SEISMO-GEODETIC CHARACTERIZATION OF THE TUZLA FAULT (IZMIR/TURKEY): ITS KINEMATICS AND EARTHQUAKE POTENTIAL

by

Bengisu Gelin

B.S., Geomatics Engineering, Yıldız Technical University, 2016

Submitted to the Institute for Graduate Studies in
Science and Engineering in partial fulfillment of
the requirements for the degree of
Master of Science

Graduate Program in Geodesy

Boğaziçi University

2020

ACKNOWLEDGEMENTS

First of all, I would like to express my deepest appreciation to my thesis advisor Assoc. Prof Fatih Bulut since he helped me always, whenever I ran into a trouble spot or had a question about my research or writing. He guided and encouraged me to be professional. I also wish to thank the members of my dissertation committee: Prof. Cenk Yaltırak and Assoc. Prof. Aslı Doğru for generously offering their time, support and guidance. In addition, I would like to thank to Assoc. Prof. Ufuk Hancılar for his significant help in terms of correcting my thesis in my final step to the graduation.

Special thanks are given to Kandilli Observatory and Earthquake Research Institute, Geodesy Department, since they give me the chance of studying here. My sincere thanks to Prof. Dr. Haluk Özener, Asst. Prof Tülay Kaya Eken, Dr. Onur Yılmaz, Dr. Aslı Sabuncu, Kaan Alper Uçan, Maryna Batur and Ahmet Ali Altın for their continuous support since the day I came to the department. Also, I am very grateful to Prof. Dr. Haluk Özener, Prof. Dr. Semih Ergintav, Assoc. Prof. Aslı Doğru, Asst. Prof Tülay Kaya Eken, Dr. Onur Yılmaz, Dr. Aslı Sabuncu and geomatics engineer Bülent Turgut for sharing their experience and knowledge.

Finally, I must express my very profound gratitude to the people who made my life meaningful and full of happiness, my parents Ayşe-Derya Gelin, my sister Bilgesu Gelin, my husband Sefa Onur Dündar for providing me continuous support and encouragement throughout my years of study and through the process of writing this thesis and to my four-legged child, Kırpık, for her limitless love. Thank you.

GPS measurements which are used in this study has been supported by The Scientific and Technological Research Council of Turkey (TUBITAK) - CAYDAG under grant no 108Y295 and Boğaziçi University Scientific Research Projects (BAP) under grant no 6359.

ABSTRACT

SEISMO-GEODETIC CHARACTERIZATION OF THE TUZLA FAULT (IZMIR/TURKEY): ITS KINEMATICS AND EARTHQUAKE POTENTIAL

İzmir, the third largest city of Turkey, located in western coast of the country is seismically super active due to Hellenic subduction zone and extensional back-arc basin under the Aegean Sea. This tectonic environment has flattened the cities in the region again and again as reported in the historical records. Hence, investigating the seismically active faults in the region is crucial to elaborate on earthquake hazard for the cities along the Western Turkey. In this context, we jointly analyzed geodetic, geological and seismological data to investigate latest failure, present day deformation, slip accumulation and fault kinematics along the Tuzla Fault. Historical and recent earthquakes were investigated to determine the latest failure of the Fault and result reveals that there is no evidence of a large earthquake failing the Fault entirely since 1688. Six epochs GPS measurements of fifteen stations were analyzed for the time period of 2009-2017 to obtain horizontal tectonic slip rates along the Tuzla Fault. As a result, overall southwest movements change between 26.67±1.03 mm/yr and 28.96±1.00 mm/yr with respect to Eurasia. Differential slip rates range between 1.00 to 2.00 mm/yr. Magnitude calculations were done for Tuzla Fault and its segments seperately. Tuzla Fault has currently a potential to generate a strong earthquake up to M6.2-M6.8. Strain analysis results show that the Çatalca Segment and northern Orhanlı Segment, accumulates high shear strain and therefore accommodate higher potential for co-seismic slip. According to fault plane solutions and maximum shear strain values and planes, Cumalı Segment has dextral characteristic, however, maximum shear strain planes indicates sinistral structure in Çatalca Segment.

ÖZET

TUZLA FAYI'NIN (İZMİR/TÜRKİYE) SİSMO-JEODEZİK KARAKTERİZASYONU: FAY KİNEMATİĞİ VE DEPREM POTANSİYELİ

Türkiye'nin en kalabalık üçüncü kenti olan ve ülkenin Ege kıyısında yer alan İzmir, Helenik dalma batma zonunun etkisiyle sismik aktivite açısından oldukça aktiftir. Bölgenin tektonik yapısı, tarih boyunca birçok kez bölgedeki kentlerin yıkımına neden olmuştur. Bu sebeple, bölgedeki sismik olarak aktif olan fayların incelenmesi, bölgedeki şehirlerin deprem tehlikesinin ayrıntılı olarak incelenmesi açısından son derece önemlidir. Bu kapsamda, Tuzla Fayı'nın en son hangi tarihte kırıldığının, fayın güncel deformasyonunun, güncel kayma birikiminin ve fay kinematiğinin belirlenebilmesi için jeodezik, jeolojik ve sismolojik veriler analiz edilmiştir. Tarihsel ve aletsel dönem depremleri, fayın son kırıldığı tarihi belirlemek için araştırılmış ve fayın 1688 yılından beri kırıldığına dair bir kanıt olmadığını görülmüştür. Tektonik kayma miktarını belirlemek amacıyla 2009-2017 yılları arasında altı epok olarak yapılan ölçmeler analiz edilmiştir. Sonuçlar, istasyonların kayma hızlarının Avrasya plakasına göre güneybatı yönünde 26.67±1.03 mm/yr and 28.96±1.00 mm/yr arasında olduğunu, diferansiyel kayma miktarının ise 1.00-2.00 mm/yr arasında değiştiğini göstermiştir. Sonuç olarak, Tuzla Fayı ve her segmentin ayrı ayrı üretecekleri büyüklüklerin hesaplamaları yapılmış ve Tuzla Fayı üzerindeki olası bir depremin 6.2 ile 6.8 büyüklükleri arasında bir deprem üretme potansiyeli olduğu saptanmıştır. Gerinim analizi sonuçları, Çatalca Segmenti ve Orhanlı Segmentinin kuzeyinin yüksek gerinim değerine sahip olduğunu göstermiştir. Odak mekanizması analizlerine ve maksimum gerinim değerlerine göre, Cumalı Segmenti sağ yanal karaktere sahip olmasına rağmen, Çatalca segmentinin maksimum gerinim değerleri sol yanal yapıya işaret etmektedir.

TABLE OF CONTENTS

LIST OF FIGURES

LIST OF TABLES

LIST OF SYMBOLS

A	Area
a_0	Clock bias
a_1	Clock drift
a_2	Frequency drift
c	Speed of light
f	Frequency
ΔL_{ij}	Single differences
$\Delta\nabla L$	Double differences
$\Delta\nabla\Delta L$	Triple differences
M_0	Seismic moment
M	Moment magnitude
N	Ambiguity
P	Force
R_r^s	Observed pseudorange between receiver and satellite
r	Slope
s	Slip
t	Time
V	Velocity
x_i, y_i, z_i	Coordinates of the given object/station
ε	Strain
ε_x	Error
ε_{xx}, ε_{xy}, ε_{yx}, ε_{yy}	Components of deformation tensor
λ	Wavelength
λ_D	Dilatation
λ_1,λ_2	Principal components
μ	Shear modulus
ρ_r^s	Distance between receiver and satellite

τ	Stress
Φ_r^s	Observed carrier phase between receiver and satellite

LIST OF ACRONYMS/ABBREVIATIONS

2D	Two Dimensional
3D	Three Dimensional
AFAD	Afet ve Acil Durum Yönetimi Başkanlığı / Ministry of Interior Disaster and Emergency Management Presidency
BDS	BeiDou Navigation Satellite System
DOP	Dilution of Precision
EAF	East Anatolian Fault
ECEF	Earth Centered Earth Fixed
ECI	Earth Centered Inertial
EU	European Union
GAMIT	GNSS at MIT
GEO	Geostationary Orbit
GDOP	Geometrical Dilution of Precision
GLONASS	Globalnaya Navigatsionnaya Sputnikovaya Sistema
GLOBK	Global Kalman Filter
GNSS	Global Navigation Satellite System
GPS	Global Positioning System
IAG	International Association of Geodesy
IGS	International GNSS Service
IGSO	Inclined orbit
ISC	International Seismological Center
ITRF	International Terrestrial Reference Frame
KOERI	Kandilli Observatory and Earthquake Research Institute
KOERI-RETMC	Kandilli Observatory and Earthquake Research Institute-Regional Earthquake and Tsunami Monitoring Center
MEO	Medium Earth Orbit
MTA	Maden Tetkik ve Arama Genel Müdürlüğü / General Directorate of Mineral Research and Exploration
NAF	North Anatolian Fault

NASA-JPL	National Aeronautics and Space Administration-Jet Propulsion Laboratory
PDOP	Positional Dilution of Precision
TDOP	Time Dilution of Precision
USA	United States of America
USGS	United States Geological Survey
UTC	Coordinated Universal Time

1. INTRODUCTION

As we are living in the tectonically active planet, earthquakes are part of our lives. Turkey, due to the geological structure of the Anatolian Plate, is one of the most affected countries from earthquakes in the Earth. Table 1.1 indicates how often earthquakes occur in Turkey and in the Earth. As can be easily seen in this comparison, every fourth day a strong earthquake occurs in the Earth. This period is 1.5 years in Turkey to have a strong earthquake. Figure 1.1 illustrates all major earthquakes since 1900 [3]. It shows that researches about examining the globe in the scope of crustal movements and eventually, earthquakes, are essential field to understand the Earth better and to avoid its natural disasters. Since earthquakes are one of the most dangerous disasters, especially with the increasing rate of urbanization, investigating seismically active faults is becoming more crucial in order to assess hazard and risk of strong or larger earthquakes.

Table 1.1. Statistics of Earthquakes occurrence frequency in the world and Turkey (KOERI, USGS, AFAD).

Magnitude	**Classification**	**Turkey**	**Earth**
8+	Great	-	Every 15 months
7<M<8	Major	Every 6-7 years	every month
6<M<7	Strong	Every 1.5 years	Every 4 days
5<M<6	Moderate	Every 1.6 months	Twice in a day

Turkey has always been in the focus of the earthquake research community since it hosts two major active faults, namely the North Anatolian Fault (NAF) and the East Anatolian Fault (EAF), and various number of other active faults which can generate catastrophic results. Although there are many investigations that have been already done on the NAF and the EAF, the faults located in the Western Turkey have been investigated only by limited number of studies. Therefore, we focused Tuzla Fault located in Izmir, third largest city of Turkey accommodating currently 4.3 million inhabitants. Figure 1.2 indicates the population density of both Turkey and Izmir.

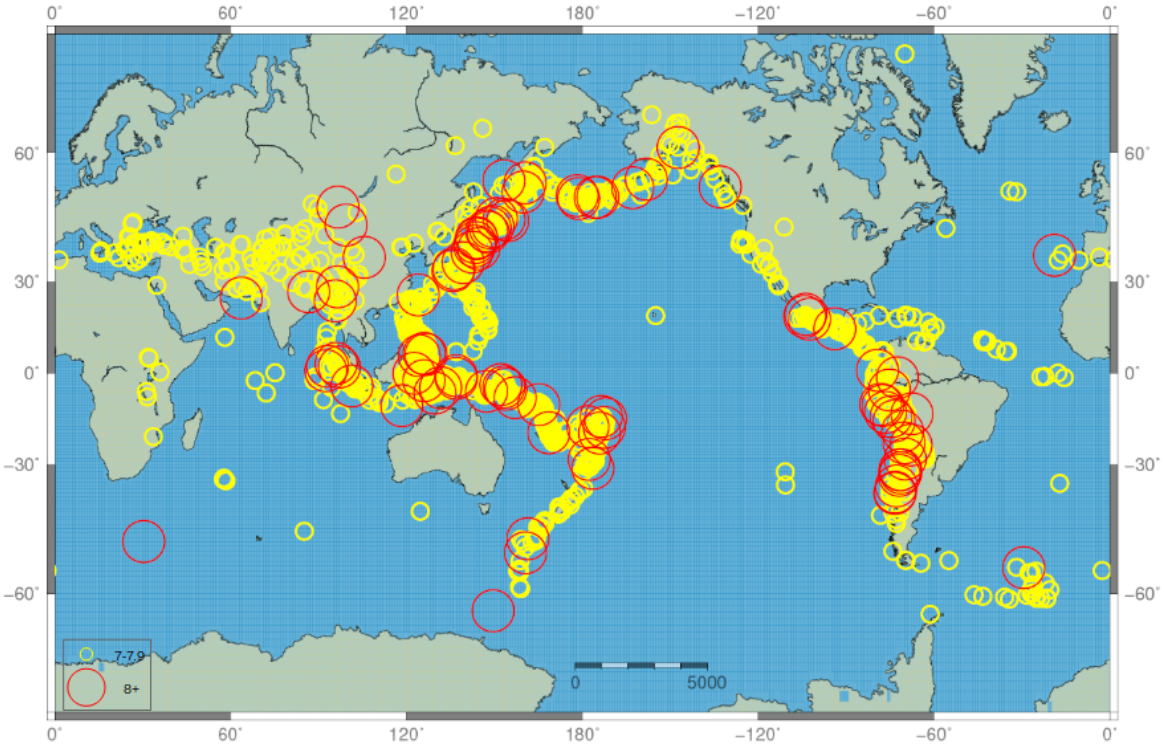

Figure 1.1. Earthquakes occured between 1900-2020 (M>7) in the World. Data were taken from USGS .

Tuzla Fault extends for 50 km [4] in the south of Izmir near the city center, its largest water reservoir [5] and its main airport (Izmir Adnan Menderes Airport). Therefore, it is essential to investigate present day earthquake potential of the Tuzla Fault.

In this frame, we combined all available geodetic, geological and seismological data to better understand the kinematics and the deformation of the Tuzla Fault. Historical earthquakes were examined to determine the latest failure and earthquake cycle of the Fault [4, 6, 7]. Furthermore, instrumental earthquakes were relocated to verify whether the fault was partly failed during the last century [8]. In a second step, we used six-years of campaign based GPS data for fifteen sites between the years of 2009 and 2017, deployed by Kandilli Observatory and Earthquake Research Institute, Geodesy Department. Those data were processed using GAMIT/GLOBK software [9] and we obtained precise coordinates and velocities of fifteen sites in the area. GPS-derived velocity field was analyzed to identify strain field along the Tuzla Fault in

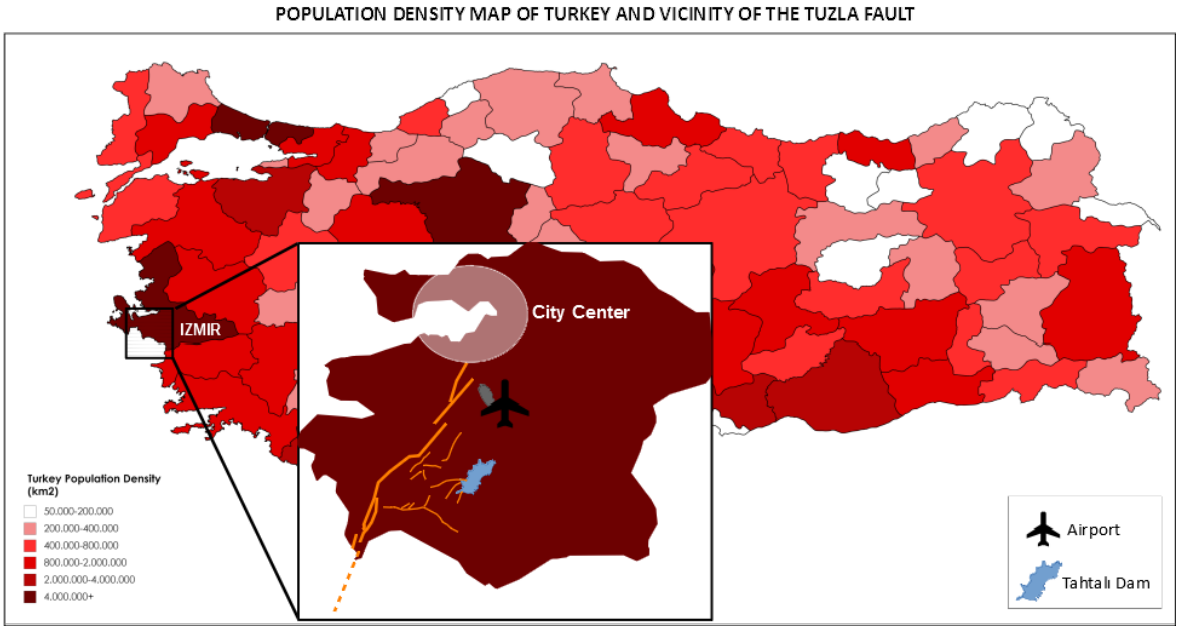

Figure 1.2. Population Intensity Map of Turkey and vicinity of the Tuzla Fault. Inset figure reveals both Adnan Menderes Airport and Tahtalı Dam that can also be affected in case of a strong earthquake on the Tuzla Fault due to their close proximities to the Tuzla Fault. Population density data were taken from Izmir Governorship.

order to characterize its kinematics. Additionally, FOCMEC software [10] were used to investigate the focal mechanism of the earthquakes occurred on or near the Tuzla Fault to verify its fault kinematics, which is still in-debate. Finally, we calculated present day slip accumulation and we include main characteristics of the Tuzla Fault to determine the possible magnitude of the Tuzla Fault can generate.

2. SEGMENTATION AND LONG TERM SEISMICITY OF THE TUZLA FAULT

2.1. Segmentation of the Tuzla Fault

Tuzla Fault have been characterized by NE-SW extension [4] and researchers mentioned the Fault with several different names such as Orhanlı Fault [11], Cumalı Thrust Fault [12], Cumaovası Linearity [13] and finally Tuzla Fault [14]. While its length has been determined approximately 42 km [15–17] on land, it reaches 50 km with its offshore part [18, 19] The fault covers three major segments namely Çatalca, Orhanlı and Cumalı segments from North to South, respectively [11] (Figure 2.2). Length of the Çatalca Segment reaches 15 km and differentiates from Orhanlı segment which has approximately 16 km [4]. Although Cumalı segment has 15 km length in land, when the offshore part of the segment were taken into account as 10 km [18] it reaches 25 km as a whole. Beside joint decisions made for the fault such as it covers three different segments, different aspects are arising when it comes to the fault geometry of the fault. Figure 2.1 indicates the Tuzla Fault and surrounding region determined by (Emre et al., 2011a-b) [20,21], by (Genç et al., 2001) [11], and (Göktaş, 2019) [22], respectively. Although (Genç et al., 2001) mentioned another fault which is named "Yeniköy Fault Zone" parallel to the Tuzla Fault (Figure 2.1), this fault is not specified in active fault map series of Turkey, Izmir quadrangle. Furthermore, Göktaş, 2019 mentioned that there can be another possible fault which has a normal characteristic in eastern side of the Tuzla Fault. In this research, while we used and plotted Tuzla Fault based on (Emre et. al, 2011); we took the small faults near the fault from (Genç et. al., 2001).

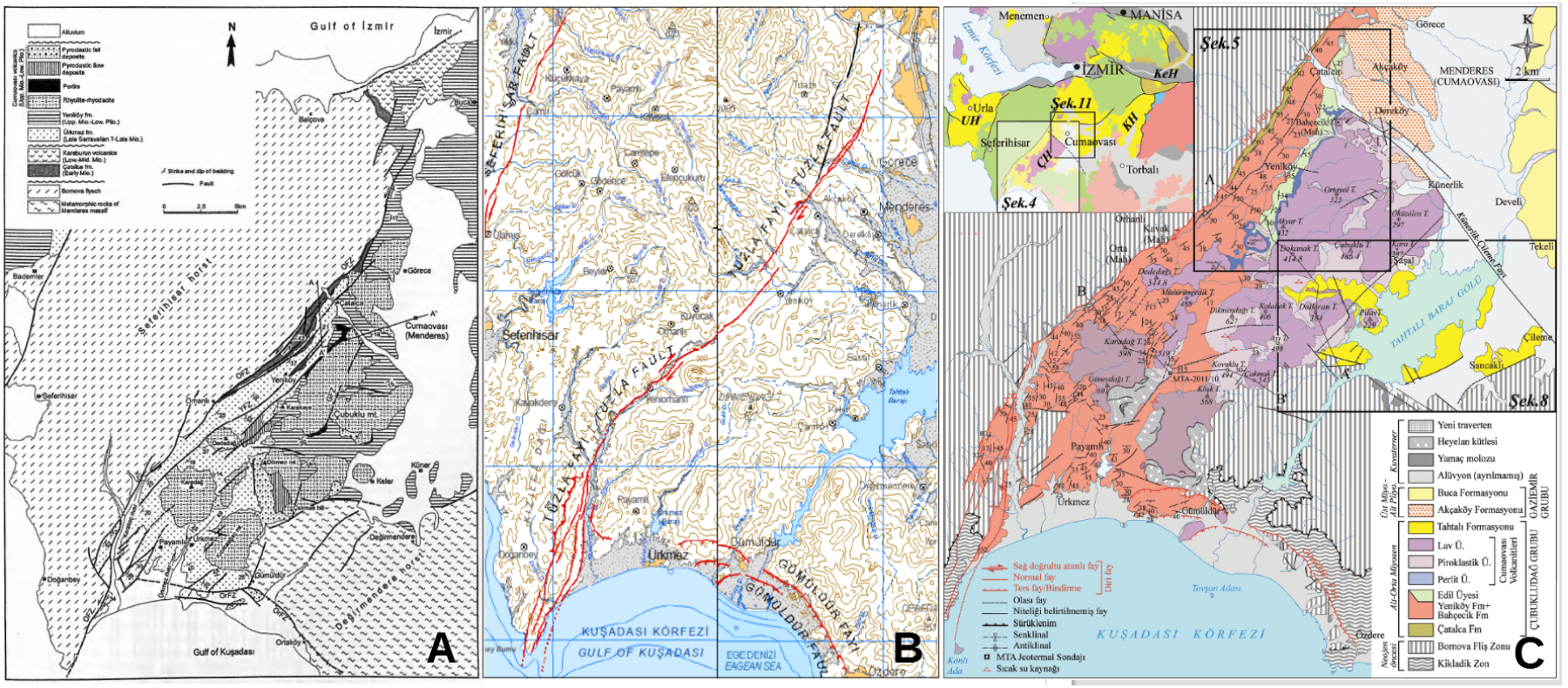

Figure 2.1. (A) Geology of Tuzla Fault (Genç et al., 2001), Abbreviations, GFZ, OFZ, OrFZ and YFZ stands for Göllükaya Fault Zone, Orhanlı Fault Zone, Ortaköy Fault Zone and Yeniköy Fault Zone, respectively. (B) Fault Geometry according to (Emre et. al., 2011) , (C) Fault Geometry and geology, (Göktaş, 2019).

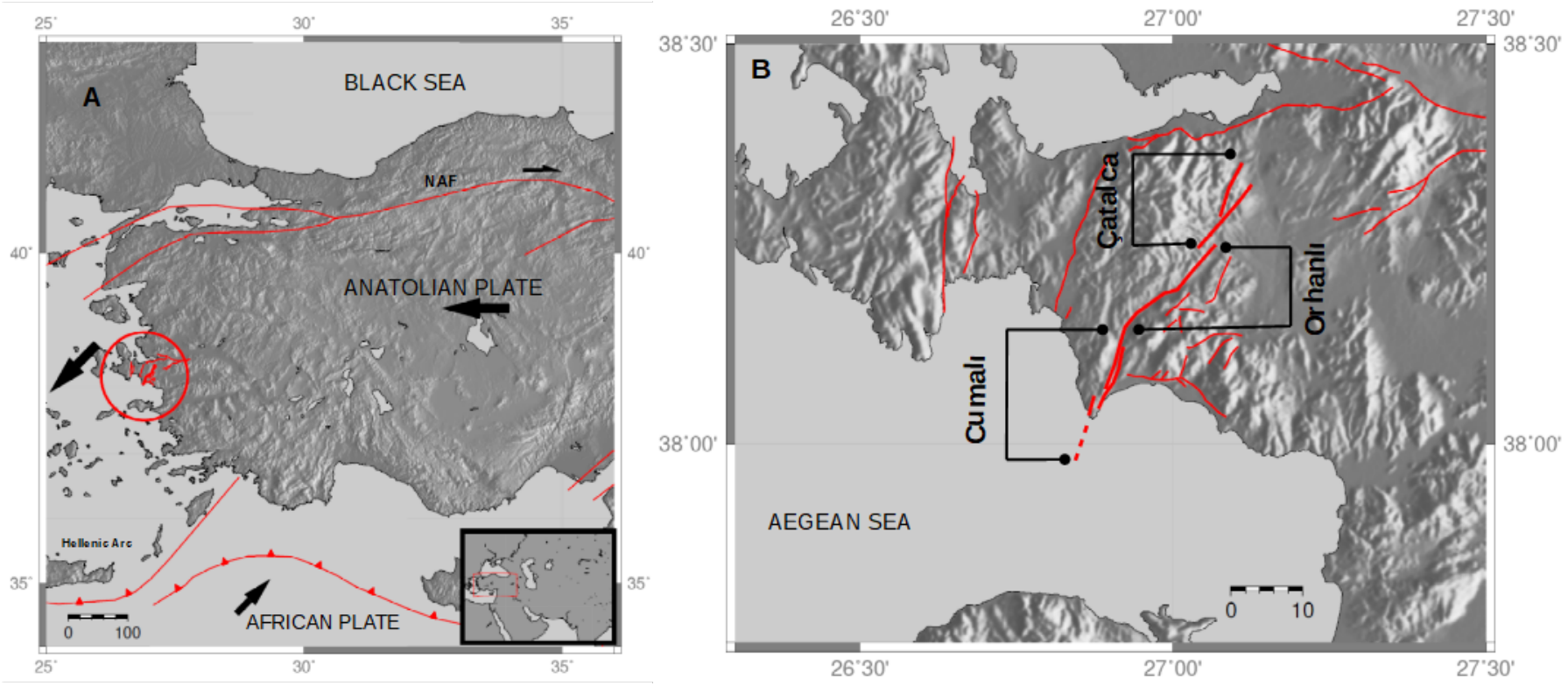

Figure 2.2. A indicates representation of research area and main faults of Western Turkey and vicinity. B shows segments of the Tuzla Fault. Faults located in Turkey and Mediterranean Sea in Figure A and B were taken from (Emre et al., 2011), (Emre et al., 2013) [1], (Genç et al., 2001) and (Barka, 1992) [2].

2.2. Historical and Recent Earthquakes

We investigated significant earthquakes occurred in the target area during historical and instrumental periods, between 47 CE and 2019 CE to elaborate on the time when the Tuzla Fault has been partly/completely failed. This will allow us to identify initiation time of the slip storage that will define the present day earthquake potential of the Tuzla Fault.

2.2.1. Historical Earthquakes

Historical earthquakes occurred in the vicinity of the Tuzla Fault (50 km) obtained combining the earthquake catalogues by (Grünthal, G., Wahlström, R., 2012), (Tan et al., 2008), (Emre et al., 2005). Restricting historical earthquake catalog to the distance range of 50 km, we found ten destructive earthquakes near Tuzla Fault. (Table 2.1) (Figure 2.3). Only two of these earthquakes, which have occurred in 178 (M 6.5) and 1688 (M 6.8), were able to generate the latest complete failure of the Tuzla Fault.

Table 2.1. Combined catalogue of historical earthquakes in the vicinity of the Tuzla Fault. (*) indicates events that have a potential to generate the last failure of the Tuzla Fault. 1, 2 and 3 in the eighth column indicate the references taken from (Emre et al., 2005), (Grünthal and Wahlström, 2012), (Tan et al., 2008), respectively.

Date			**Lat (°)**	**Long (°)**	**Intensity**	**Magnitude**	**References**
Y	**M**	**D**					
47			38.45	27.18	-	6.3	2,3
178			38.30	27.10	VIII	6.5	1
688			38.41	27.20	IX	6.5	1
1039			38.40	27.30	VIII	6.8	1,2
1664	**6**	**2**	38.41	27.20	VII	5.8	1
1668			38.41	27.20	IX		1,3
1680	**2**	**14**	38.40	27.20	VII	6.2	1,2
1688*	**7**	**10**	38.38	27.17	X	6.8	2
1723			38.40	27.00	VIII	6.4	1,2
1883	**10**	**15**	38.30	26.60	IX	6.8	2

2.2.2. Instrumental Period Earthquakes

We used seismic data from International Seismological Center (ISC) [23] [24] and Boğaziçi University Kandilli Observatory and Earthquake Research Institute (KOERI) [25] to refine hypocenter locations of the earthquakes occurred in instrumental period (Figure 2.3). We used "Hypocenter" [8] computer program to invert travel time data for the absolute earthquake locations. Hypocentral depths are further optimized with a grid search over the range of all potential depths between 0 - 20 km. Totally 38 earthquakes have been analyzed near the Tuzla Fault for the time period of 1928-2019 CE. Tables from 2.2 to 2.4 indicate total 38 earthquakes larger than magnitude 3.5 and Figure 2.3 shows refined catalogue for the earthquakes larger than Mw5.0. In our catalogue, hypocentral locations are mostly resolved better than 3 km in horizontal axes. However, due to the lack of accurate and sufficient seismic data, same accuracy is not maintained for some of those which occurred in instrumental period.

Location of the November 1992 earthquake is refined precisely using the seismic data of ISC (2.2 km in latitude and 1.7 km in longitude). Relocation of the earthquake clarified that the earthquake was occurred approximately 10 km northeastern side of the result of USGS. Furthermore, since there are three different realizations of the Tuzla Fault and vicinity (Figure 2.1), we performed with three different scenarios whether there is a fault named Yeniköy Fault or not. For all, 1992 earthquake may not have broken the Tuzla Fault since its epicenter more likely occurred on the one of the eastern faults. Only the August 8, 2019 Mw 5.0 earthquake occurred on the Cumalı Segment of Tuzla Fault. However, this Mw 5.0 earthquake cannot rupture more than a few kilometers of fault patch. Investigation of past earthquakes both in historical and instrumental periods indicates that the Tuzla Fault did not completely fail since the 1688 (M 6.8) earthquake. In other words, forthcoming large earthquake rupturing the Tuzla Fault will release the slip that has been accumulated since 1688.

Table 2.2. Revised catalogue of instrumental period earthquakes from KOERI in the vicinity of the Tuzla Fault.

Date			**Hour**	**Lat (°)**	**err(km)**	**Lon (°)**	**err(km)**	**Depth**	**err(km)**	**Magnitude**
Y	**M**	**D**								
2019	8	8	08:39	38.036	1.9	26.859	2.1	14.0	1.0	5.0
2018	10	28	21:44	38.195	2.1	26.842	3.0	10	3.4	3.6
2018	10	28	08:19	38.181	1.3	26.863	1.6	7.1	2.2	3.3
2018	10	28	08:15	38.186	1.9	26.853	2.6	7.3	3.5	4.0
2018	10	28	6.18	38.202	1.3	26.841	1.8	13.3	1.7	3.8
2018	10	28	05:40	38.177	2.2	26.860	3.0	5.8	4.1	3.5
2016	10	17	01:30	37.918	1.2	26.885	2.3	17.2	3.1	4.7
2016	9	27	04:34	38.171	1.8	27.014	2.7	10	2.1	3.6
2016	9	23	05:06	38.179	1.8	27.015	3.0	11.3	2.2	3.9
2015	1	10	04:32	38.198	1.8	27.051	4.4	13.1	3.3	4.3
2014	11	22	08:57	38.074	2.5	27.018	4.5	8.9	4.9	3.7
2014	10	21	03:03	38.182	2.1	27.096	4.0	10.7	3.5	4.1
2014	5	2	00:02	37.993	1.9	27.011	3.1	15.5	3.0	3.7
2013	5	26	05:37	38.289	1.9	27.164	1.7	12.5	2.9	3.5
2013	5	26	02:39	38.306	2.3	27.174	17	10.2	3.3	3.6
2012	2	4	20:10	38.072	2.1	26.843	3.5	15.2	2.1	3.8

Table 2.3. Revised catalogue of instrumental period earthquakes from KOERI in the vicinity of the Tuzla Fault.

Date			**Hour**	**Lat (°)**	**err(km)**	**Lon (°)**	**err(km)**	**Depth**	**err(km)**	**Magnitude**
Y	**M**	**D**								
2010	11	11	20:08	37.864	0.6	27.348	0.6	11.7	0.8	4.7
2006	11	21	12:14	38.011	2.4	26.748	3.0	18.0	4.8	3.5
2006	3	9	03:18	37.856	1.2	26.761	1.3	9.2	2.8	4.3
2005	10	31	05:26	38.147	0.9	26.653	1.2	11.0	1.7	4.8
2005	10	20	21:40	38.162	1.0	26.700	1.0	5.0	2.0	5.9
2005	10	17	09:55	38.154	0.9	26.627	1.3	15.0	1.5	5.3
2005	10	17	09:46	38.180	1.0	26.661	1.2	10.0	1.0	5.8
2005	10	17	05:45	38.133	0.9	26.613	1.0	9.5	1.0	5.7
2005	3	17	05:03	37.771	1.5	26.887	2.5	6.9	3.3	4.3
2003	4	10	00:40	38.258	1.4	26.891	1.4	12.0	2.0	5.8
1998	7	9	17:36	37.919	1.2	26.748	1.5	12.0	1.0	5.3
1996	4	2	07:59	37.931	1.4	26.986	1.6	11.0	1.0	4.9
1992	11	6	20:05	38.081	2.4	27.021	1.8	10	2.3	4.7
1992	11	6	19:08	38.214	2.2	27.080	1.7	12.0	3.0	6.0
1984	4	23	10:31	37.949	1.8	27.007	1.6	10.6	3.6	4.6
1977	12	16	07:37	38.358	1.0	27.243	1.2	5.0	1.5	5.3

Table 2.4. Revised catalogue of instrumental period earthquakes from KOERI in the vicinity of the Tuzla Fault.

Date			**Hour**	**Lat (°)**	**err(km)**	**Lon (°)**	**err(km)**	**Depth**	**err(km)**	**Magnitude**
Y	**M**	**D**								
1974	2	1	00:01	38.656	2.6	27.359	2.7	18	2.5	5.3
1954	5	1	20:53	37.796	1.4	26.871	2.3	10.0	2.0	5.4
1954	5	1	15:24	37.705	4.3	27.327	4.7	5.9	3.2	5.3
1953	5	2	18:37	38.318	2.2	26.464	2.9	16	4.1	5.1
1953	5	1	20:06	38.288	2.5	26.486	3.6	13	4.2	4.9
1928	3	31	00:29	38.123	4.8	27.572	6.3	6.0	4.0	6.2

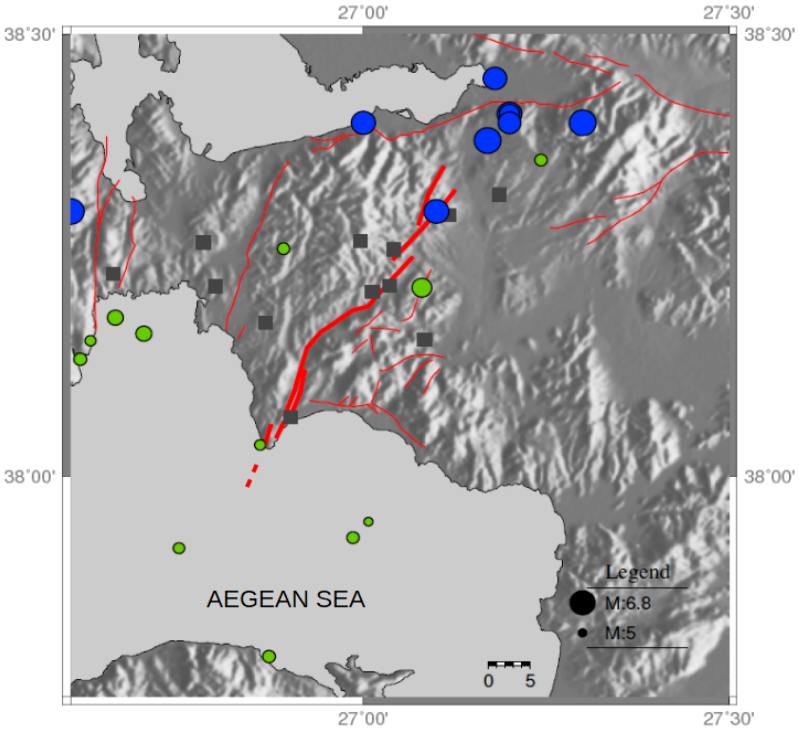

Figure 2.3. Green and blue circles show instrumental and historical earthquakes M>5, respectively. Circle sizes represent magnitudes of the earthquakes. Gray squares represent campaign-based GPS stations. Fault plotted thick red line indicates Tuzla Fault. Thin red faults are other faults located in the area.

3. GPS DATA PROCESSING

We analyzed six epochs of GPS measurements from the fifteen-station campaign-based network (Table 3.2) using GAMIT/GLOBK software [9], which covers wide variety of programs calculating residual observations and partial derivatives, finding outliers and performing a least squares analysis. The network has been deployed by KOERI Geodesy Department [15]. We additionally included thirteen IGS stations (Table 3.1) for double-differencing and to fix the absolute positions. IGS stations were chosen according to their data quality in the days of our campaign-based GPS measurements. As a reference frame, ITRF08 [26] were used for all processes. Zenith delay unknowns were calculated through the SAAS model described by Saastamoinen,1972 [27]. BERNE model [28] were used for direct solar radiation accelerations. Time series are optimized to estimate velocities of stations using GLOBK, which includes Kalman filtering techniques (Table 3.3) (Figure 3.1).

First order results indicate that two stations, namely URKM and KPLC, have errors above 1.0 mm/yr. Hence, they have not been included for the final process and the interpretation. GPS-derived velocities range between 26-28 mm/yr. The uncertainties remain below 1.0 mm to the Southwest with respect to the stable Eurasian Plate (Table 3.3). Slip deficit which Tuzla Fault stored annually varies from 1.00 to 2.00 mm. Time series indicated that cumulative displacements range from 21.33 to 23.17 cm with respect to stable Eurasia for the time period of 2009-2017 (Figure 3.1).

Table 3.1. IGS Stations used in GPS process.

Name	**Country**	**Latitude**	**Longitude**	**Satellite System**
AJAC	France	41.9274	8.7626	GPS+GLO+GAL+BDS+SBAS
BUCU	Romania	44.4639	26.1257	GPS+GLO
GLSV	Ukraine	50.3642	30.4967	GPS+GLO+GAL+BDS+QZSS+SBAS
GRAZ	Austria	47.0671	15.4935	GPS+GLO+GAL+BDS
NICO	Cyprus	35.1409	33.3964	GPS+GLO+GAL+BDS+SBAS
NOT1	Italy	36.8761	14.9898	GPS+GLO+GAL+BDS+SBAS
ONSA	Sweden	57.3952	11.9255	GPS+GLO+GAL+BDS+SBAS
POTS	Germany	52.3792	13.0660	GPS+GLO+GAL+BDS+QZSS+IRNSS+SBAS
SVTL	Russia	60.5328	29.7808	GPS+GLO
VILL	Spain	40.4436	-3.9520	GPS+GLO+GAL+BDS+SBAS
YEBE	Spain	40.5249	-3.0886	GPS+GLO
ZECK	Russia	43.7883	41.5650	GPS+GLO
ZWE2	Russia	55.7000	36.7600	GPS

3.1. GPS Campaigns in the Area

First research to install the fifteen-station network were done by KOERI, Geodesy department in 2006 [15,29]. The construction of fifteen stations were made on bedrock to prevent creep or other surface movements in order to observe pure crustal movement [15, 30]. KOERI Geodesy Department has deployed a fifteen-station campaign based GPS network to monitor geodetic deformation along the Tuzla Fault. We analyze six epochs (2009, 2010, 2011, 2012(1),2012(2) 2017) of GPS measurements from this network that are currently available for the time period of 2009-2017. Local stations namely ASKE, CTAL, ESEN, GEMR, GORC, HZUR, KOKR, PTKV, SFRH, TRAZ, TURG, YACI and YKOY were processed using GAMIT/GLOBK software with combining thirteen IGS (YEBE, AJAC, BUCU, NICO, SVTL, ZECK, GLSV, NOTL, ONSA, POTS, VILL, ZWE2). While KPLC and URKM were used in initial process, because of their high uncertainties, data of these two stations were extracted from final process.

Table 3.2. GPS campaign dates of the stations. KPLC and URKM stations extracted from the process.

Stations	2009		2010		2011		2012				2017	
	229	230	152	153	145	146	38	39	157	158	87	88
ASKE		x		x		x		x		x	x	
CTAL	x		x		x		x		x			x
ESEN	x		x	x	x	x		x	x	x	x	
GEMR	x		x		x		x		x		x	
GORC	x		x		x		x		x		x	
HZUR		x	x		x	x	x		x	x	x	
KOKR	x		x		x		x		x		x	
PTKV		x		x		x		x		x		x
SFRH		x		x		x		x		x		x
TRAZ		x		x		x		x		x		x
TURG	x		x		x	x		x		x		x
YACI	x		x		x		x		x		x	
YKOY	x		x		x		x		x			x
KPLC		x		x		x	x		x			
URKM		x		x		x		x		x		
Observation duration	10h	10h	10h	10h	10h	10h	10h	10h	10h	10h	10h	10h
Elevation Mask	10	10	10	10	10	10	10	10	10	10	10	10

Table 3.3. Latitude and Longitude of campaign-based stations, their annual displacements in East and North with their uncertainties with respect to the Eurasia.

Station	**Lat (°)**	**Long (°)**	N_{vel}**(mm/yr)**	N_{sig}**(mm/yr)**	E_{vel}**(mm/yr)**	E_{sig} **(mm/yr)**
ASKE	38.174	26.867	-19.7	0.61	-20.79	0.6
CTAL	38.257	27.041	-18.61	0.9	-21.81	0.84
ESEN	38.156	27.084	-17.62	0.66	-20.59	0.67
GEMR	38.319	27.186	-15.9	0.83	-22.01	0.77
GORC	38.296	27.117	-18.11	0.65	-21.00	0.66
HZUR	38.068	26.900	-21.62	0.71	-19.22	0.69
KOKR	38.183	26.599	-21.55	0.71	-19.35	0.71
PTKV	38.209	27.012	-18.5	0.76	-20.24	0.73
SFRH	38.215	26.797	-19.31	0.63	-19.52	0.64
TRAZ	38.267	26.996	-18.28	0.67	-21.05	0.65
TURG	38.265	26.781	-21.03	0.72	-19.69	0.69
YACI	38.229	26.658	-19.85	0.67	-20.52	0.66
YKOY	38.216	27.036	-17.56	0.73	-20.07	0.74

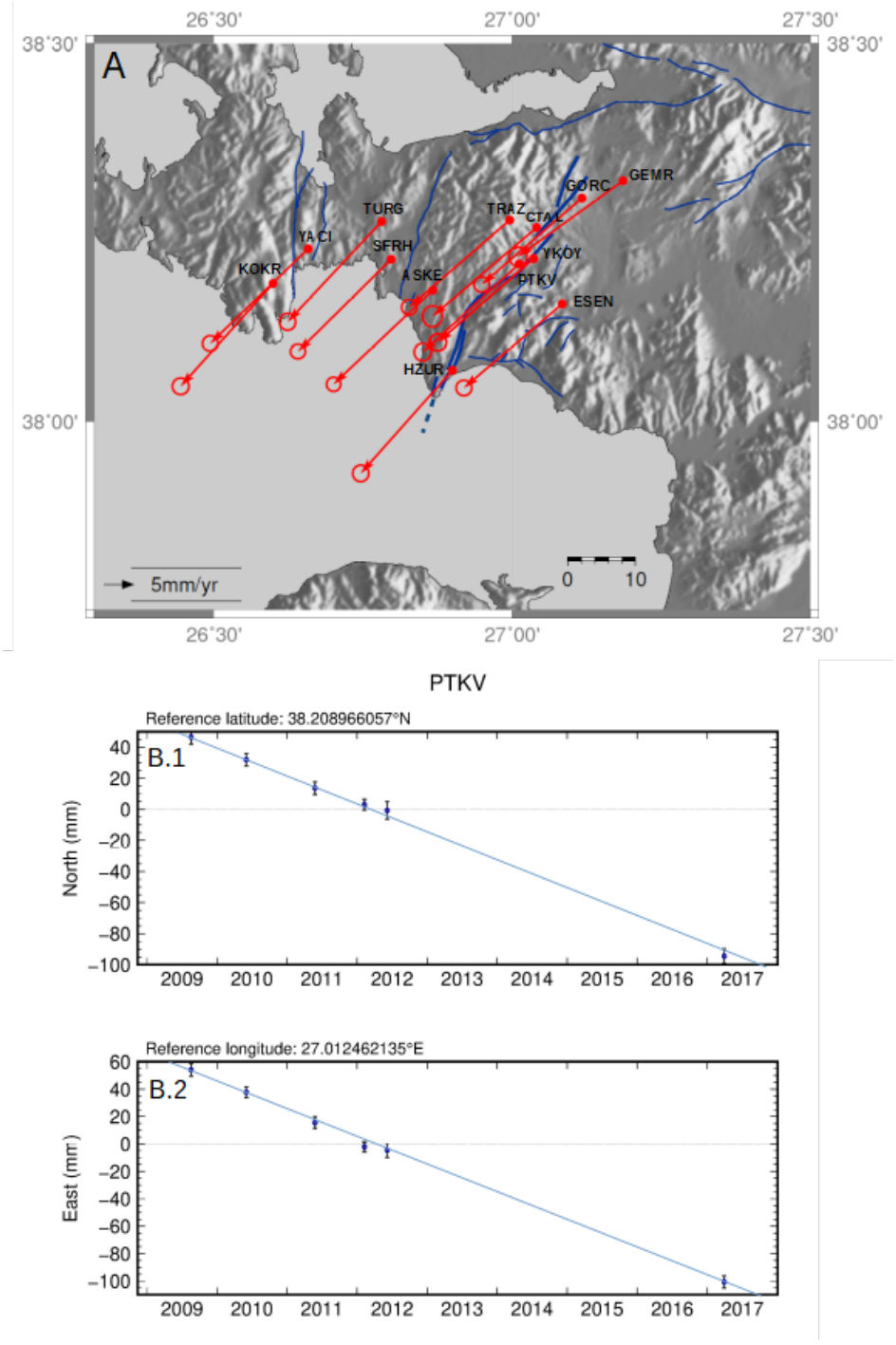

Figure 3.1. A indicates campaign based stations and their velocities (mm/yr) with respect to the fixed Eurasian Plate. The annual velocities of the stations are at 95% confidence level. B.1 and B.2 indicate time series of PTKV in North and East from 2009 to 2017, respectively. For the eight years of period, total displacements of both components are ∼148 mm and ∼160 mm. Time series of all stations are provided in the appendix C

4. STRAIN RATE

We performed strain calculations [31] in order to investigate lateral variation of elastic deformations along the Tuzla Fault and its surroundings. GAMIT/GLOBK derived horizontal coordinates (N, E) as well as their slip rates were used for Delaunay triangulation and calculating strain tensors. The functions of the deformations were represented as first-degree polynomial equations. Partial derivatives of coordinates in the equation, namely the components of the deformation tensors were adjusted by the least squares method. Using those elements, we obtain dilatation, maximum and minimum shear and rotation. Alternatively, we used SSPX [32] to calculate strain rate from velocity data of thirteen stations. Delaunay triangulation mode was preferred for strain rate calculations. Strain values of sixteen triangles were indicated in Table 4.1.

Figure 4.1 compares results from these two alternative calculations. Although there are some slight discrepancies between strain results due to the different calculation methods, overall strain tensors indicate that there are strain accumulations located on or near the Tuzla Fault (Figure 4.2). We found that four triangles, which are located in the northern section of the fault, namely 6, 8, 9 and 12 have larger strain tensors among others for calculation methods we used. In addition, triangle 8 corresponds to the area covering the Izmir Adnan Menderes Airport.

Due to structural complexity of the Tuzla Fault, three distinct segments of the fault operate with different kinematics from each other. Maximum shear strain planes in Figure 4.2 indicates that while southern section of the Fault (Cumalı Segment) has dextral mechanism, northern section (Çatalca Segment) has sinistral mechanism according to the relation between fault strike and corresponding planes of local shear strain.

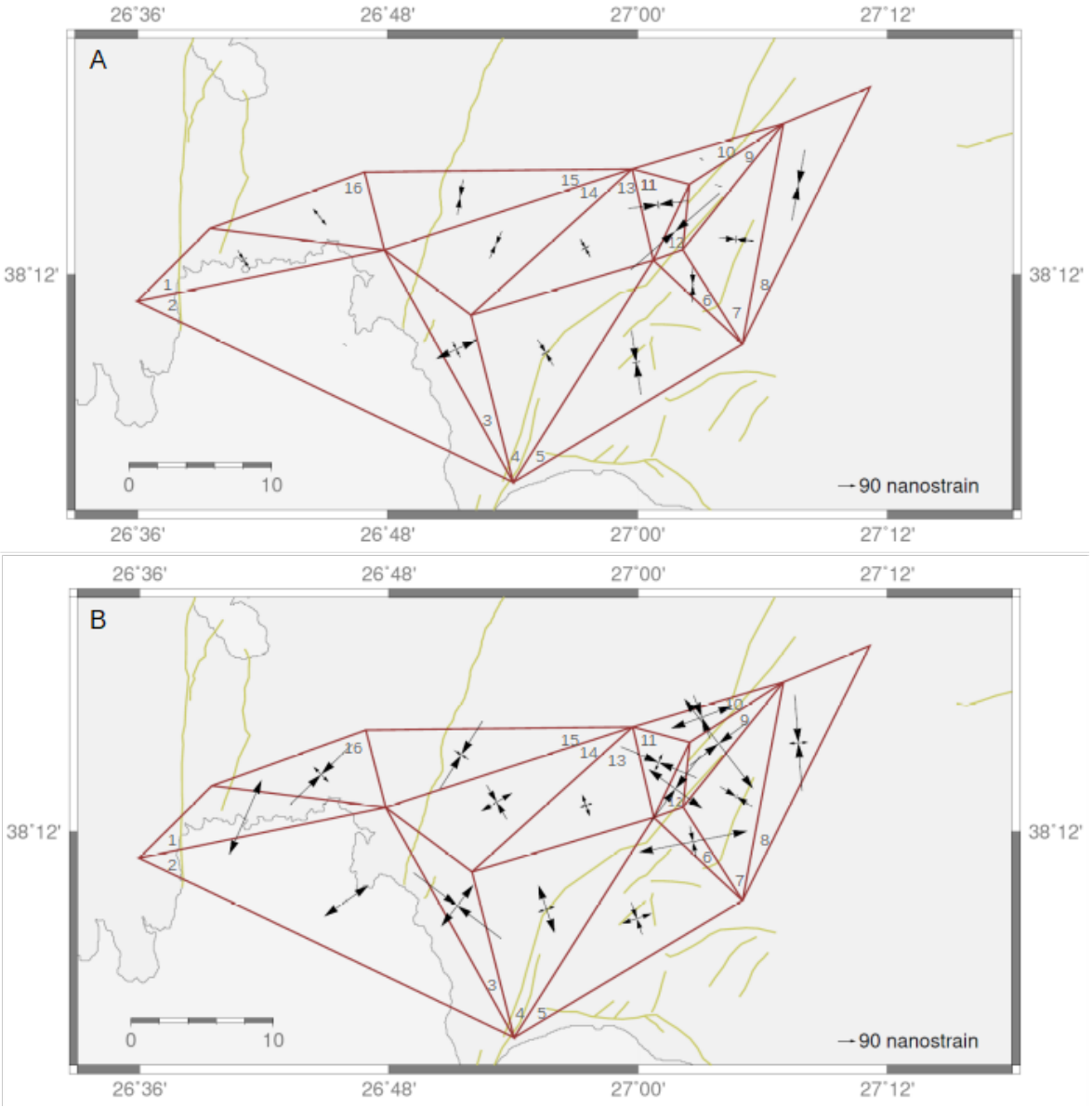

Figure 4.1. Strain rate solutions for the Tuzla Fault (A) indicates calculations according to Belhadj et. al., 2012 (B) indicates SSPX solutions. Yellow lines demonstrate the faults in the area.

Table 4.1. Strain values of sixteen Delaunay triangles in the study area.

Triangle	**No**	**Latitude**	**Longitude**	**Emax**	**Emin**
KOKR-YACI-SFRH	1	38.2092	26.6848	2.9456E-07	6.8768E-09
KOKR-SFRH-HZUR	2	38.1554	26.7657	1.9619E-07	-1.1345E-08
SFRH-ASKE-HZUR	3	38.1524	26.8548	1.9105E-07	-3.9248E-07
ASKE-HZUR-PTKV	4	38.1502	26.9264	1.8482E-07	6.5363E-08
HZUR-PTKV-ESEN	5	38.1441	26.9988	1.1601E-07	-1.2045E-07
PTKV-ESEN-YKOY	6	38.1934	27.0440	3.9735E-07	-1.1444E-07
ESEN-YKOY-GORC	7	38.2223	27.0787	-1.6155E-08	-1.3499E-07
GORC-ESEN-GEMR	8	38.2567	27.1286	7.2018E-08	-3.4799E-07
YKOY-GORC-CTAL	9	38.2562	27.0646	4.0871E-07	-2.6271E-07
GORC-CTAL-TRAZ	10	38.2732	27.0511	2.3643E-07	-1.6705E-07
TRAZ-CTAL-PTKV	11	38.2443	27.0164	6.9969E-08	-2.9177E-07
PTKV-CTAL-YKOY	12	38.2272	27.0299	2.4085E-07	-2.9422E-07
TRAZ-PTKV-ASKE	13	38.2167	26.9581	8.3155E-08	4.4802E-08
ASKE-TRAZ-SFRH	14	38.2188	26.8864	1.3134E-07	-1.4219E-07
SFRH-TRAZ-TURG	15	38.2491	26.8580	-6.0266E-08	-2.8795E-07
TURG-SFRH-YACI	16	38.2365	26.7455	8.0618E-08	-3.1262E-07

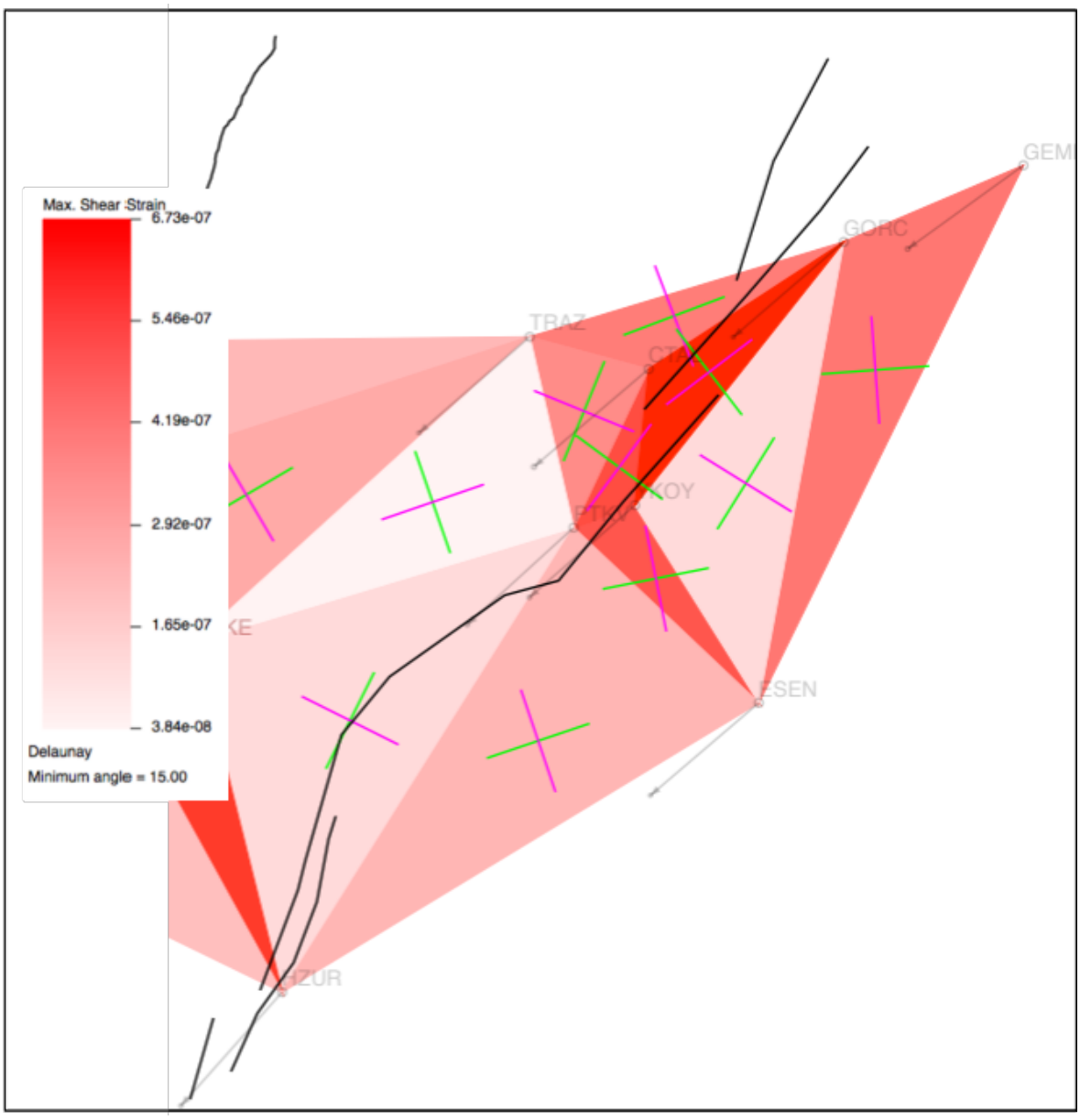

Figure 4.2. Maximum shear strain values and planes. Green and pink planes correspond dextral and sinistral mechanism which the fault may have according to SSPX strain results, respectively.

5. FOCAL MECHANISMS

We analyzed the seismic data to refine their locations and to investigate their focal mechanisms. We used HYPOCENTER to refine earthquake locations using P- and S-wave arrivals [8]. We used FOCMEC program to search for best-fitting strikes, dips and rakes with P-wave first motion data [10]. Fault plane solutions of all earthquakes larger than Mw 3.5 were obtained in the study area. However, three earthquakes occurred in 2003 and 1992 (Table 5.1) were taken from USGS as the seismic data are available only after 2003. Our refined hypocenter locations and fault plane solutions are listed in Table 5.1 and Table 5.2.

There was only one earthquake M≥5.0 along the Tuzla fault during the instrumental period (>1900). This Mw 5.0 earthquake occurred recently along the southern-most section of the fault in August 2019 (KOERI). Our results show that it has a dextral fault plane mechanism (Figure 5.1). Right lateral mechanism of the earthquake is well correlated with overall results from our strain calculations and fault plane solutions along the southern section of the Tuzla Fault. However, there is not any M≥5.0 earthquake occurred along the northern section of the Tuzla Fault in the last century. Fault mechanism solutions mainly indicate strike-slip, sometimes with a gentle reverse component. There are also pure reverse fault mechanisms, e.g. in Gaziemir region, where the airport settled, two reverse-type earthquakes occurred in 2013 with magnitudes 3.5 and 3.6

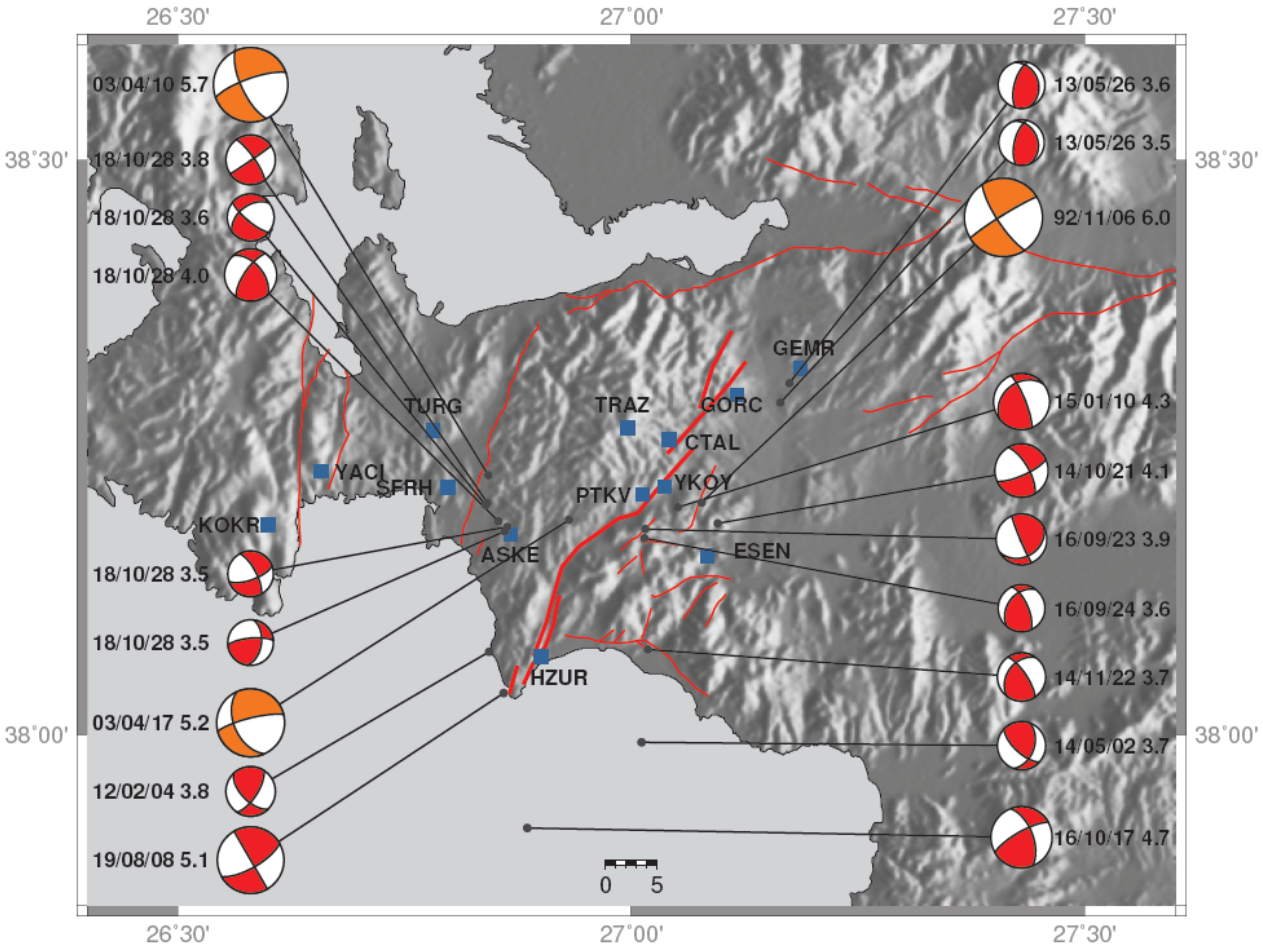

Figure 5.1. Red color indicates focal mechanism solutions of the earthquakes occurred near the Tuzla Fault after 2004. Those have red color were solved using data from Kandilli Observatory and Earthquake Research Institute. Nodal planes of the mechanism having orange color were taken from USGS [3]. All earthquakes located in the figure were re-located using seismic data (ISC and KOERI). Active Fault data were taken from (Emre et al., 2013).

Table 5.1. Earthquakes which have focal mechanism near the Tuzla Fault. Location of all earthquakes in the table were revised using the seismic data obtained from ISC and KOERI. *Strike,dip and rake were taken from USGS. Locations were re-evaluated using Hypocenter software.

Date			**Time (UTC)**	**Lat (°)**	**Long(°)**	**Depth**	**Mag.**	**Str**	**Dip**	**Rake**
Y	**M**	**D**								
1992*	**11**	**6**	19:08	27.081	38.227	12	6	147	77	-5
2003*	**4**	**10**	00:40	26.891	38.258	12	5.7	155	70	-15
2003*	**4**	**17**	22:34	26.934	38.189	5	5.2	156	50	-15
2012	**2**	**4**	20:10	26.843	38.072	15.2	3.8	136	60	25
2013	**5**	**26**	02:39	27.174	38.306	10.2	3.6	342	29	60
2013	**5**	**26**	05:37	27.164	38.289	12.5	3.5	339	30	59
2014	**5**	**2**	00:02	27.011	37.993	15.5	3.7	141	62	51
2014	**10**	**21**	03:03	27.095	38.184	10.0	4.1	330	59	-16
2014	**11**	**22**	08:57	27.018	38.074	9.0	3.7	326	74	52
2015	**1**	**10**	04:32	27.051	38.198	13.4	4.3	338	79	58
2016	**9**	**23**	05:06	27.015	38.179	11.3	3.9	157	87	60

Table 5.2. Earthquakes which have focal mechanism near the Tuzla Fault. Location of all earthquakes in the table were revised using the seismic data obtained from ISC and KOERI.

Date			**Time (UTC)**	**Lat (°)**	**Long(°)**	**Depth**	**Mag.**	**Str**	**Dip**	**Rake**
Y	**M**	**D**								
2016	**9**	**24**	04:34	27.014	38.171	10.0	3.6	336	68	55
2016	**10**	**17**	01:30	26.885	37.918	17.2	4.7	340	60	18
2018	**10**	**28**	05:40	26.860	38.177	5.8	3.5	8	51	21
2018	**10**	**28**	06:18	26.841	38.202	13.3	3.8	326	78	-2
2018	**10**	**28**	08:15	26.853	38.186	7.3	4.0	320	55	24
2018	**10**	**28**	08:19	26.863	38.181	7.1	3.5	332	71	-23
2018	**10**	**28**	21:44	26.839	38.200	6.2	3.6	131	76	-42
2019	**8**	**8**	08:39	26.872	38.047	14.4	5.1	150	90	30

6. DISCUSSION

This study has been conducted to analyze geodetic and seismic data along the Tuzla Fault in order to investigate kinematics and earthquake potential of the Tuzla fault. In this context, historical and instrumental time earthquakes were analyzed in the vicinity of the Tuzla Fault to determine the last failure of the entire fault or its individual patches. Our investigation of seismicity in historical and instrumental periods resulted that several earthquakes occurred on or near the Tuzla Fault. The first known major earthquake occurred in 178 (M 6.5) [4] along the Tuzla Fault according to the historical records. Another major earthquake occurred in 1688 (M 6.8) [6], which have a potential to simultaneously fail entire Tuzla Fault. However, since the epicenters of historical earthquakes are poorly constrained, this earthquake might even have ruptured another fault. If we presume that the last rupture occurred in 1688, approximately 332 years of slip has been currently accumulated along the Tuzla Fault.

Seismic data from International Seismological Centre allowed us to re-analyze locations of instrumental period major earthquakes. Refining the hypocenters of instrumental period earthquakes indicate that there is only one M>5.0 earthquake occurred on Tuzla Fault. This earthquake occurred on August 08, 2019 and has a potential to rupture only few kilometers of Cumalı Segment. Within the time period of our analysis, the largest event was the November 6, 1992 Mw 6.0 earthquake. Its location is however 5 km off that fault to the southeast with the location accuracy of 2.2 km and 1.7 km, in latitude and longitude, respectively.

Although there is a consensus that overall characteristic of the Tuzla Fault is strike slip fault, its detailed kinematics is still in debate. (Genç et al., 2001) investigated the area, named the Tuzla Fault as Orhanlı Fault and concluded that it is a sinistral fault. (Emre et al., 2005), however, proposes that the Tuzla Fault is a dextral fault. (Eytemiz, 2010) [33] argues that there is no proof of active faulting in Çatalca and Orhanlı segments of the Tuzla Fault but Cumalı segment has right lateral strike-slip

structure. (Göktaş, 2019) concluded that the Tuzla Fault is a strike-slip fault implying its dextral character.

The largest two earthquakes we carefully analyzed (November 6, 1992 and August 08, 2019) indicates purely dextral fault plane solutions. These structural features of earthquakes support that Cumalı and Orhanlı Segments of the Tuzla Fault have right lateral strike slip kinematics. However, there is no evidence that northern section of the Fault, namely Çatalca Segment has the same kinematics. Furthermore, maximum shear strain planes obtained from GPS measurements of stations (Section 4) indicate that Çatalca Segment might have different kinematics from Cumalı and Orhanlı Segments. Figure 4.2 demonstrate plane solutions obtained in SSPX. While western and eastern side of the CTAL-YKOY-GORC triangle have dextral mechanism, triangle itself has sinistral structure. Due to this conflict among the triangles in Figure 4.2 and insufficient seismic-geological data, which mechanism Çatalca segment has, could not verified.

Seismicity observed in the area may not be always corresponding to a fault as there might be unmapped faults [34]. In fact, (Göktaş, 2019) propose a new fault near the eastern side of the Tuzla Fault, which has not mapped before. In addition, (Genç et al., 2001) demonstrate Yeniköy Fault and smaller faults in the eastern side of the Tuzla Fault (Figure 2.1). Those Faults introduced by (Genç et al., 2001) are not included in active fault map series of Turkey prepared by (Emre et al., 2011). In this study, geometry of the Tuzla Fault were taken from (Emre et al., 2011) and integrated with the faults near the Tuzla Fault mapped by (Genç et al., 2001).

In this study, we used six epochs from fifteen-station GPS network deployed along the Tuzla Fault (2009, 2010, 2011, 2012(1), 2012(2) and 2017). GPS sessions are ten hours per epoch. Due to the fact that Aegean Region has complex structure, GPS observations applied in fifteen points can partially indicate the tectonic mechanism of the area [35]. ITRF08 were preferred in GAMIT/GLOBK. We excluded two stations, namely KPLC and URKM, since their first order processes indicated error larger than 1 mm for horizontal components, which is also in the order of expected

differential tectonic movements in the region. GPS observation of six years has been resulted southwest movement of stations with the velocity between 26.67±1.03 mm and 28.96±1.00 mm per year with respect to Eurasia (Figure 3.1) (Table 6.1). While the maximum velocities are found in KOKR and HZUR stations with 28.96±1.00 mm/yr and 28.93±0.99 mm/yr, respectively; the minimum velocity is determined in YKOY station with 26.67±1.03 mm/yr. Final velocity results of this study and velocities from (Özener et al., 2013) and (Doğru et al.,2014) [36] were compared. As a result, we saw that most of the stations were well correlated from these studies. However, differences were detected for some of the stations due to the number of the campaigns were done in the area. In addition, differences between our results and result of (Doğru et al., 2014) were expected since the velocity calculations in (Doğru et al., 2014) were done for wider area with using additional stations.

Table 6.1. Velocity vectors of stations.

Station	Velocities (mm/yr)
ASKE	28.64±0.85
CTAL	28.67±1.23
ESEN	27.10±0.94
GEMR	27.15±1.13
GORC	27.73±0.92
HZUR	28.93±0.99
KOKR	28.96±1.00
PTKV	27.42±1.05
SFRH	27.46±0.89
TRAZ	27.88±0.93
TURG	28.81±0.99
YACI	28.55±0.94
YKOY	26.67±1.03

Slip rate among stations differentiate between 1.0 to 2.0 mm annually with respect to GPS campaign results. Based on this observation, we investigate magnitude of

possible future earthquake using the moment magnitude and seismic moment relations by (Hanks and Kanamori, 1979) [37],

$$M_0 = \mu A s \tag{6.1}$$

$$M = \frac{2}{3} \log M_0 - 10.7 \tag{6.2}$$

Where μ is shear modulus (dynes/cm2), A is area, s is slip rate, M_0 is seismic moment. Crustal thickness of the Western Turkey is taken from (Tezel et al., 2013) [38]. We generate two different scenarios as the slip rates change between 1.00-2.00 mm/yr. Figure 6.1 demonstrate both scenarios.

In addition to simultaneous failure of the entire Tuzla Fault, magnitude calculations were done for every segment of the fault separately and for binary combinations of the fault segments. If individual segments of the Tuzla Fault fail independently, moment magnitude of the possible earthquakes range between Mw 6.2 and Mw 6.5. Çatalca and Orhanlı Segments can generate magnitude ranging from Mw 6.2 to Mw 6.4 according to 1 to 2mm/yr slip rates. Cumalı Segment has a potential to generate earthquake with the magnitude ranging from Mw 6.3 to Mw 6.5. Binary combinations of these segments have the potential to generate earthquakes in the magnitude range of Mw 6.4 to Mw 6.7 earthquake. In the scenario that Orhanlı and Çatalca Segments fail simultaneously, the moment magnitude can range from Mw 6.4 to Mw 6.6. In a second scenario, where Cumalı and Orhanlı Segments fail simultaneously, magnitude can range from Mw 6.5 to Mw 6.7. If the entire Tuzla Fault fails simultaneously, it can generate an earthquake with a magnitude up to Mw 6.8. As a result, for all possible scenarios, the Tuzla Fault can generate earthquake(s) in a magnitude range of Mw 6.2 - Mw 6.8. Figure 6.1 indicates all possible moment magnitudes according to two different slip rate scenario.

Strain rate solutions indicate that intersection area of Çatalca and Orhanlı Seg-

ments have the highest strain along the Tuzla Fault (Triangle 9 in Figure 4.2). Another triangle which have higher strain accumulation is 8 that includes the airport area of Izmir. These two area can host a possible future earthquake with respect to strain computations. Focal mechanisms of sixteen earthquakes which occurred near Tuzla Fault after 2003 were re-analyzed with FOCMEC program [10]. Due to the lack of seismic data, nodal planes of three earthquake occurred before 2003 in the vicinity of Tuzla Fault were taken from USGS (Figure 5.1). Focal mechanism solutions also verified Cumalı Segment has dextral kinematic (August 2019 Earthquake). In addition, the complicated structure of vicinity of the Tuzla Fault has been justified with reverse fault mechanism in the northeastern side and oblique movement in eastern side of Orhanlı Segment.

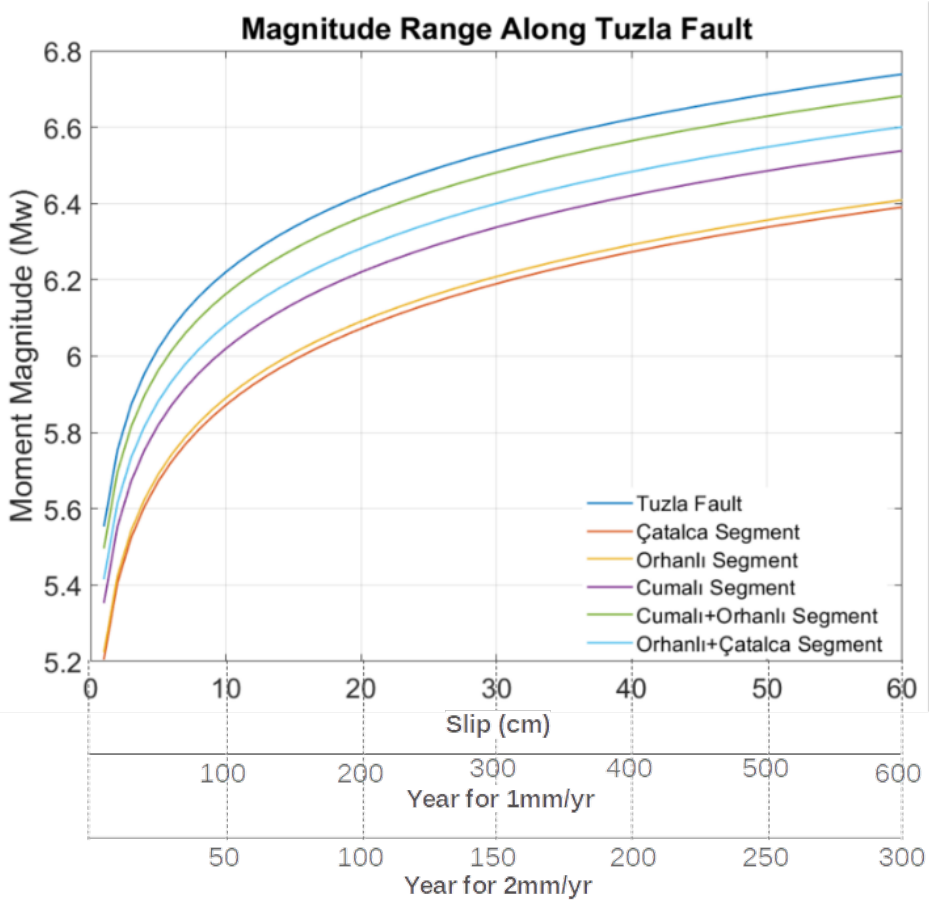

Figure 6.1. Possible moment magnitude ranges along the Tuzla Fault and for every segment in case of generating earthquakes which would not rupture the whole Fault. Two different scenarios as 1.00 mm/yr and 2.00 mm/yr slip rates were taken into account. Blue, green, cyan, purple, yellow and orange colors correspond the possible moment magnitude of Tuzla Fault, Cumalı and Orhanlı Segments together, Orhanlı and Çatalca Segments together, Cumalı Segment, Orhanlı segment and Çatalca Segment respectively. Figure indicates that 1.00 mm/yr and 2.00 mm/yr slips for 332 years can be resulted earthquake which generate magnitude from M6.4 to M6.8 for Tuzla Fault.

7. CONCLUSION

We analyzed seismographs and GPS stations to understand kinematics as well as earthquake potential of the Tuzla Fault (Izmir - Western Turkey). We refined locations of moderate size earthquakes in the study area to verify if the Tuzla Fault partially/fully failed during instrumental period. We performed fault plane solutions for moderate size earthquakes to better identify faulting mechanisms along the Tuzla Fault. We precisely positioned GPS stations at different epochs for the time period of 2009-2017 to measure velocity of lateral tectonic motion in order to elaborate on present day slip potential of the Tuzla Fault. Finally, we analyzed strain field to discriminate between creeping and locked segments as well as to confirm faulting types. Our seismic and geodetic investigations led us to draw following main conclusions,

(i) According to Fault plane solutions and maximum shear strain values and planes Cumalı segment has dextral characteristic, however, maximum shear strain planes indicates sinistral structure in Çatalca segment. Nevertheless, as there is no seismic activity in Çatalca segment in the instrumental period, this result could not be verified and supported with fault plane solutions.

(ii) Movement of the Fault area indicates southwest direction which differentiates between 26.67±1.03 mm/yr and 28.96±1.00 mm/yr with respect to Eurasia plate. Furthermore, Tuzla Fault deforms 1.00 to 2.00 mm/yr according to GPS derived tectonic velocity field.

(iii) The highest strain storage occurs at intersection zone of Orhanlı Segment and Çatalca Segment (Triangle 9 in Section 4) according to strain analysis (Figure 4.2).

(iv) Tuzla Fault is not completely failed for the last 332 years according to refined earthquake locations as well as historical records.

(v) The Tuzla Fault has currently potential to generate a magnitude Mw 6.8 earthquake. However, magnitude might be smaller if its sub-segments fail at different times. The Cumalı segment can generate an earthquake in a magnitude range

of Mw 6.3 - Mw 6.5. The Orhanlı and Çatalca segments have potential to generate two earthquakes in a magnitude range of Mw 6.2 - Mw 6.4. Simultaneous failure of Cumalı and Orhanlı segments can generate an earthquake in a magnitude range of Mw 6.5 - Mw 6.7 earthquake. Simultaneous failure of Orhanlı and Çatalca segments can generate an earthquake in a magnitude range of Mw 6.4 - Mw 6.6 (Figure 6.1).

DATA AND SOFTWARE ACKNOWLEDGEMENTS

Active Faults in Turkey and surrounding region were obtained from General Directorate of Mineral Research and Exploration.

Historical Earthquake data were obtained from (Grünthal and Wahlström, 2012), (Tan et. al, 2008) and (Emre et al., 2005). Instrumental Period Earthquakes obtained from ISC, and KOERI. Seismic phase data for re-location of instrumental earthquakes were obtained from ISC Bulletin.

GPS reference stations data were obtained from IGS.

Seismic waveform data were obtained from Kandilli Observatory and Earthquake Research Institute, Regional Earthquake-Tsunami Monitoring Center (KOERI-RETMC) in order to re-analyze the focal mechanisms of earthquakes after 2003. Seismic station network data were obtained from KOERI, USGS and AFAD. Fault plane solutions of instrumental earthquakes before 2003 were obtained from USGS.

Earthquake Location were done by using HYPOCENTER Earthquake Location Software. GAMIT used for GPS positioning process. GLOBK used for velocity analysis and producing time series. Strain analysis were done by using SSPX software. Strain calculations were done by using SSPX software and using MATLAB.

Focal plane solutions were done by using FOCMEC software.

Maps were plotted using GMT 5.4.5 [39]

REFERENCES

1. Emre, Ö., T. Y. Duman, S. Özalp, H. Elmacı, Ş. Olgun and F. Şaroğlu, "Active Fault Map of Turkey.", *General Directorate of Mineral Research and Exploration*, , No. 30, 2013.

2. Barka, A., "The north Anatolian fault zone", *Annales tectonicae*, Vol. 6, pp. 164–195, 1992.

3. USGS, *United States Geological Survey Earthquake Catalogue*, 2019, `https://earthquake.usgs.gov/earthquakes/search/`.

4. Emre, Ö., S. Özalp, A. Doğan, V. Özaksoy, C. Yıldırım and F. Göktaş, "İzmir yakın çevresinin diri fayları ve deprem potansiyelleri", *MTA rapor*, , No. 10754, 2005.

5. İzmir Sular İdaresi Başkanlığı, "İZSU Barajların son durumu hakkında rapor", , 2020.

6. Grünthal, G. and R. Wahlström, "The European-Mediterranean earthquake catalogue (EMEC) for the last millennium", *Journal of seismology*, Vol. 16, No. 3, pp. 535–570, 2012.

7. Tan, O., M. C. Tapirdamaz and A. Yörük, "The earthquake catalogues for Turkey", *Turkish Journal of Earth Sciences*, Vol. 17, No. 2, pp. 405–418, 2008.

8. Lienert, B. R. and J. Havskov, "A computer program for locating earthquakes both locally and globally", *Seismological Research Letters*, Vol. 66, No. 5, pp. 26–36, 1995.

9. Herring, T., R. King and S. McClusky, "Introduction to Gamit/Globk", *Massachusetts Institute of Technology, Cambridge, Massachusetts*, 2010.

10. Snoke, J. A., "FOCMEC: Focal mechanism determinations", *International Handbook of Earthquake and Engineering Seismology*, Vol. 85, pp. 1629–1630, 2003.

11. Genç, C. Ş., Ş. Altunkaynak, Z. Karacık, M. Yazman and Y. Yılmaz, "The Çubukludağ graben, south of İzmir: its tectonic significance in the Neogene geological evolution of the western Anatolia", *Geodinamica Acta*, Vol. 14, No. 1-3, pp. 45–55, 2001.

12. Esder, T., *Gümüldür-Cumaovası (İzmir) alanının jeolojisi ve jeotermal enerjisi olanaklarının araştırılması*, Ph.D. Thesis, PhD diss., İstanbul Ünversitesi Fen Bilimleri Enstitüsü, 1988.

13. Saroğlu, F., Ö. Emre and A. Boray, "Türkiye'nin Diri Fayları ve Depremsellikleri.", *General Directorate of Mineral Research and Exploration*, Vol. 394, 1987.

14. Emre, Ö. and A. Barka, "Gediz Grabeni-Ege Denizi Arasının (İzmir Yöresi) Aktif Fayları.", *Batı Anadolunun Depremselliği Sempozyumu*, pp. 131–132, 2000.

15. Ozener, H., A. Dogru and M. Acar, "Determination of the displacements along the Tuzla fault (Aegean region-Turkey): Preliminary results from GPS and precise leveling techniques", *Journal of Geodynamics*, Vol. 67, pp. 13–20, 2013.

16. Sabuncu, A. and H. Ozener, "Monitoring vertical displacements by precise levelling: a case study along the Tuzla Fault, Izmir, Turkey", *Geomatics, Natural Hazards and Risk*, Vol. 5, No. 4, pp. 320–333, 2014.

17. Sabuncu, A., "Investigation of crustal movement along Tuzla fault-Izmir", , 2010.

18. Ocakoğlu, N., E. Demirbağ and İ. Kuşçu, "Neotectonic structures in the area offshore of Alaçatı, Doğanbey and Kuşadası (western Turkey): evidence of strike-slip faulting in the Aegean extensional province", *Tectonophysics*, Vol. 391, No. 1-4, pp. 67–83, 2004.

19. Ocakoğlu, N., E. Demirbağ and İ. Kuşçu, "Neotectonic structures in İzmir Gulf and surrounding regions (western Turkey): evidences of strike-slip faulting with compression in the Aegean extensional regime", *Marine Geology*, Vol. 219, No. 2-3, pp. 155–171, 2005.

20. Emre, Ö. Y., S. Özalp and T. Duman, "Active Fault Map Series of Turkey, Urla (NJ 35-6) Quadrangle.", *General Directorate of Mineral Research and Exploration*, , No. 5, 2011.

21. Emre, Ö. Y., S. Özalp and T. Duman, "Active Fault Map Series of Turkey, İzmir (NJ 35-7) Quadrangle.", *General Directorate of Mineral Research and Exploration*, , No. 6, 2011.

22. Göktaş, F., "Çubukludağ Havzasındaki Neojen Tortullaşması ve Volkanizmasının Stratigrafisi, Batı Anadolu", *Türkiye Jeoloji Bülteni*, Vol. 62, No. 1, pp. 63–98.

23. Centre, I. S., "On-line bulletin", , 2001.

24. Bondár, I. and D. Storchak, "Improved location procedures at the International Seismological Centre", *Geophysical Journal International*, Vol. 186, No. 3, pp. 1220–1244, 2011.

25. KOERI, *Boğaziçi University Kandilli Observatory and Earthquake Research Institute, Earthquake Catalogue*, 2019, `http://www.koeri.boun.edu.tr/sismo/zeqdb/`.

26. Altamimi, Z., L. Métivier and X. Collilieux, "ITRF2008 plate motion model", *Journal of geophysical research: solid earth*, Vol. 117, No. B7, 2012.

27. Saastamoinen, J., "Atmospheric correction for the troposphere and stratosphere in radio ranging satellites", *The use of artificial satellites for geodesy*, Vol. 15, pp. 247–251, 1972.

28. Springer, T., G. Beutler and M. Rothacher, "A new solar radiation pressure model for GPS satellites", *GPS solutions*, Vol. 2, No. 3, pp. 50–62, 1999.

29. Halicioglu, K. and H. Ozener, "Geodetic network design and optimization on the active Tuzla fault (Izmir, Turkey) for disaster management", *Sensors*, Vol. 8, No. 8, pp. 4742–4757, 2008.

30. Havazlı, E., "Determination of Strain Accumulation along Tuzla Fault", , 2012.

31. Belhadj, A., G. B and K. S, "Triangulation of Delaunay: Application to the deformation monitoring of geodetic network by use of strain tensors", *FIG,working week*, 2012.

32. Cardozo, N. and R. W. Allmendinger, "SSPX: A program to compute strain from displacement/velocity data", *Computers & Geosciences*, Vol. 35, No. 6, pp. 1343–1357, 2009.

33. Eytemiz, C., *Sismolojik gözlemler ışığında izmir ve çevresinin depremselliğinin araştırılması*, Ph.D. Thesis, PhD diss., DEÜ Fen Bilimleri Enstitüsü, 2010.

34. Gök, E. and O. Polat, "An assessment of the microseismic activity and focal mechanisms of the Izmir (Smyrna) area from a new local network (IzmirNET)", *Tectonophysics*, Vol. 18, No. 635, pp. 154–164, 2014.

35. Aktuğ, B. and A. Kılıçoğlu, "Recent crustal deformation of Izmir, Western Anatolia and surrounding regions as deduced from repeated GPS measurements and strain field.", *Journal of Geodynamics*, Vol. 41, No. 5, pp. 471–484, 2006.

36. Dogru, A., E. Gorgun, H. Ozener and B. Aktug, "Geodetic and seismological investigation of crustal deformation near Izmir (Western Anatolia)", *Journal of Asian Earth Sciences*, Vol. 82, pp. 21–31, 2014.

37. Hanks, T. C. and H. Kanamori, "A moment magnitude scale", *Journal of Geo-*

physical Research: Solid Earth, Vol. 84, No. B5, pp. 2348–2350, 1979.

38. Tezel, T., T. Shibutani and B. Kaypak, "Crustal thickness of Turkey determined by receiver function.", *Journal of Asian Earth Sciences*, Vol. 75, pp. 36–45, 2013.

39. Wessel, P., W. H. Smith, R. Scharroo, J. Luis and F. Wobbe, "Generic mapping tools: improved version released", *Eos, Transactions American Geophysical Union*, Vol. 94, No. 45, pp. 409–410, 2013.

40. Shearer, P. M., *Introduction to seismology*, Cambridge university press, 2019.

41. Stein, S. and M. Wysession, *An introduction to seismology, earthquakes, and earth structure*, John Wiley & Sons, 2009.

42. Aki, K., "Scaling law of seismic spectrum", *Journal of Geophysical Research*, Vol. 72, No. 4, pp. 1217–1231, 1967.

43. El-Rabbany, A., *Introduction to GPS: the global positioning system*, Artech house, 2002.

44. Kaplan, E. and C. Hegarty, *Understanding GPS: principles and applications*, Artech house, 2005.

45. Dow, J. M., R. E. Neilan and C. Rizos, "The international GNSS service in a changing landscape of global navigation satellite systems", *Journal of geodesy*, Vol. 83, No. 3-4, pp. 191–198, 2009.

46. Colombo, O. L., "Ephemeris errors of GPS satellites", *Bulletin géodésique*, Vol. 60, No. 1, pp. 64–84, 1986.

47. Hofmann-Wellenhof, B., H. Lichtenegger and E. Wasle, *GNSS–global navigation satellite systems: GPS, GLONASS, Galileo, and more*, Springer Science & Business Media, 2007.

48. Xu, G. and Y. Xu, *GPS: theory, algorithms and applications*, Springer, 2016.

49. Kurt, A. İ., *Sabit GPS istasyonları zaman serileri analizinden yararlanarak kampanya tipi GPS ölçülerinin hızlarının iyileştirilmesi*, Ph.D. Thesis, Fen Bilimleri Enstitüsü, 2009.

50. Altamimi, Z., D. Angermann, D. Argus, G. Blewitt, C. Boucher, B. Chao, H. Drewes, R. Eanes, M. Feissel, R. Ferland *et al.*, "The terrestrial reference frame and the dynamic Earth", *Eos, Transactions American Geophysical Union*, Vol. 82, No. 25, pp. 273–279, 2001.

51. Herring, T., R. King and S. McClusky, "GAMIT", *Refer ence Manual. GPS Analysis at MIT. Release*, Vol. 10, pp. 1–182, 2006.

52. Herring, T., R. King and S. McClusky, "GLOBK", *Global Kalman filter VLBI and GPS analysis program, version*, Vol. 10, 2005.

53. RETMC, *Boğaziçi University Kandilli Observatory and Earthquake Research Institute Regional Earthquake-Tsunami Monitoring Center*, 2019, `http://www.koeri.boun.edu.tr/sismo/2/deprem-verileri/sayisal-veriler/`.

APPENDIX A: METHODS

In this section theoretical background of the methods applied in the study were described briefly.

A.1. Earthquake Location and Magnitude

A.1.1. Types of Waves

Energy generated by earthquakes is partly propagated into the Earth's crust and interiors as seismic waves. There are different types of seismic waves, e.g., P-wave (compressional), S-wave (shear) and Reighly and Love (surface waves) [40]. These waves are primary data to detect, locate and characterize earthquakes sources as well as structure of the Earth's interiors.

Seismic waves are mainly categorized as body waves and surface waves according to their traveling process. While body waves travel through inner layers of the Earth, surface waves propagate along the layers near the Earth's surface [41] (Figure A.1). Body waves cover two different seismic waves namely P and S waves. P waves, in other words compresional waves, can move along both fluids and solid rocks. They are the fastest seismic waves, and therefore they firstly reach the seismic station although P- and S- waves emerge from the earthquake source simultaneously. Second wave arriving to the station is known as S wave, or shear wave which can travel through only the rocks. Surface waves, which have larger amplitude, arrive later than body waves. Surface waves are classified as Love and Rayleigh waves, which have more destructive effect on engineering structures compared to body waves. Literally, we generally feel surface waves rather than body waves following major earthquakes. These waves are the main reason why the earthquakes are named as disaster. Figure A.1B illustrates schematically the behavior of both Body waves and Surface waves.

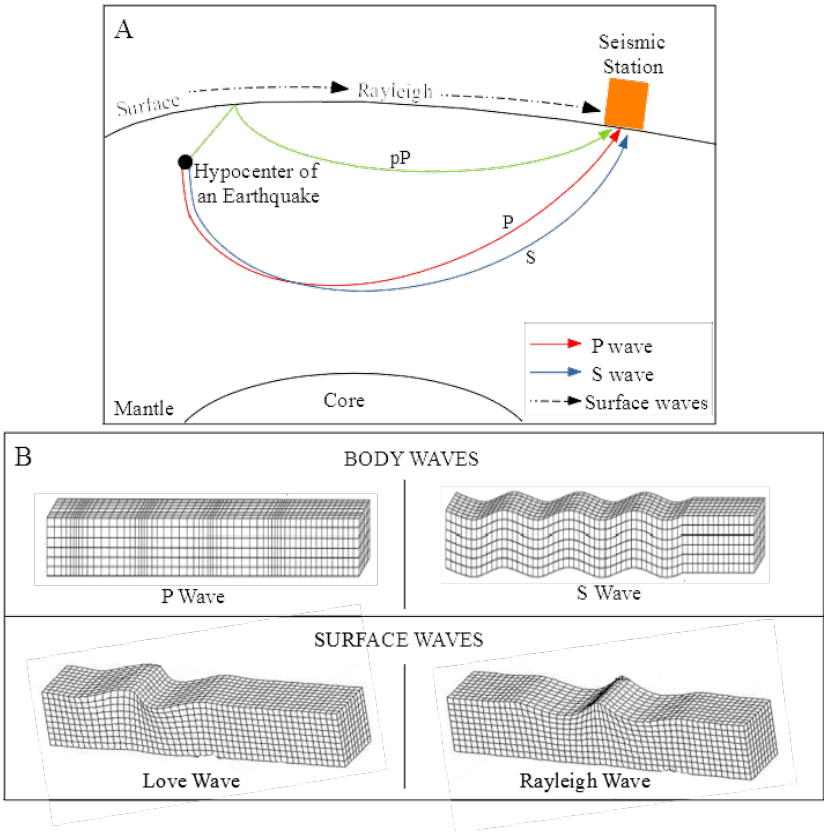

Figure A.1. A illustrates typical propagation paths of seismic waves. B indicates types of motions generated by different seismic waves.

A.1.2. Hypocenter of an Earthquake

Earthquake location is so-called "hypocenter" in 3D space representing its latitude, longitude and depth. Its location in 2D space, in other words as latitude and longitude, is so-called "epicenter". Both are located using arrival times of seismic waves at seismic stations originating from the earthquake source (mainly P and S waves). In order to determine the travel times, we use seismograms, which are instantaneous and sensitive records of the Earth's movements. To introduce the logic behind, locating an earthquake epicenter is simply exemplified below:

When an earthquake occurs and signals begin to travel, P and S waves arrive at seismic station in chronological order as they have different propagation velocity (e.g.

firstly P and secondly S wave). As their velocity and arrival time to the seismic station are roughly known, distance between station and event can be calculated as follows:

$$\frac{\sqrt{(x-x_i)^2+(y-y_i)^2}}{\vartheta} = t_i \tag{A.1}$$

where *(xi,yi)* are station coordinates, *(x,y)* are unknown coordinates of an event, V is seismic velocity and t is travel time. Equation A.1 can be simplified for both P and S wave arrival times as;

$$\frac{D}{V_s} = t_s \text{ and } \frac{D}{V_p} = t_p \tag{A.2}$$

where V_p and V_s seismic velocities, t_p and t_s travel times, for P and S waves respectively. D is the event – station distance. Differential travel times then becomes;

$$D\left(\frac{V_p - V_s}{V_p V_s}\right) = t_s - t_p \tag{A.3}$$

Therefore, distance can be measured using differential times (S-P times) using seismic velocity. If there is one station, only a single great circle can be obtained for the epicentral distance D. In order to obtain epicenter of an event, at least three seismic stations are needed to be used. (Figure A.2)

There are two main earthquake location methods, namely absolute location method and relative location method [40]. In absolute earthquake location method, starting from an initial model, least square technique is used to optimize the location based on data misfit. Firstly, final location are specified as follows,

$$X = X_0 + \Delta X \tag{A.4}$$

Where X is the final location (2D or 3D), X_0 is modeled location (2D or 3D), which can be an initial location, or a stepwise-optimized location at a particular iteration,

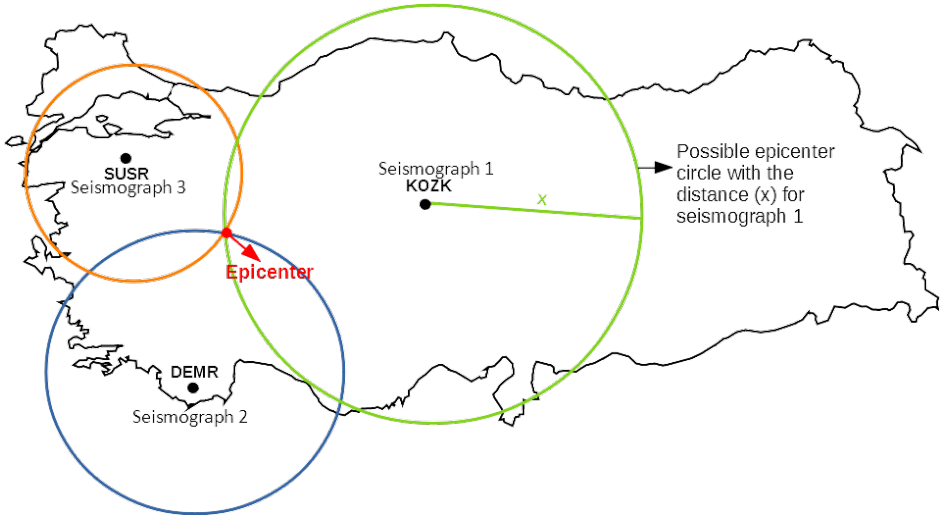

Figure A.2. Illustration of epicenter of a possible earthquake. Seismic Stations in the map are operated by Kandilli Observatory and Earthquake Research Institute (KOERI hereafter).

and ΔX distance between final location and modeled location. The modeled travel time at X can be estimate via Taylor series:

$$t_i^p(X) = t_i^p\left(X_0\right) + \frac{\partial t_i^p}{\partial X_j}\Delta X_j \tag{A.5}$$

Residual at X:

$$\begin{aligned} r_i(X) &= t_i - t_i^p(X) \\ &= t_i - t_i^p\left(X_0\right) - \frac{\partial t_i^p}{\partial X_j}\Delta X_j \\ &= r_i\left(X_0\right) - \frac{\partial t_i^p}{\partial X_j}\Delta X_j \end{aligned} \tag{A.6}$$

Then the equation can be written as below,

$$r_i\left(X_0\right) = \frac{\partial t_i^p}{\partial X_j}\Delta X_j \tag{A.7}$$

or

$$r\left(X_0\right) = A\Delta X \tag{A.8}$$

Where A is the matrix of partial derivatives. This procedure continues until final location and current assumption converges each other. In other words, ΔX converges to zero as much as possible.

In this study, "HYPOCENTER" earthquake location program is used to perform absolute earthquake location [8]. Figure A.3 indicates flowchart of the program. P- and S-wave arrivals are manually marked if digital waveform data are available. If not, they are obtained from bulletins of the International Seismological Centre [**?**]. Arrival times are prepared in NORDIC format as an input for HYPOCENTER program. For final locations, we excluded arrival times with large residuals (>1.0 s).

Flowchart of the HYPOCENTER in Figure A.3 indicates the main steps of the program. In order to begin the location calculations, parameters and station information should be organized as NORDIC format as an initial step. Due to the fact that every arrival time and information of station location will affect the overall result for the hypocenter determination, program will apply consistency test. Furthermore, program allows the user to apply residual weighting to increase the accuracy. After the phase data set was imported to the program correctly, program will begin to calculate the hypocenter of an earthquake. This method continues until final location and current assumption converges each other and finally gives the output solution with its error.

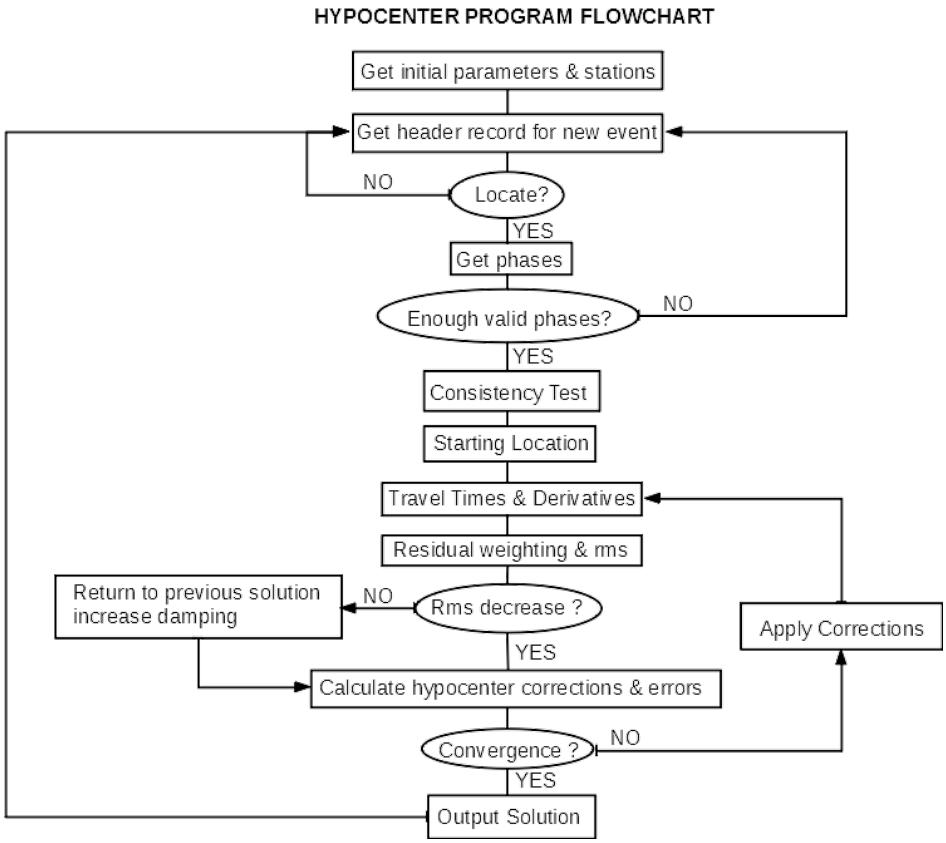

Figure A.3. Flowchart of the HYPOCENTER earthquake location program.

A.1.3. Magnitude of an Earthquake

There are several ways to calculate the magnitude of an earthquake. Nevertheless, moment magnitude is widely used and the only physical method today to represent magnitude of an earthquake. It is not saturated beyond certain magnitude range. Therefore it covers entire range of earthquake size and can be applied globally.

Moment Magnitude depends on seismic moment, which is measure of rupture size related to force couples across area of fault slip [42].

$$M_0 = \mu A s \tag{A.9}$$

Where M_0 is seismic moment, μ is shear modulus (dynes/cm^2), A is the faulted area

and s is the average slip along the ruptured fault (Figure A.4).

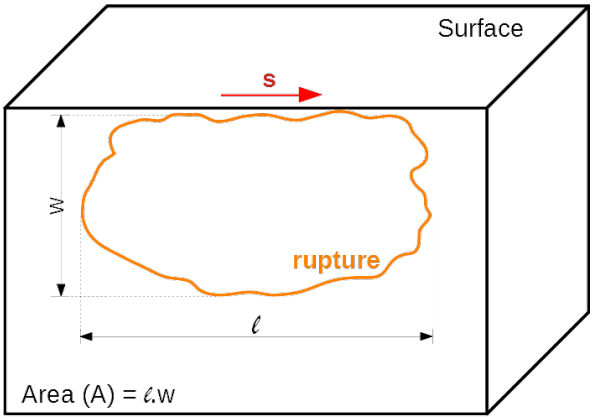

Figure A.4. Variables which are used for calculating seismic moment and moment magnitude. s represents the average slip along the fault, l is length of the fault and w is the width of the fault.

Using the seismic moment M_0, moment magnitude can be written as below [37],

$$M = \frac{2}{3}\log M_0 - 10.7 \tag{A.10}$$

In this research, magnitudes of instrumental earthquakes were obtained from Earthquake Catalogue of Kandilli Observatory and Earthquake Research Institute.

A.2. Global Navigation Satellite System

The Earth's surface is dynamic due to plate tectonics as the plates move in horizontal and vertical axis. These movements are mostly steady state at a scale of mm/yr rates in inter-earthquake periods. During earthquakes, when strain energy stored over the time periods of hundred years releases in few seconds, they might move unstably at a scale of meters. To characterize this ongoing change of the Earth's crust, four main space techniques are used for computing accurate coordinates with respect to globally well-defined reference frame. Among them, Global Navigation Satellite

System (GNSS hereafter) is widely used for better understanding the dynamics of the Earth, such as tectonic motions, plastic and elastic deformations of the crust, and characterization of faults.

GNSS is a worldwide system to obtain position and time of a particular point using radio signals which are seperated as pseudorange code measurements and carriers phase measurements. There are two different pseudorange code measurements namely C/A (coarse acquisition) and P-code (precision). While C/A code contains 1023 binary digits (1.023 MHz) and repeat itself every millisecond, P-code contains 10230 binary digits (10.23MHz) and repeat itself after 266 days [43]. The resolution of the codes accepted as 1% of the chiplength. Therefore, while C/A code has 3 meter resolution, P-code has 30 cm resolution since the length of the chiplength corresponds 300 meters and 3 meters, respectively. On the other hand, in carrier phase measurements, there are two main sine waves used as GPS signal namely L1 and L2 carrier. Frequencies of these carriers are generated at 1575 MHz and 1227 MHz which equal to 19 cm and 24.4 cm respectively. Therefore, since the carriers' lengths are smaller than the pseudorange codes' chiplengths, carrier phase measurements are much more accurate than code measurements. Phase and code measurements provide two different satellite ephemerides namely precise ephemerides and broadcast ephemerides, respectively. While accuracy of the broadcast ephemerides has approximately 100 cm, accuracy of the data in precise ephemerides differentiates whether it is final, rapid or ultra rapid. However, all data obtained from precise ephemerides are better accuracy than 3 cm. In order to obtain 3D location of a point, a reference coordinate system has to be chosen for both satellite and receiver. It is beneficial to use Earth Centered Inertial Coordinate System (ECI) to measure and determine the orbits of GNSS satellites since the movement of satellites follows the Newtonian mechanics which are indicated accurately in an inertial coordinate system [44] and Earth-Centered Earth-Fixed (ECEF) Coordinate system is useful for positioning GNSS stations on the surface of the earth.

GNSS mainly consists of three segments, namely space, control and user segments. Space segment includes GPS satellite constellation. Every satellite sends a

signal (L-band) containing carrier frequencies and codes which are used to calculate distance between satellite and receiver. These signals travel from satellites to the control segment. Main responsibility of the control segment is observing the satellites and determining the information such as their locations or atomic clocks. After these informations were obtained, data are sent back to the satellite through S-band. User segment covers all users around the world including civillians and military.

GNSS receivers are designed to collect time data for which this specific frequency band to resolve latitude, longitude and altitude/elevation of target locations with high precision. Several constellations are available operated by different countries/unions (Table A.1). GPS, which is the GNSS constellation of USA, has thirty-one operational GPS satellites orbiting twice a day in MEO (Medium Earth Orbit) at an altitude of 20200 km. GNSS constellation of China, namely BeiDou (BDS), has been still in operation since the late twentieth century and currently consists of operational satellites, of six GEO (geostationary orbit), twenty-one MEO and six IGSO (inclined orbit) satellites. Galileo, EU's GNSS constellation, consists of twenty-four satellites in MEO. (European Space Agency) and GLONASS with twenty-four operational satellites, operating by Russia. Table A.1 lists specifications of all these constellations.

International GNSS Service (IGS), operating by International Association of Geodesy (IAG), provides GNSS data, navigation, positioning, timing, and terrestrial reference frame products working together over 200 self-funding agencies, research institutions and universities in more than 100 countries worldwide [45]. In this study, thirteen IGS stations were used for stabilization.

A.2.1. GNSS Error Sources

GNSS have several types of random errors and biases due to the satellites, receivers and atmospheric signal propagations. As the initial outcome of the GNSS signals is the distance between satellite and receiver, all errors and biases affect the distance between them.

Table A.1. Global Navigation Satellite Systems which are commonly used.

System	**GPS**	**GALILEO**	**GLONASS**	**BEIDOU**
Owner	United States	EU	Russia	China
Geodetic Reference System	WGS-84 GPS time, UTC (USNO)	GTRF Galileo system time	PZ-90 GLONASS time, UTC(SU)	CGS2000 Bei Dou System Time (BDT)
Number of Satellites	31	10 Healthy 12 Orbiting	24	33
Coverage	Global	Global	Global	Global
Altitude	20200 km	23222 km	19100 km	21528 km
Period	11 h 58 m	14 h	11h 15m	12 h 53 m
Orbital Inclination	55°	56°	64.8°	55°

- Ephemerides / Orbit Errors : Satellite positions are determined using ground control stations of GNSS. Ephemerides errors are occurred when accuracy of the satellite navigation message gets below certain threshold. Generally, satellites cannot be perfectly positioned and therefore ephemerides errors range between from 2 to 5 meter [43]. The impact of ephemerides errors on baselines can be assessed as follows [46]:

$$\frac{e_b}{l_b} = \frac{e_e}{r_s} \tag{A.11}$$

  where e_b is baseline error, l_b is baseline length, e_e ephemerieds error and r_s range of satellite

- Satellite and Receiver Clock Errors: The positioning is basically performed by travel time data, so system clocks are crucial for accuracy of positions. Every satellite contains atomic clock to determine the time precisely. As the GNSS signals travels with light speed, travel times are too small. In this context, even small clock errors can generate large positioning errors. For instance, nine nanoseconds

(10^{-9}) timing error in satellite clock would result in 2.7 meter positioning error for the satellites. GNSS receivers, however, use another clock type, so-called "crystal clocks", of which the accuracy much lower than the atomic clock. Master control station resolves the correction parameters for satellite error as a second-order polynomial equation, which are then used for time correction in the receiver [44]:

$$d_{ts} = a_0 + a_1 (t - t_0) + a_2 (t - t_0)^2 + \Delta t \tag{A.12}$$

Where, a_0, a_1 and a_2 are clock bias, clock drift and frequency drift, respectively. t time epoch of the measurement, t_0 is the reference time and Δt is the correction of relativistic effects. Satellite and receiver clock errors can be eliminated using single and double differencing methods as described in section A.2.4

- Multipath Error: Multipath error is one of the significant errors in GNSS measurements. This type of error occurs if the signal propagated from satellite did not directly arrive at the receiver, but rather reflected through an object such as trees, buildings, snow or water before it arrives. Since reflected signal arrives to the receiver later than its absolute arrival, arrival time from satellite to the receiver increases artificially and eventually, calculated satellite-station distance will be larger than absolute distance.

  To avoid this error, position of the antenna should be chosen carefully. In addition, cut off angle can be set as 10° or 15°. Another option is to use choke ring antennas, which are able to eliminate reflected signals.
- Antenna Phase Center Variations: Antenna phase center is the location where exactly the GNSS signal is received. In most cases, geometrical center of the antenna does not overlap with phase center of antenna since phase center differentiates with respect to altitude and azimuth of the satellite. Consequently, few centimeters of positioning error can be generated by variations of antenna phase centers [43]. To eliminate this error, ideally same types of antennas should be used and antennas are oriented to the same direction (e.g. North).
- Ionospheric Effect: Ionosphere is the part of the atmosphere between fifty km and 1000 km above the Earth where molecules are in ionized form [47]. The

number of negatively charged free electrons is excessive that those can change the propagation speed of the GPS signal. While the speed of propagation increases for carrier phase measurements (phase advance), it decreases for code measurements (code delay). Different options can be use to eliminate this error type:

- Using dual frequency (L1 and L2) combination: For dual frequency, ionospheric effect is indicated as below,

$$\delta(f_1) = \frac{A}{f_1^2} \text{ and } \delta(f_2) = \frac{A}{f_2^2} \tag{A.13}$$

  Where A is the integral of -40.3N_e (electronic density) and f is frequency. Using these two equation, we can obtain following equation which is eliminate the ionospheric effect [48],

$$f_1^2\delta(f_1) - f_2^2\delta(f_2) = 0 \tag{A.14}$$

- Setting the baselines under 20 km: Since ionospheric effect is accepted same if the baselines are shorter than 20 km, establishing a network under this distance can be a solution for ionospheric effect.

- Tropospheric Effect: Troposphere is the lowest and electrically neutral layer of the atmosphere. Since GPS signals are between 1 and 2 GHz and troposphere is unscattered environment for frequencies below 15 GHz, it delays both code and carrier phase measurements. As tropospheric effect is not dependent to the frequency, it cannot be eliminated using L1 and L2 observations. In order to remove this effect, some tropospheric models are used:
  Essen Framei (1963)
  Modified Hopfield Model (1969,1970,1972)
  Saastamonien (1972 and 1973)
  Davis (1985)
  Herring (1987)
  Niell (1996)

- Cycle Slips and Initial Phase Ambiguity: When a signal reached to a receiver in at time t_0 , the receiver can only measure a fraction of a cycle, not a total number of the complete cycles. Therefore, total number of complete cycles remains unknown and is called as initial phase ambiguity. While the GPS observations are lasting, any problem which is resulted loss of GPS signals is called cycle slip. This discontinuity can be due to the trees, buildings, mountains or any other objects between GPS signal and receiver.

A.2.2. Point Positioning

The main idea of point positioning one receiver with unknown coordinates is to determine its location via obtaining the code or phase measurements (travel time data) from four or more satellites of which geocentric positions are known (Figure A.5). For a stable inversion, number of measurements should be equal or greater then number of unknown parameters. As there are four unknowns, (receiver clock error and 3D coordinates), the receiver needs at least four satellites to obtain the position [43,47,48].

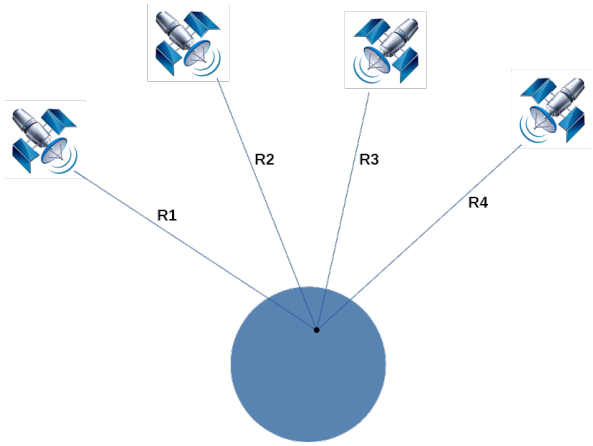

Figure A.5. Demonstration of point positioning. R1, R2, R3 and R4 indicate geometrical distance between satellite and receiver.

A.2.2.1. Point positioning with code measurements. Pseudorange code measurement at an epoch t can be written as below,

$$R_r^s(t) = \rho_r^s(t) + c\Delta d_r^s(t) \tag{A.15}$$

Where R_r^s (t) is the observed pseudorange between receiver (r) and satellite (s), $\rho_r^s(t)$ is the distance between receiver and satellite, c is speed of light, Δd_r(t) is clock bias. The distance $\rho_r^s(t)$ can also be demonstrated as follows,

$$\rho_r^s(t) = \sqrt{(X^s(t) - X_r)^2 + (Y^s(t) - Y_r)^2 + (Z^s(t) - Z_r)^2} \tag{A.16}$$

Here X^s(t), Y^s(t),Z^s(t) indicates coordinates of the satellite and X_r, Y_r, Z_r show receiver coordinates. In addition, the clock bias can be reorganised as,

$$\Delta d_r^s(t) = d_r(t) - d^s(t) \tag{A.17}$$

Eventually, equation A.15 is formed as,

$$R_r^s(t) + cd^s(t) = \rho_r^s(t) + cd_r(t) \tag{A.18}$$

A.2.2.2. Point Positioning with carrier phase measurements. Carrier phase measurements can also be used for point positioning using the same formula at equation A.15 for code measurements with slight changes,

$$\Phi_r^s(t) = \frac{1}{\lambda^s}\rho_r^s(t) + N_r^s + \frac{c}{\lambda^s}\Delta d_r^s(t) \tag{A.19}$$

Where, Φ_r^s(t) is observed carrier phase between receiver and satellite, λ is wavelength,$\rho_r^s(t)$ is the distance between receiver and satellite, N is ambiguity, c is speed of light and Δd_r^s (t) is clock bias.

A.2.3. Relative positioning

In relative positioning, a baseline is measured from a reference station, of which the location is assumed to be exactly known, to a point, which is to be located. This process can be real time with low accuracy, or using post-processing techniques in high accuracy. While post-processing method allows processing raw data obtained from different GNSS receivers simultaneously, real time data are processed at each receivers individually. Schematic demonstration of relative positioning in Figure A.6 can be analytically written as,

$$X_B = X_A + b_{AB} \tag{A.20}$$

Where A is known position, B is unknown position and b_{AB} is the baseline between A and B. There are mainly five different relative positioning methods:

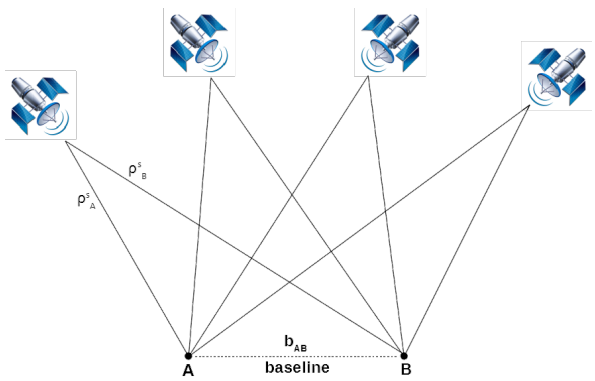

Figure A.6. Schematic demonstration of Relative positioning: ρ_A^s and ρ_B^s indicate the distances between satellite and points.

- Static Surveying (5mm+1ppm)
- Fast (rapid) Static Surveying (5-10mm + 1ppm)
- Repetitive/reoccupation Measurements (1 cm+1ppm)

- RTK Surveying (1-2 cm+1ppm)
- Stop and Go (1-2 cm+1ppm)

Accuracy of relative positioning depends on preferred positioning method as well as length of data since the length of the data directly affect the mathematical model used for environmental and instrumental errors. In this study, ten-hours of static surveying campaigns were performed. Totally six epochs were recorded for the time period of 2009-2017.

A.2.4. Phase Differences in Relative Positioning

Using phase differences in relative positioning allows minimizing errors or biases due to unknown effects along the travel paths between satellites and GNSS stations. There are three basic types of phase differences used in relative positioning.

A.2.4.1. Single Differences. Combination of two GNSS receivers, which simultaneously record arrival time of the signals originating from the same satellite, can resolve satellite clock error since all data receivers obtained contains approximately same error. Hence, difference between the measurements at these receivers can remove the satellite-related data noise efficiently (Figure A.7). Equation between receiver A-B and satellite S1 can be defined as follows:

$$\Delta L_{AS1} = \Delta\rho_{AS1} + c\Delta d_{S1}(t) + c\Delta d_A(t) + \Delta N_{AS1} + \Delta rel_{AS1} + \Delta trop_{AS1} + \Delta Ion_{AS1} \quad \text{(A.21)}$$

$$\Delta L_{BS1} = \Delta\rho_{BS1} + c\Delta d_{S1}(t) + c\Delta d_B(t) + \Delta N_{BS1} + \Delta rel_{BS1} + \Delta trop_{BS1} + \Delta Ion_{BS1} \quad \text{(A.22)}$$

and the difference between two equation is,

$$\Delta L_{ABS1} = (L_A - L_B) = \Delta\rho_{ABS1} + c\Delta d_{AB}(t) + \Delta N_{ABS1} + \Delta rel_{ABS1} + \Delta trop_{ABS1} + \Delta Ion_{ABS1} \tag{A.23}$$

Where, L_{ij} is single difference between i and j, ρ_{ij} is geometrical distance between i and j, c is speed of light , d is clock error, N is ambiguity. Rel, trop and Ion are relativistic effect, tropospheric effect and ionospheric effect, respectively. The number of single

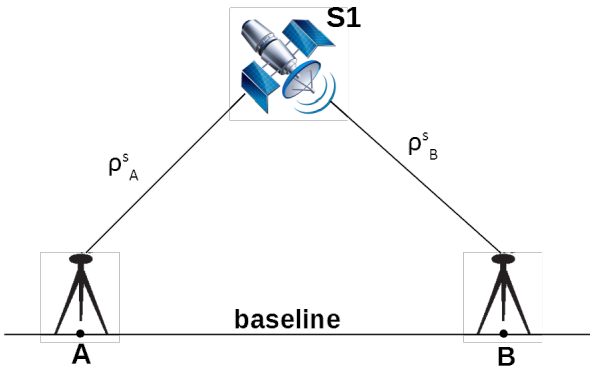

Figure A.7. Demonstration of single differences. ρ_A^s and ρ_B^s indicate the geometrical distances between the satellite S1 and the stations A and B.

differences can be found using the following formula,

$$n = RxSxT \tag{A.24}$$

Where n is the number of single differences, R is the number of receiver, S is the number of satellite and T is the number of epoch.

A.2.4.2. Double Differences. Double differences can be defines as difference between two single difference (Figure A.8). That is,

$$\Delta\nabla L_{ABS1S2} = \Delta L_{ABS1} - \Delta L_{ABS2} \tag{A.25}$$

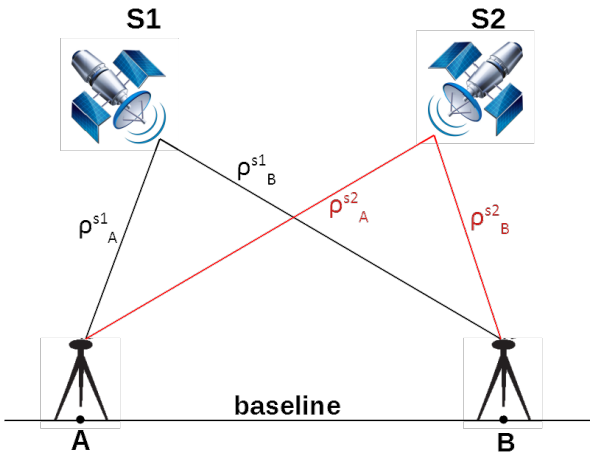

Figure A.8. Demonstration of double differences. ρ_A^{s1} and ρ_B^{s1} indicate the geometrical distances between the satellite S1 and the stations A and B. ρ_A^{s2} and ρ_B^{s2} indicate the geometrical distances between the satellite S2 and the stations A and B.

In addition to satellite clock error, receiver clock error can also be eliminated using double difference method. It should be noted that since the satellite and receiver clock error is the largest error source among other errors and biases, eliminating them affects the accuracy of the positioning significantly.

The number of double differences can be calculated as follow,

$$n = (R-1)x(S-1)xT \tag{A.26}$$

A.2.4.3. Triple Differences. Triple differences are obtained from two double differences in two different epoch, t_i and t_{i+1}, and can be define as difference between two double difference (Figure A.9),

$$\Delta\nabla\Delta L_{ABS1S2}\left(t_{i+1}, t_i\right) = \Delta\nabla L_{ABS1S2}\left(t_{i+1}\right) - \Delta\nabla L_{ABS1S2}\left(t_1\right) \tag{A.27}$$

The number of triple differences can be computed as,

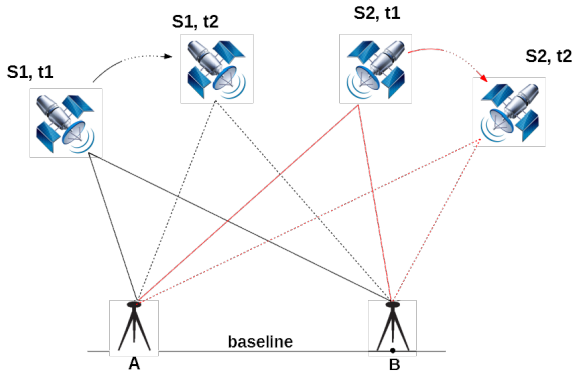

Figure A.9. Demonstration of triple differences. Black solid and dotted lines indicate distances between the satellite S1 and the stations A and B at the times t1 and t2, respectively. Red solid and dotted lines indicate distances between the satellite S2 and the stations A and B at the times t1 and t2, respectively.

$$n = (R-1)x(S-1)x(T-1) \tag{A.28}$$

In triple difference method, ambiguity and cycle clips are eliminated in addition to satellite and receiver clock errors. However, due to the fact that using triple differences decreases the accuracy and stochastic model becomes more complicated, this method is only used for finding outliers or significant errors.

A.2.5. Accuracy in GPS observation

To be able obtain measurements precisely, conditions needs to be prepared appropriately. Accuracy in GPS measurements mainly depend on following elements,

- Receiver and Antenna Type

  Double frequency receivers which have an ability to eliminate ionosphere effect and geodetic antennas should be preferred such as choke ring antennas to decrease the multipath effect.
- Duration of Measurements

Due to the fact that longer measurement time decreases the standard deviation and therefore increases the accuracy, static GPS measurements which are done at least eight-hour observations are one of the crucial fact in order to obtain precise positions of the stations.

- Number of Satellites

  The number of satellites are affecting the accuracy as location coordinates are produced for every satellite. Although four satellite is enough in order to solve the unknown parameters, obtaining more accurate data depends on the number of satellites.

- Satellite Geometry (Dilution of Precision - DOP)

  Positions of the GPS satellites ,whether they are separated equally or not with respect to the location of the station, affect the accuracy of the GPS measurements. Numerical quality of the positions of GPS satellites is called DOP (dilution of precision). There are three types of DOP which are,

  PDOP (Positional dilution of precision)

  TDOP (Time dilution of precision)

  GDOP(Geometrical dilution of Precision)

  Higher DOP value corresponds lower quality of satellite geometry.

- Using IGS product

  Using precise GPS satellite ephemerides , coordinates and velocities of IGS stations in ITRF system, earth tide and ocean loading tide corrections, information of ionosphere and troposphere are crucial to produce precise location.

- Post-Processing

  Using commercial software is efficient in local GPS studies which have smaller baselines than 20 km, since commercial softwares are not ionosphere-free. However, academic softwares such as BERNESE(University of Bern), GAMIT (MIT) or GIPSY (NASA JPL) are crucial to obtain high accuracy for regional or global GPS process.

A.2.6. Time Series Analysis

Time series can be described as set of measurements for a value performed at different times. In geodesy, time series are used for determining the position differences of the stations, and therefore, slip rates and corresponding uncertainties. These measurements allow characterizing crustal movements in tectonically active regions at different stages of the the earthquake cycle, namely inter-seismic, pre-seismic, co-seismic and post-seismic periods. [49]. Figure A.10 indicates time series of PTKV station for North and East component from 2009 to 2017.

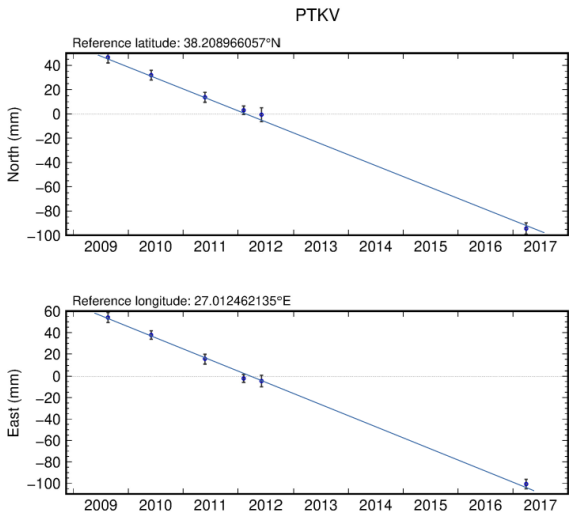

Figure A.10. North and East component of time series of PTKV between 2009 and 2017.

In order to obtain velocity from time series, LSQR adjustment is applied combining a set of following linear equation,

$$X\left(t_i\right) = X_0 + rt_i + \varepsilon_x(t) \tag{A.29}$$

Where $x_{(ti)}$ is time series in t_i , X_0 is the point where the line crosses the x axis, r is slope, ε_x(t) is error

Since the crustal motions remain below 1.0 mmm/year except for active plate boundaries, GNSS campaigns, should continue more than five years to provide required accuracy [50]. In this research, GAMIT/GLOBK academic software [51, 52] was used to position GNSS station and analyze their time series. Totally six epochs of campaign-based GPS measurements were performed for the time period of 2009-2017

A.3. Strain Analysis

Strain is one of the fundamental elements of the investigating kinematics and earthquake potential of faults since it quantifies amount and direction of accumulated deformation. According to the Hooke's Law, when a force was applied to a stable material, its shape begins to change with respect to the direction of the force. This change becomes elastic deformation when the material have an ability to turn back to its initial form in absence of the applied force. However, if material strength is exceeded by the applied force, the deformation becomes permanent, which is called plastic deformation. When material reaches its ultimate strength, fractures begin to form inside they gather when final failure occurs. In tectonic environment, this plastic failure is so-called earthquake.

A.3.1. Stress and Strain

Stress can be defined as the force per unit area and strain can be basically described as the deformation of an object under the stress. Equations of the strain and stress can be written as below,

$$\varepsilon = \frac{dL}{L} \quad ; \quad \tau = \frac{P}{A} \tag{A.30}$$

Where ε and τ represent strain and stress, dL is change in length , L is the original length, P is force and A is area. There are mainly three different type of stress and strain namely, tensile, compressive and shear (Figure A.11). While tensile stress and strain occurs when the force is applied to stretch the material, compressive stress and

strain occur when the force is applied to compress the material. Figure A.11 displays types of strains as a result of force/stress applied to elastic material.

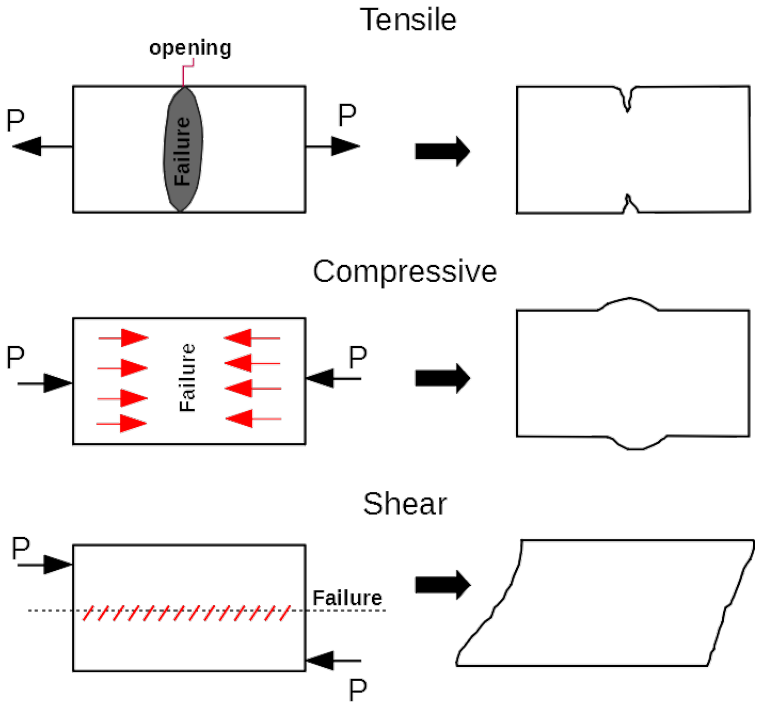

Figure A.11. Tensile, compressive and shear stress and strain. P indicates the applied force.

A.3.2. Computing Value of a Strain Using Slip Rate

The functions of the deformation can be represented as first-degree polynomial equation as follows [31] ,

$$dX_i = a_2 X_i + a_3 Y_i \tag{A.31}$$

$$dY_i = a_5 X_i + a_6 Y_i \tag{A.32}$$

where a_2, a_3, a_5 and a_6 are unknown coefficients, X_i and Y_i are the coordinates of the triangle, dX_i and dY_i are annual displacements of points. In matrix form, equations of

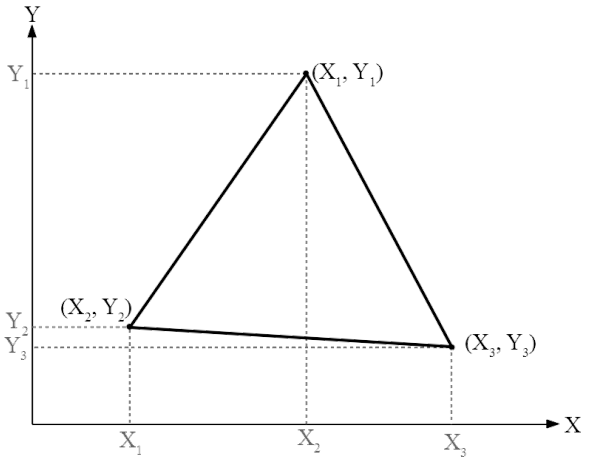

Figure A.12. Example of Delaunay triangle. X_i and Y_i indicate coordinates of the points.

(A.31) and (A.32) are:

$$\begin{bmatrix} dX_1 \\ dY_1 \\ dX_2 \\ dY_2 \\ dX_3 \\ dY_3 \end{bmatrix} = \begin{bmatrix} X_1 & Y_1 & 0 & 0 \\ 0 & 0 & X_1 & Y_1 \\ X_2 & Y_2 & 0 & 0 \\ 0 & 0 & X_2 & Y_2 \\ X_3 & Y_3 & 0 & 0 \\ 0 & 0 & X_3 & Y_3 \end{bmatrix} * \begin{bmatrix} a_2 \\ a_3 \\ a_5 \\ a_6 \end{bmatrix} \tag{A.33}$$

$$l = Ax \tag{A.34}$$

Partial derivatives of coordinates in the equation, in other words, the components of the deformation tensors were adjusted by the least squares method. The components of the deformation tensor for Figure A.12 are :

$\varepsilon_{xx} = a_2$

$\varepsilon_{xy} = a_3$

$\varepsilon_{yx} = a_5$

$\varepsilon_{yy} = a_6$

Dilatation, maximum and minimum shear and rotation are defined as follows,

$$\lambda_D = \frac{1}{2}\left(\varepsilon_{xx} + \varepsilon_{yy}\right) \text{ Dilatation} \tag{A.35}$$

$$\gamma = \frac{1}{2}\sqrt{\left(\varepsilon_{xx} - \varepsilon_{yy}\right)^2 + \left(\varepsilon_{xy} + \varepsilon_{yx}\right)^2} \text{ Total Shear} \tag{A.36}$$

$$\lambda_1 = \frac{\varepsilon_{xx} + \varepsilon_{yy}}{2} + \frac{1}{2}\sqrt{\left(\varepsilon_{xx} - \varepsilon_{yy}\right)^2 + \left(\varepsilon_{xy} + \varepsilon_{yx}\right)^2} \text{ Principal Component*} \tag{A.37}$$

$$\lambda_2 = \frac{\varepsilon_{xx} + \varepsilon_{yy}}{2} - \frac{1}{2}\sqrt{\left(\varepsilon_{xx} - \varepsilon_{yy}\right)^2 + \left(\varepsilon_{xy} + \varepsilon_{yx}\right)^2} \text{ Principal Component*} \tag{A.38}$$

$$\tan(2\theta) = \frac{\varepsilon_{xy} + \varepsilon_{yx}}{\varepsilon_{yy} - \varepsilon_{xx}} \ \theta \text{ of first half-axis} \tag{A.39}$$

*It can be noted that negative constraint refers to a compression and positive constraint to an expansion.

We performed strain calculations in order to investigate lateral variation of elastic deformations along the Tuzla Fault and its surroundings. GAMIT/GLOBK derived horizontal coordinates (N, E) as well as their slip rates were used for Delaunay triangulation and calculating strain tensors.

A.4. Fault Plane Solution

Instant motion of the Earth's crust during an earthquakes can be expressed by its three angles: (1) Strike and (2) dip angles represent the structure of the plane where the earthquake occurs. They are basically the orientation of the plane in horizontal and vertical axis, respectively. (3) Rake represents the direction of the motions, in other word slip vector. It is the angle between strike and movement of the hanging wall with respect to footwall (Figure A.13).

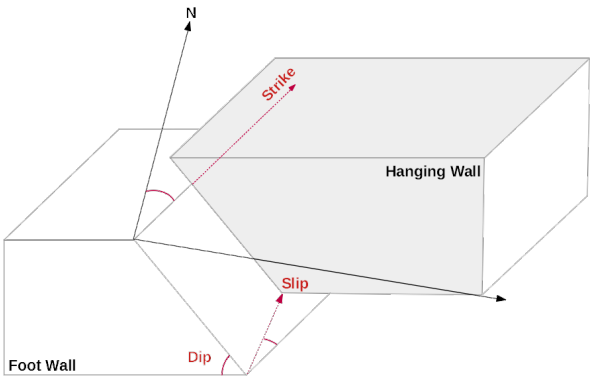

Figure A.13. Demonstration of strike, dip and rake of a fault.

These three angles quantify the motion generated by an earthquake. To generate an earthquake, double force couples are required. Unit focal sphere surrounding an earthquake source have two tension and pressure axes, as a result of double couple forces. Figure A.14 illustrates double force couples, which can be interpreted as dextral or sinistral fault depending on which nodal plane represent the actual fault plane. In this example, it refers to a right lateral strike slip faulting (dextral) if the actual fault plane is the E-W striking nodal plane (Figure A.14). Alternatively, assuming the N-S nodal plane is the actual fault plane, it would be a left lateral strike slip faulting (sinistral). Figure A.16 shows four main fault types namely thrust fault (A), normal Fault (B), sinistral fault (C) and dextral fault (D).

Fault plane solution is performed by analyzing the radiation patterns. First motions of P wave onsets are used to quantify radiation pattern, whether it is + or -,

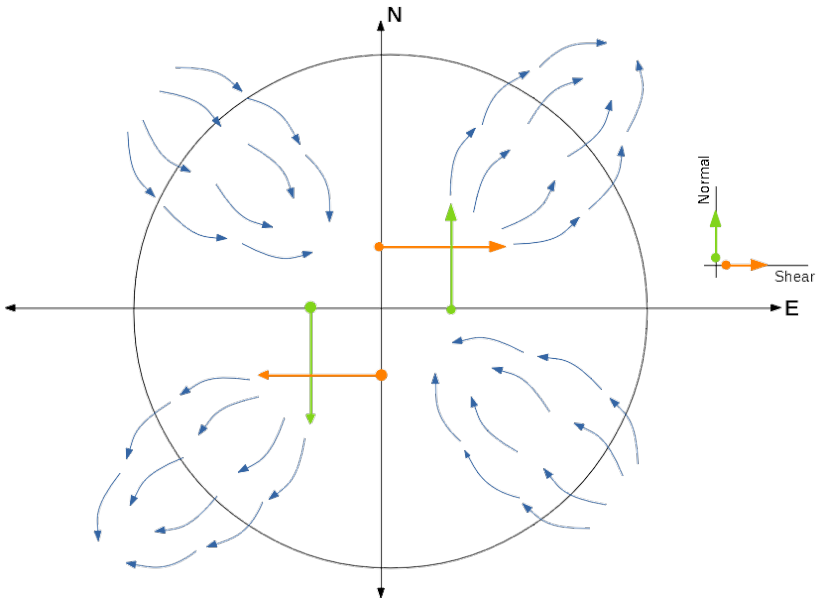

Figure A.14. Double Force Couple.

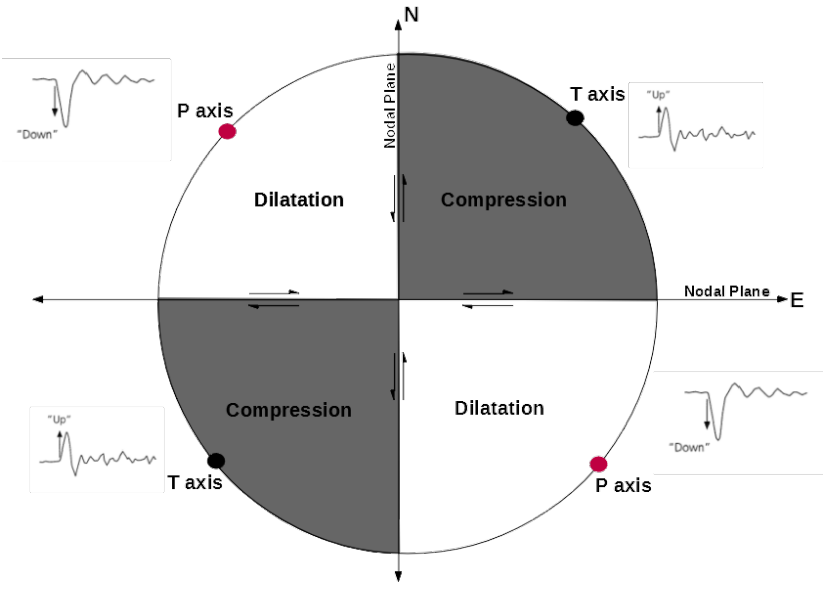

Figure A.15. Demonstration of dilatation and compression in fault plane. While downward first motion of the P wave corresponds dilatation, upward firs motion of the P wave indicates compression.

in other words, upward or downward, which corresponds compression and dilatation at unit focal sphere (Figure A.15). While the polarity of P wave resulted movement to the station is called compression, its motion away from the station corresponds dilatation. Although, upward and downward directions of radiation patterns give the information of compression and dilatation quadrants, they do not provide which nodal plane is the actual fault plane / auxiliary plane. therefore, geodetic and geological studies are crucial to verify which nodal plane represents actual fault plane [41].

In this study, we analyzed focal mechanisms of the M 3.5+ earthquakes in the vicinity of the Tuzla Fault for the time period 2003-2019. Seismic data were taken from Boğaziçi University Kandilli Observatory and Earthquake Research Institute Regional Earthquake-Tsunami Monitoring Center (KOERI-RETMC) [53]. Radiation patterns of seismic waves were analyzed manually using SeisGram2K v7.0.0. software. After refining locations of all earthquakes using HYPOCENTER, FOCMEC software was used to obtain focal mechanisms in the target area.

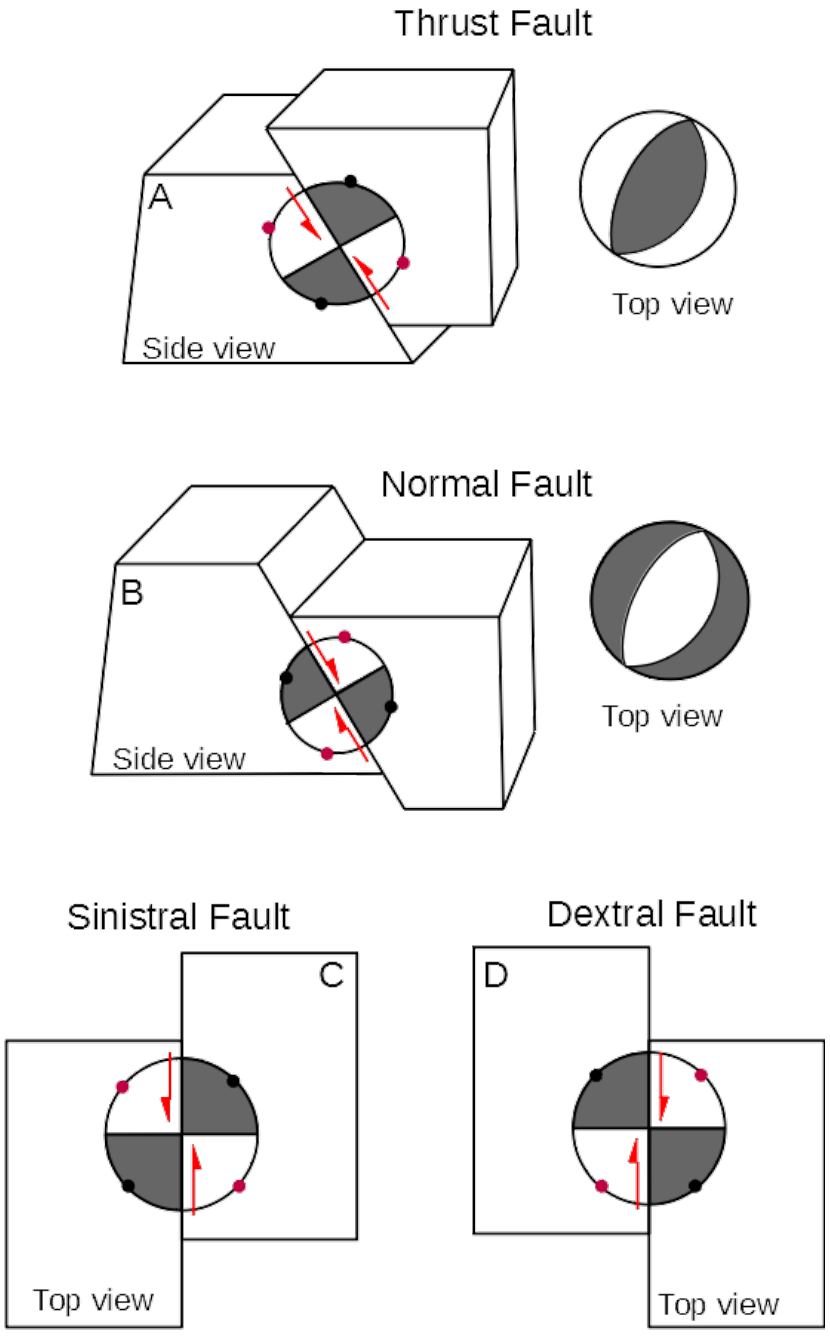

Figure A.16. Different types of fault structure. Red arrows indicate the direction of the fault plane. Pink and black dots on the beach balls represent P axis and T axis, respectively. A, B, C and D indicate thrust fault, normal fault, sinistral fault and dextral fault, respectivley

APPENDIX B: EARTHQUAKE LOCATIONS/STATION PLOTS WITH ERROR ELLIPSES OBTAINED FROM HYPOCENTER

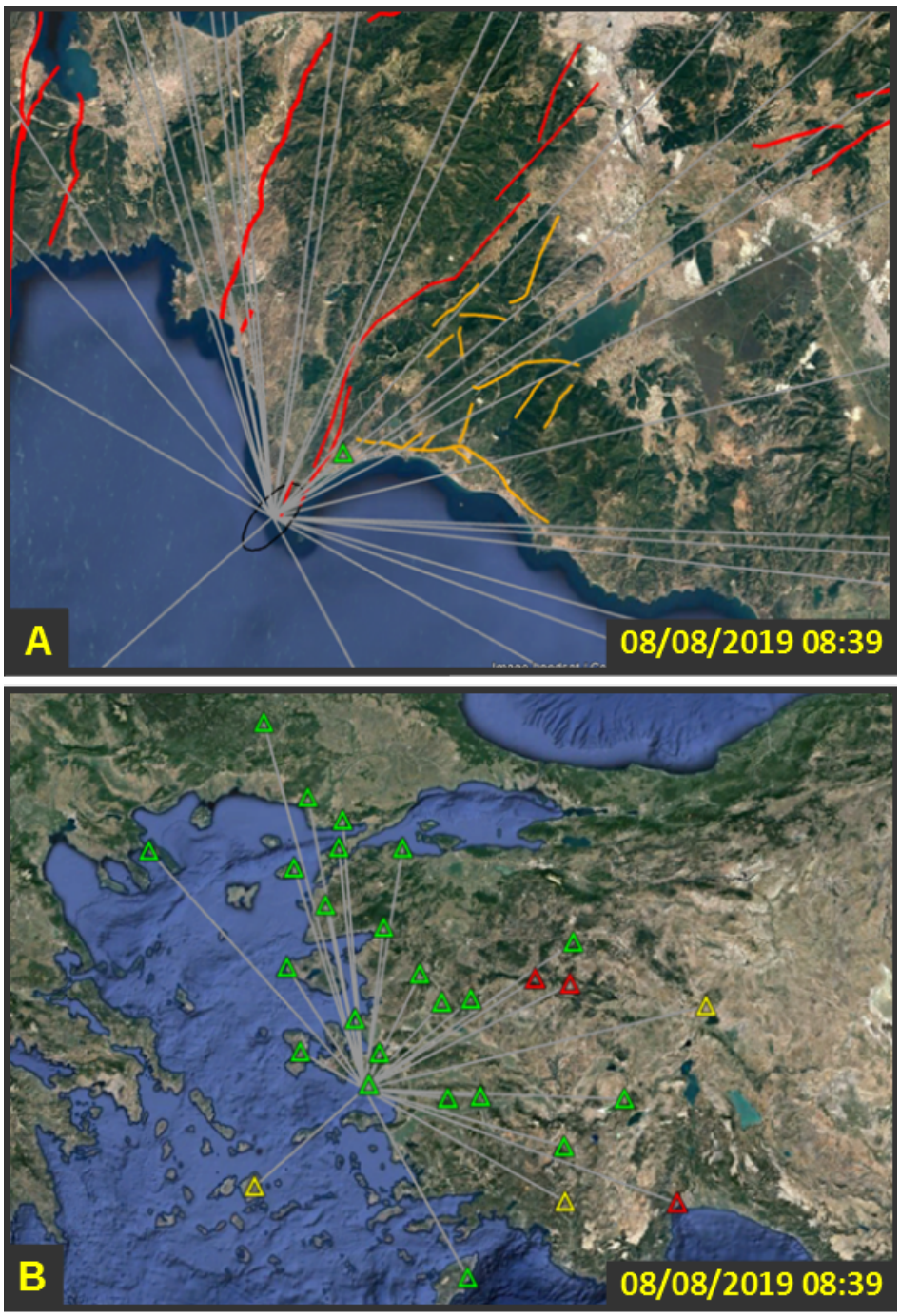

Figure B.1. 08/08/2019 08:39 M 5.0 Earthquake. A indicates location and location error ellipse of earthquake. B indicates location/station plot.

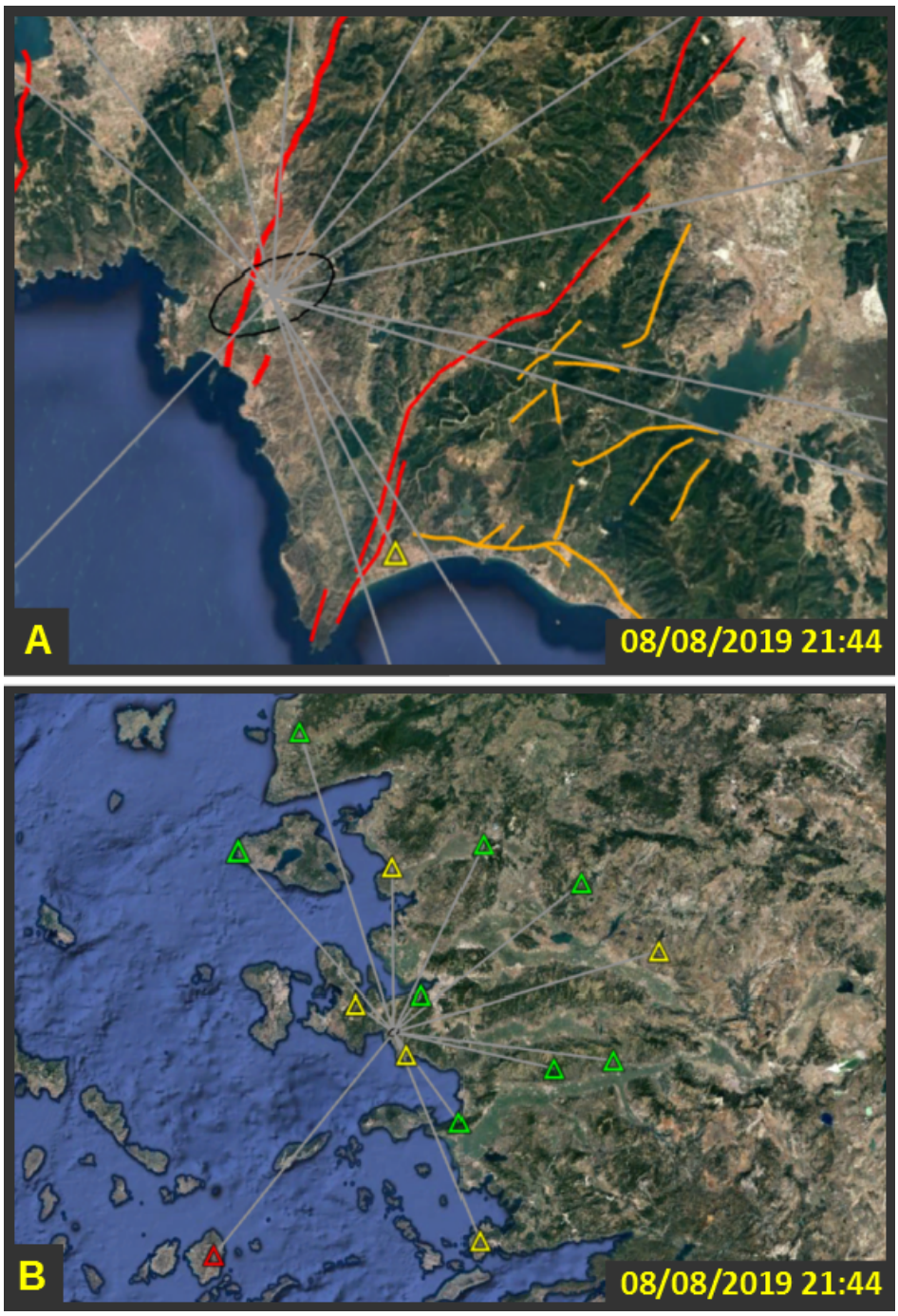

Figure B.2. 08/08/2019 21:44 M 3.6 Earthquake. A indicates location and location error ellipse of earthquake. B indicates location/station plot.

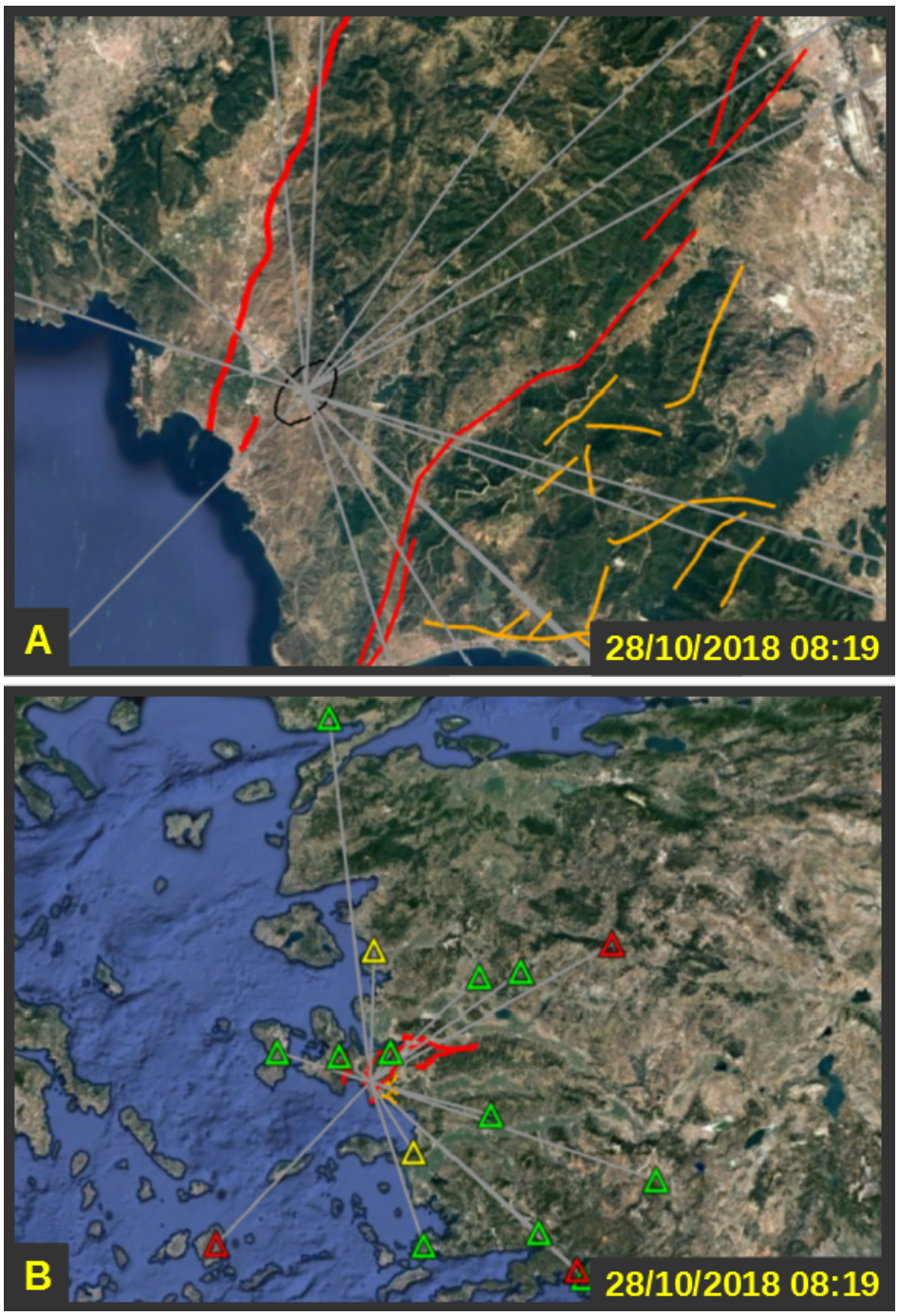

Figure B.3. 28/10/2018 08:19 M 3.5 Earthquake. A indicates location and location error ellipse of earthquake. B indicates location/station plot.

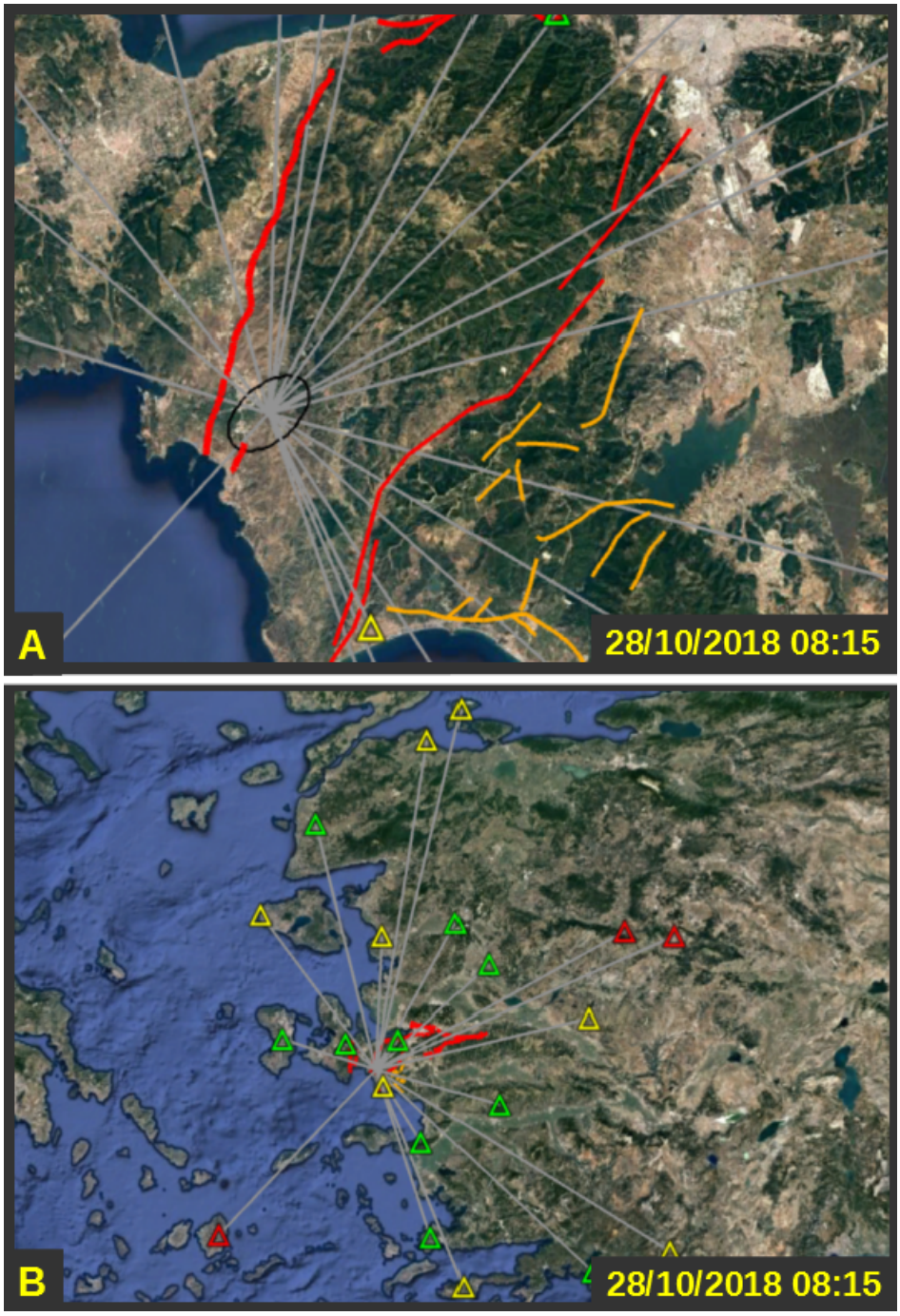

Figure B.4. 28/10/2018 08:15 M 4.0 Earthquake. A indicates location and location error ellipse of earthquake. B indicates location/station plot.

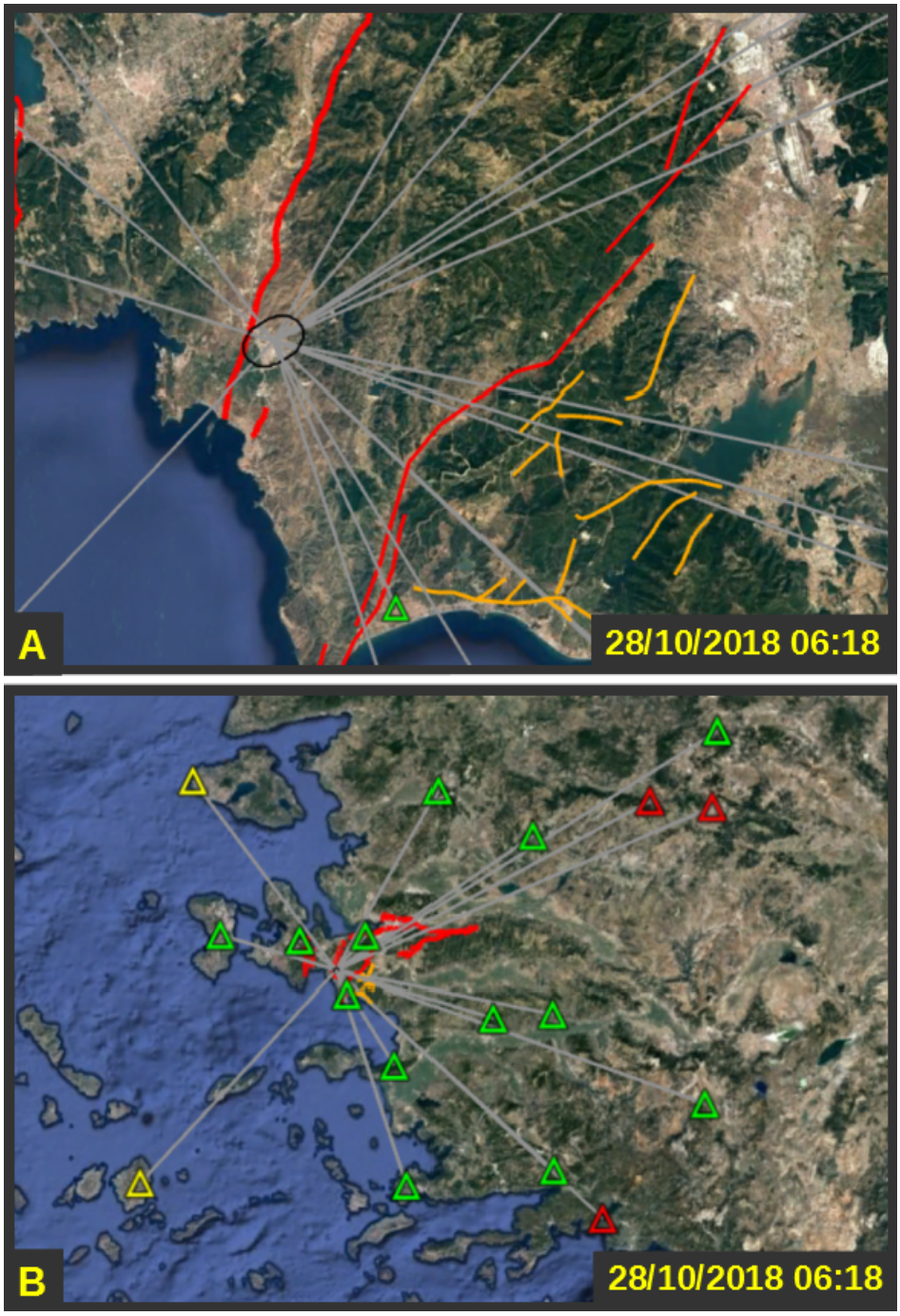

Figure B.5. 28/10/2018 06:18 M 3.8 Earthquake. A indicates location and location error ellipse of earthquake. B indicates location/station plot.

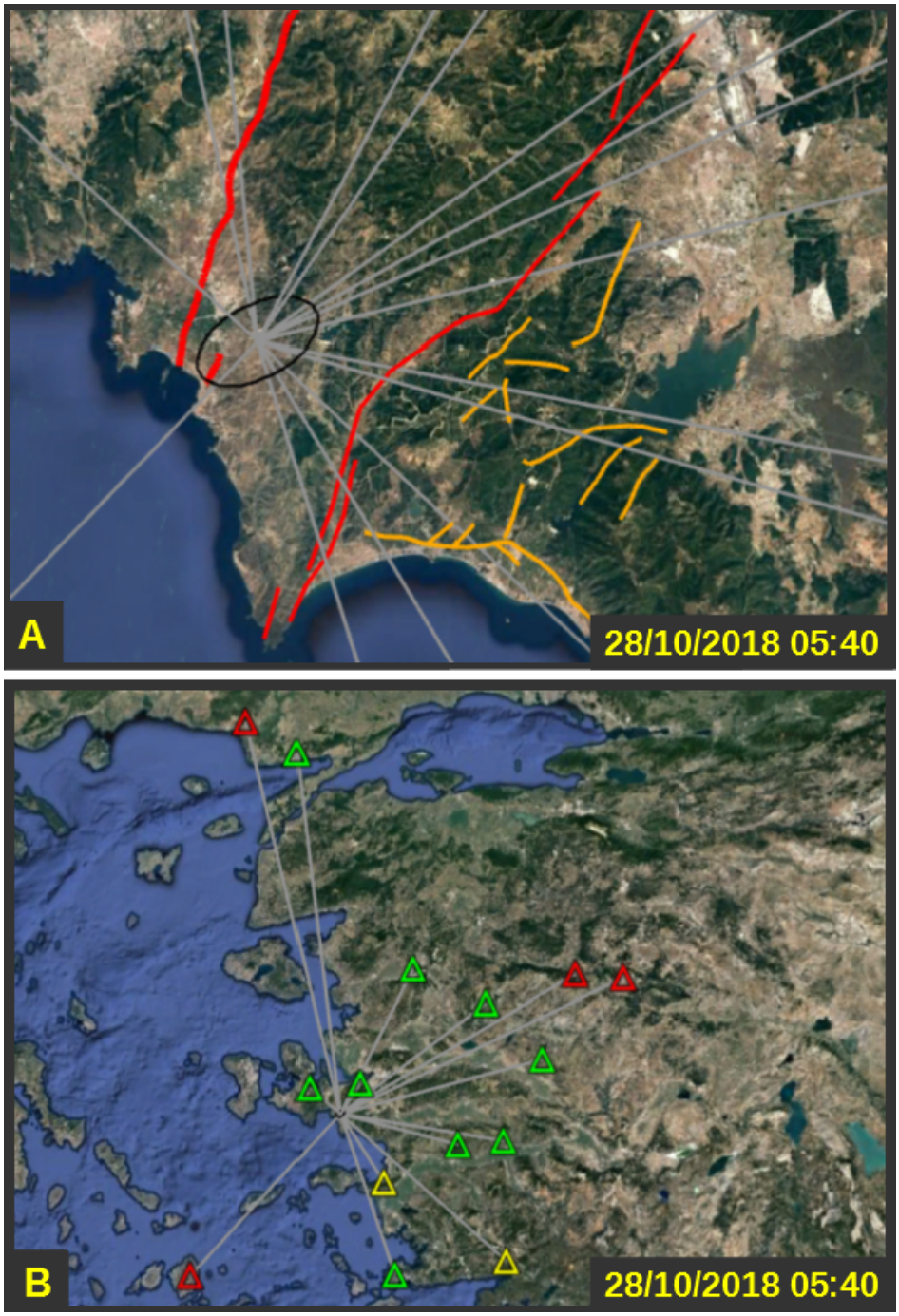

Figure B.6. 28/10/2018 05:40 M 3.5 Earthquake. A indicates location and location error ellipse of earthquake. B indicates location/station plot.

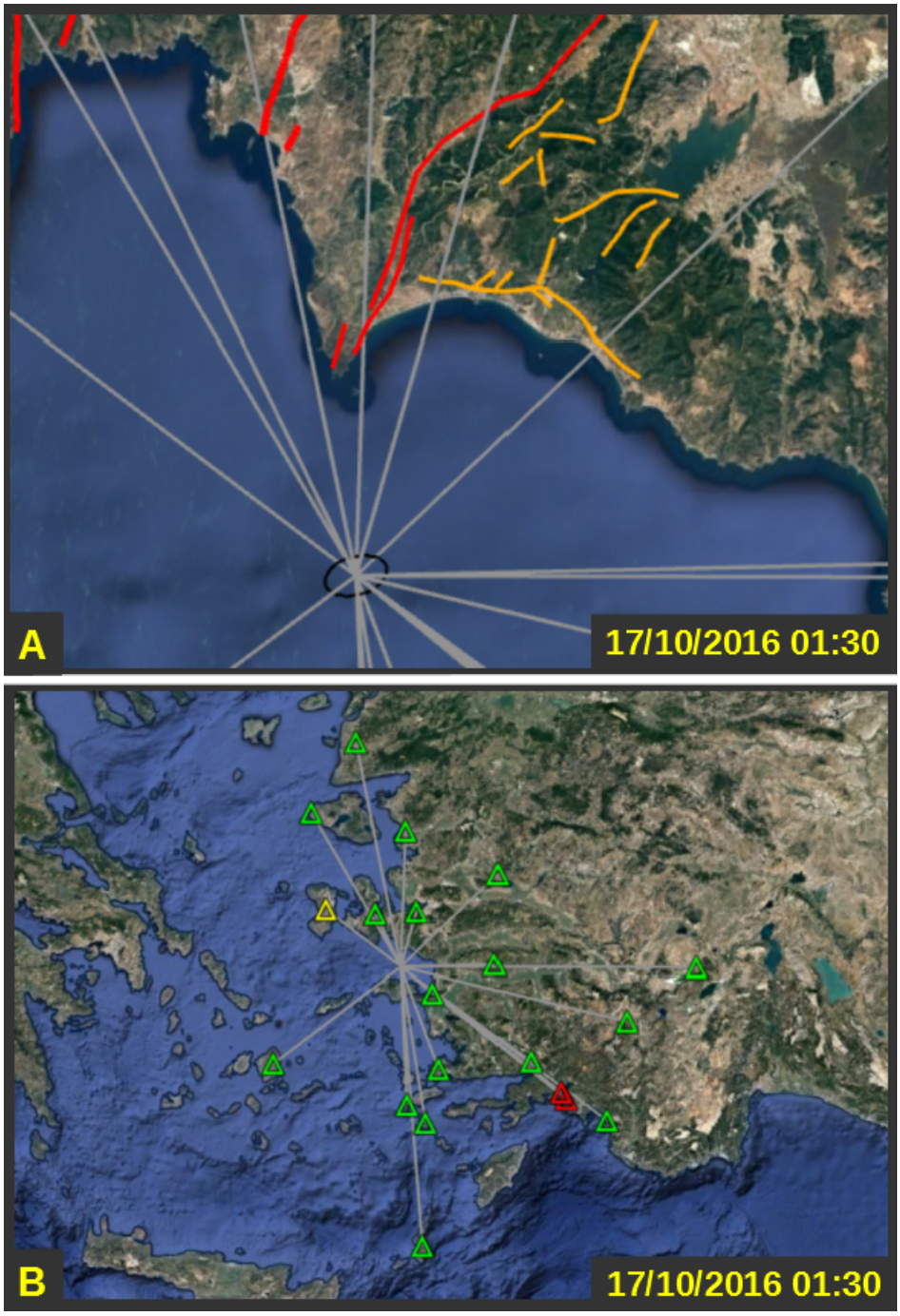

Figure B.7. 17/10/2016 01:30 M 4.7 Earthquake. A indicates location and location error ellipse of earthquake. B indicates location/station plot.

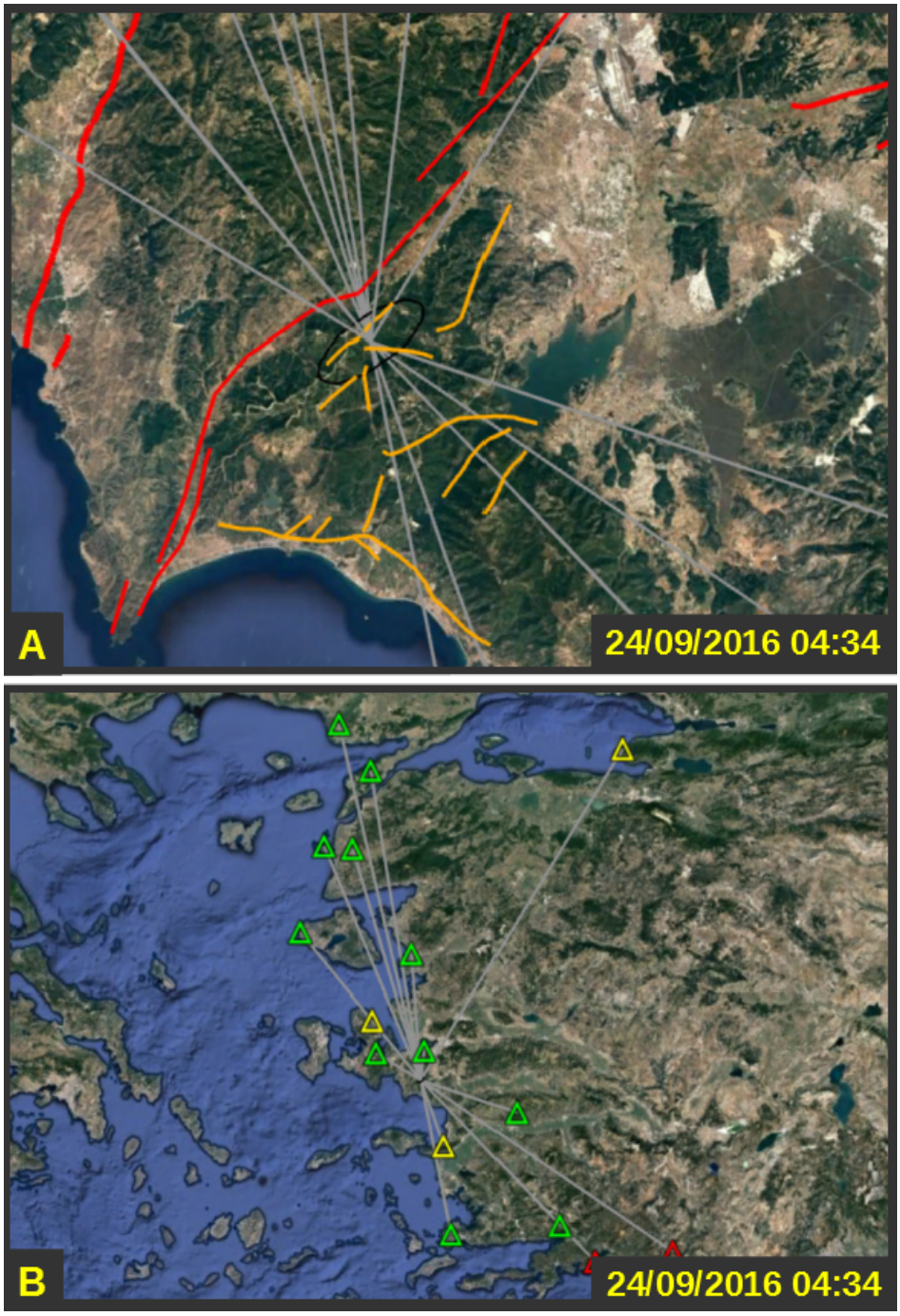

Figure B.8. 24/09/2016 04:34 M 3.6 Earthquake. A indicates location and location error ellipse of earthquake. B indicates location/station plot.

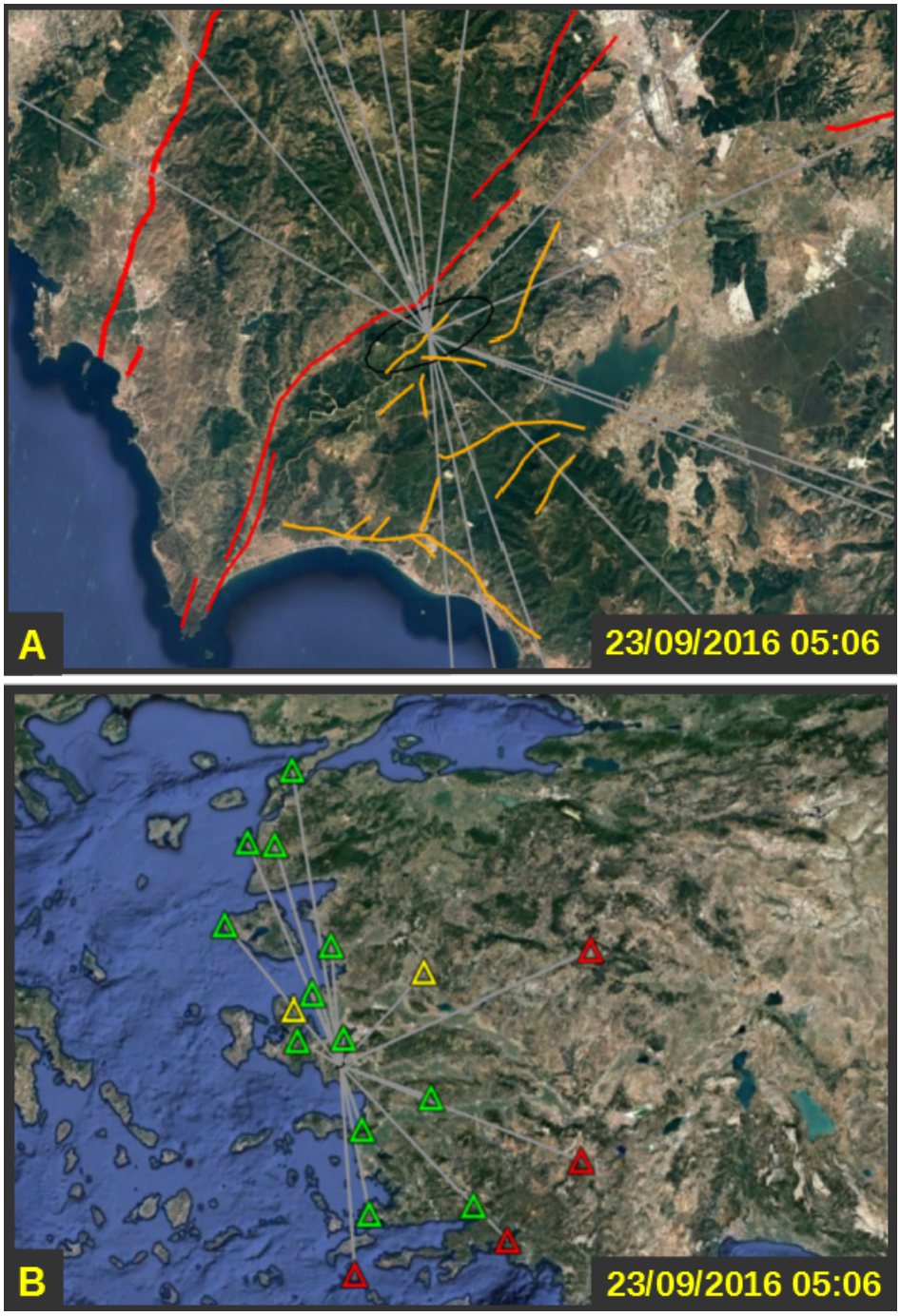

Figure B.9. 23/09/2016 05:06 M 3.9 Earthquake. A indicates location and location error ellipse of earthquake. B indicates location/station plot.

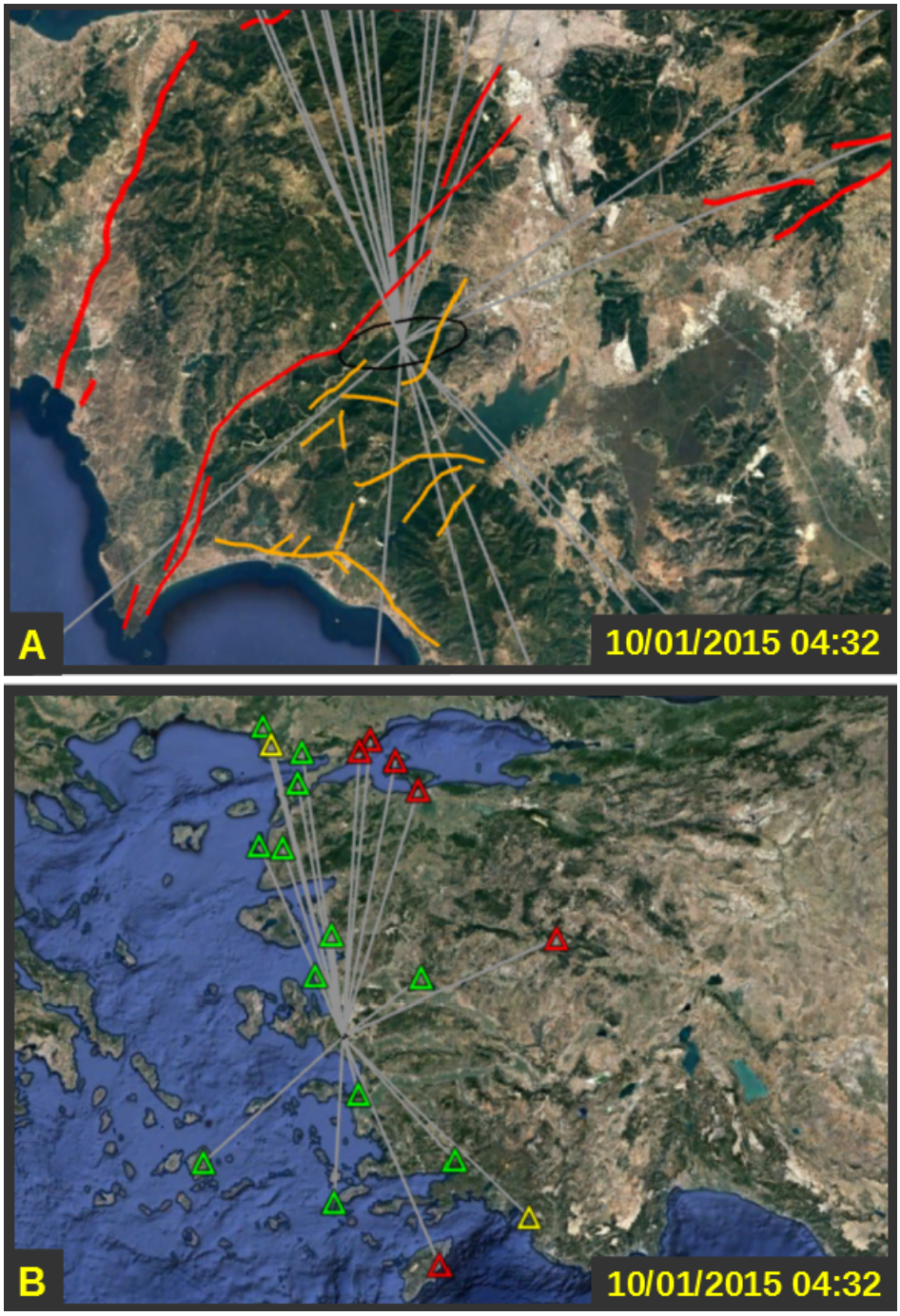

Figure B.10. 10/01/2015 04:32 M 4.3 Earthquake. A indicates location and location error ellipse of earthquake. B indicates location/station plot.

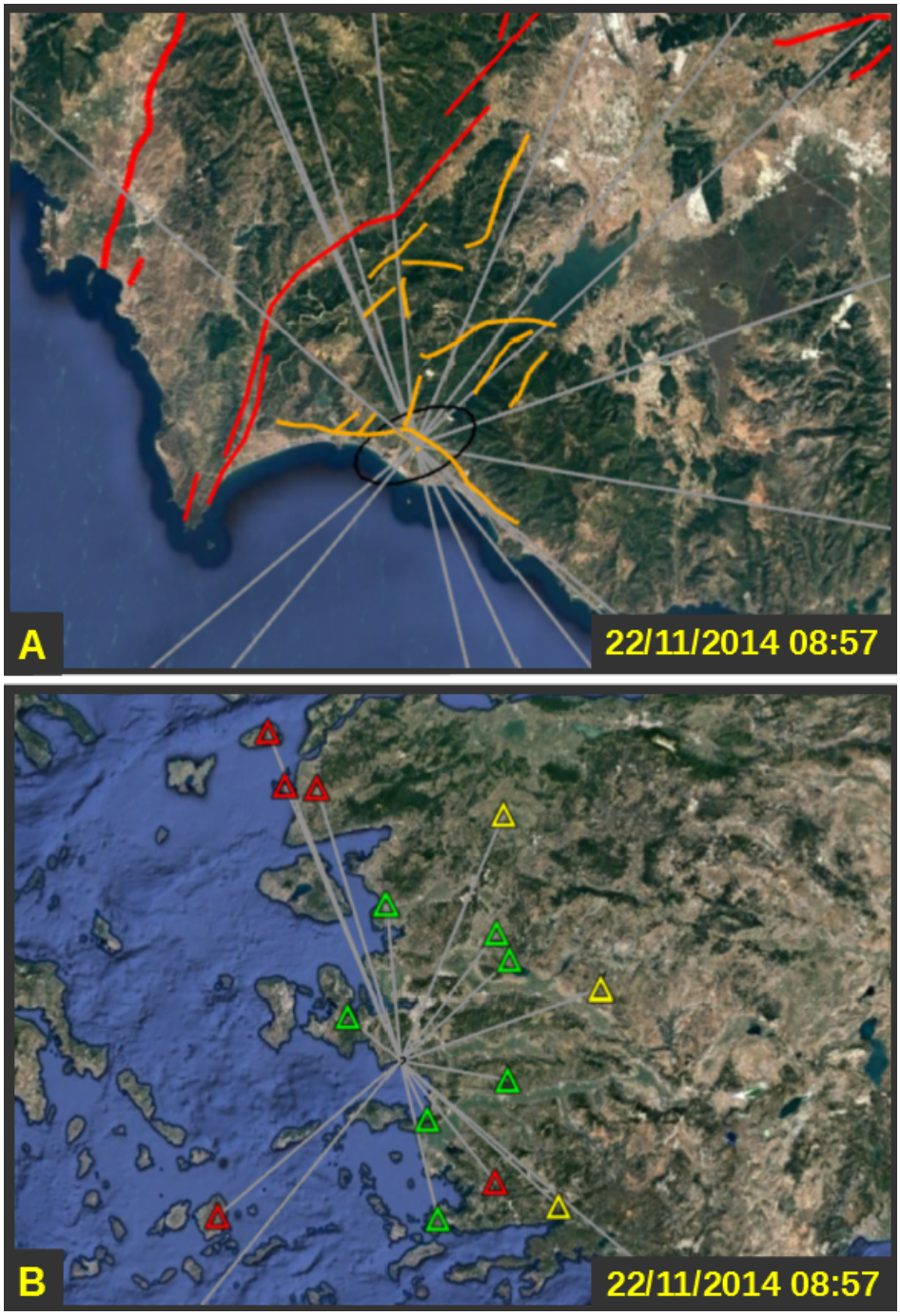

Figure B.11. 22/11/2014 08:57 M 3.7 Earthquake. A indicates location and location error ellipse of earthquake. B indicates location/station plot.

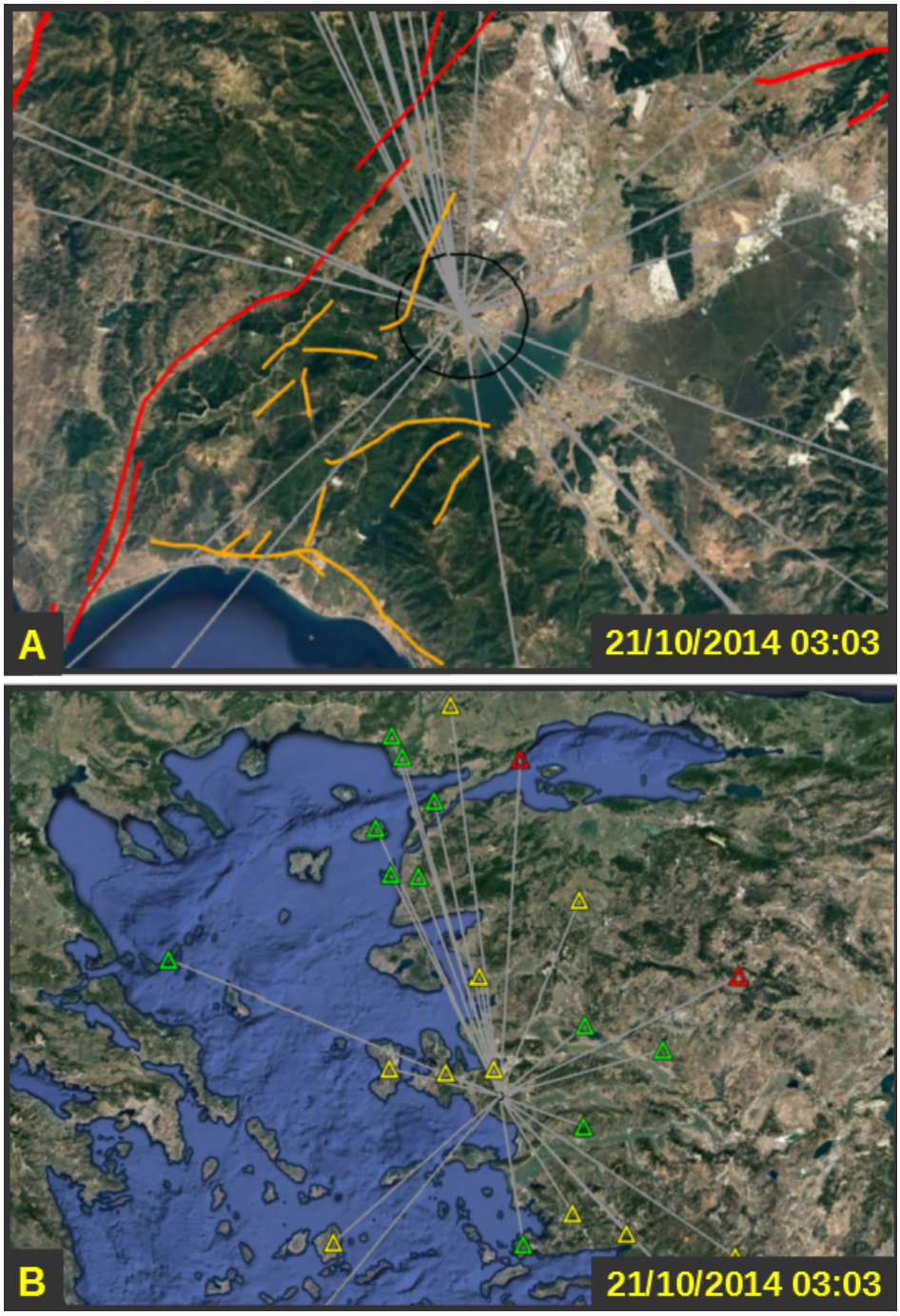

Figure B.12. 21/10/2014 03:03 M 4.1 Earthquake. A indicates location and location error ellipse of earthquake. B indicates location/station plot.

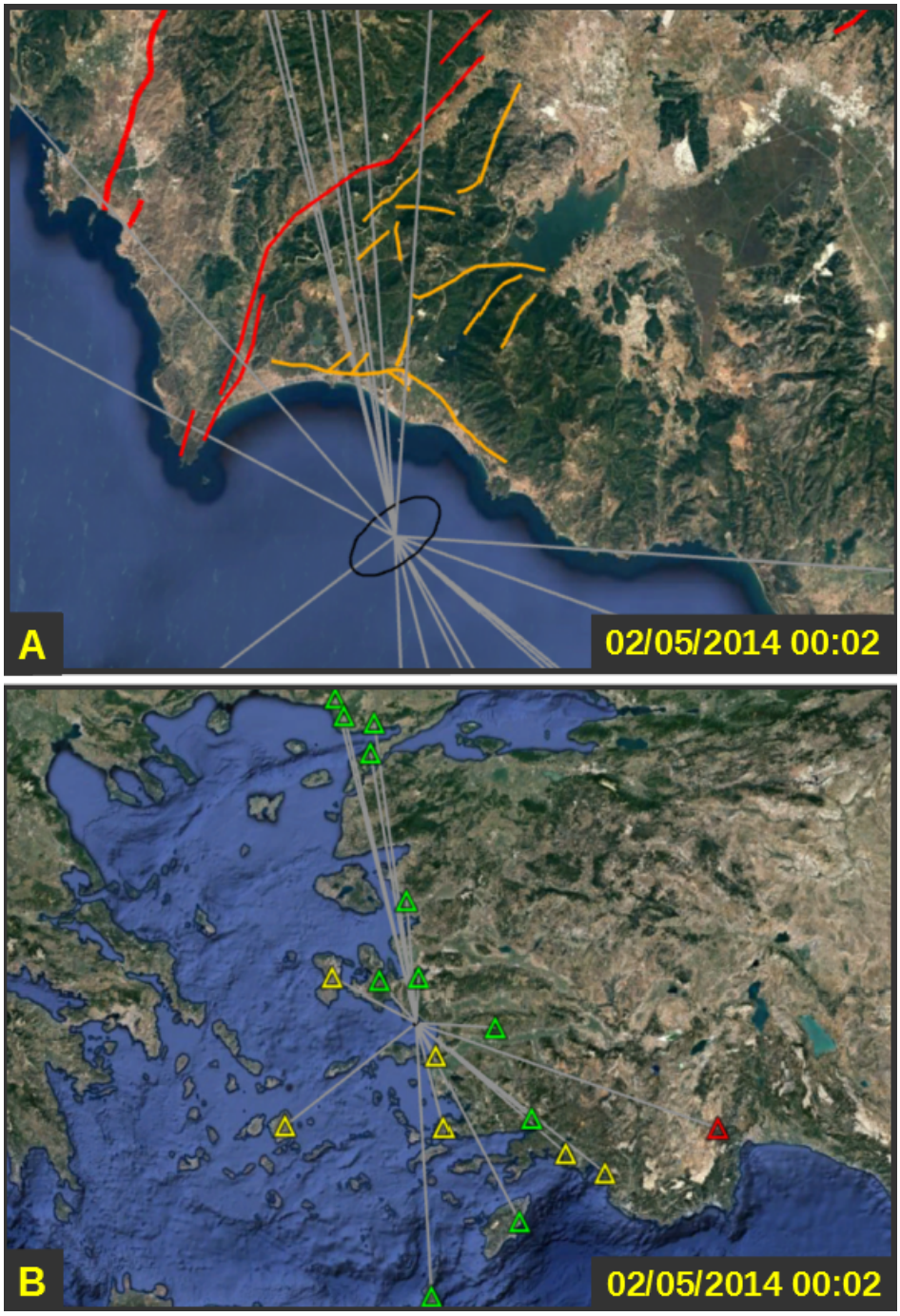

Figure B.13. 02/05/2014 00:02 M 3.7 Earthquake. A indicates location and location error ellipse of earthquake. B indicates location/station plot.

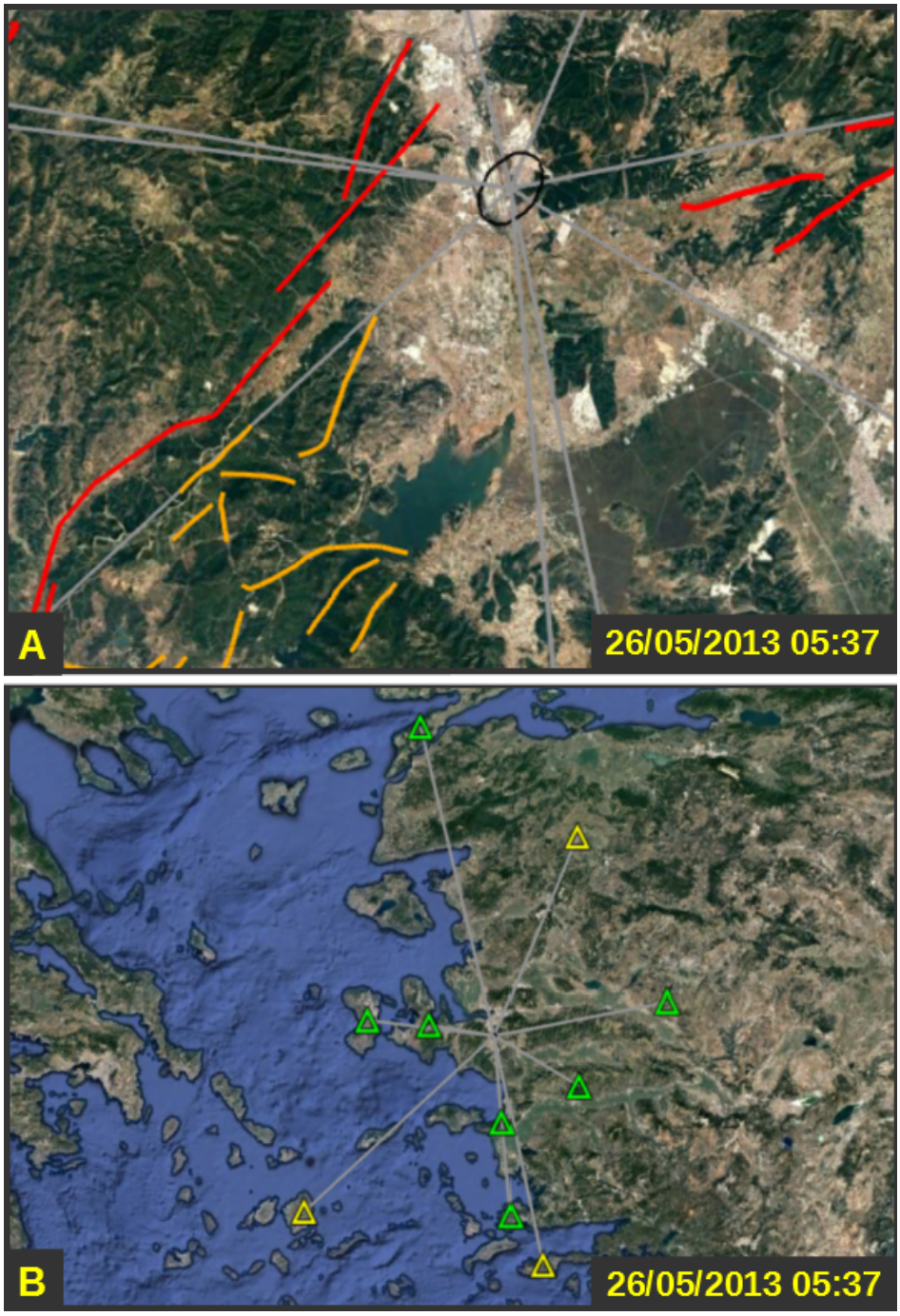

Figure B.14. 26/05/2013 05:37 M 3.5 Earthquake. A indicates location and location error ellipse of earthquake. B indicates location/station plot.

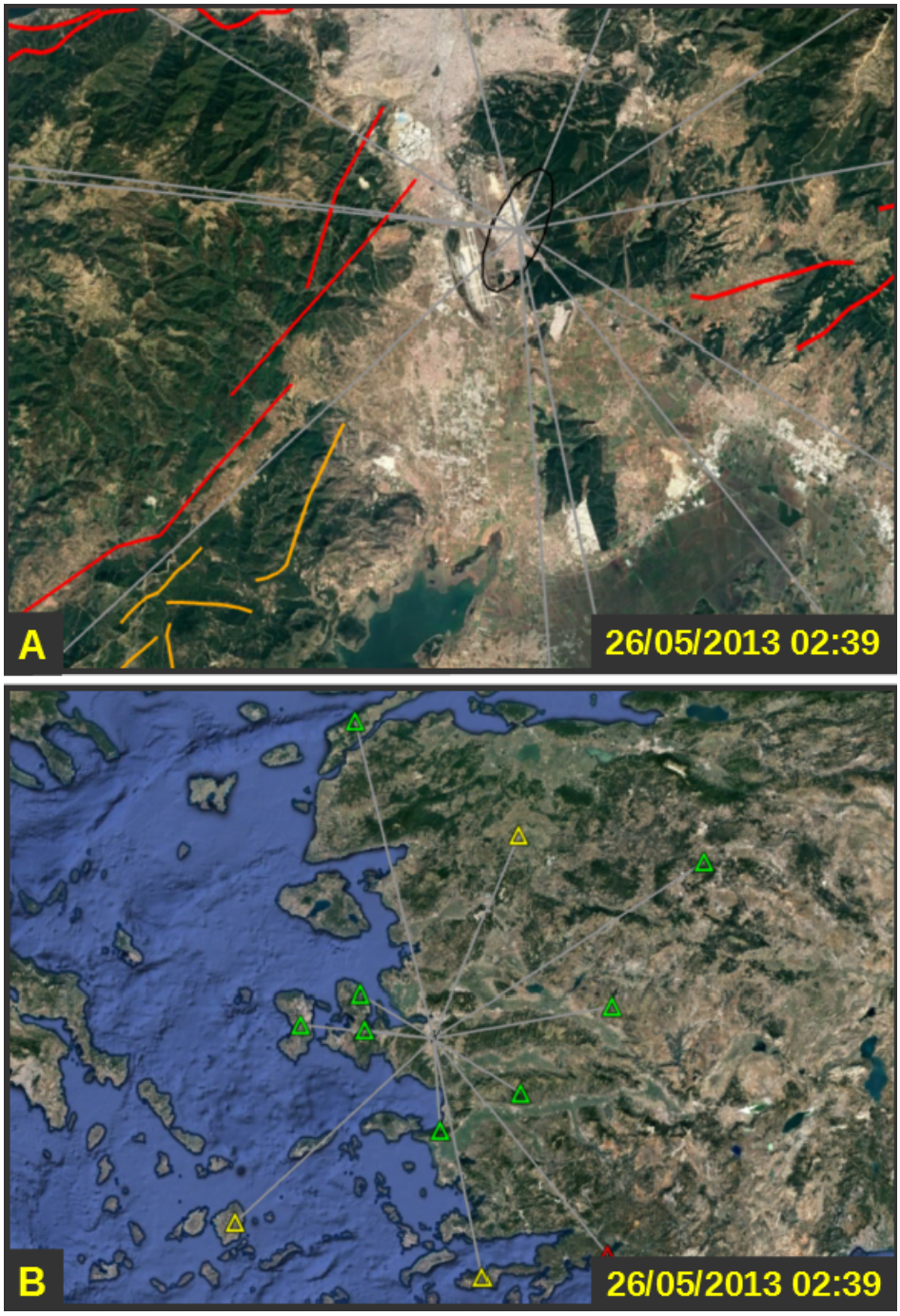

Figure B.15. 26/05/2013 02:39 M 3.6 Earthquake. A indicates location and location error ellipse of earthquake. B indicates location/station plot.

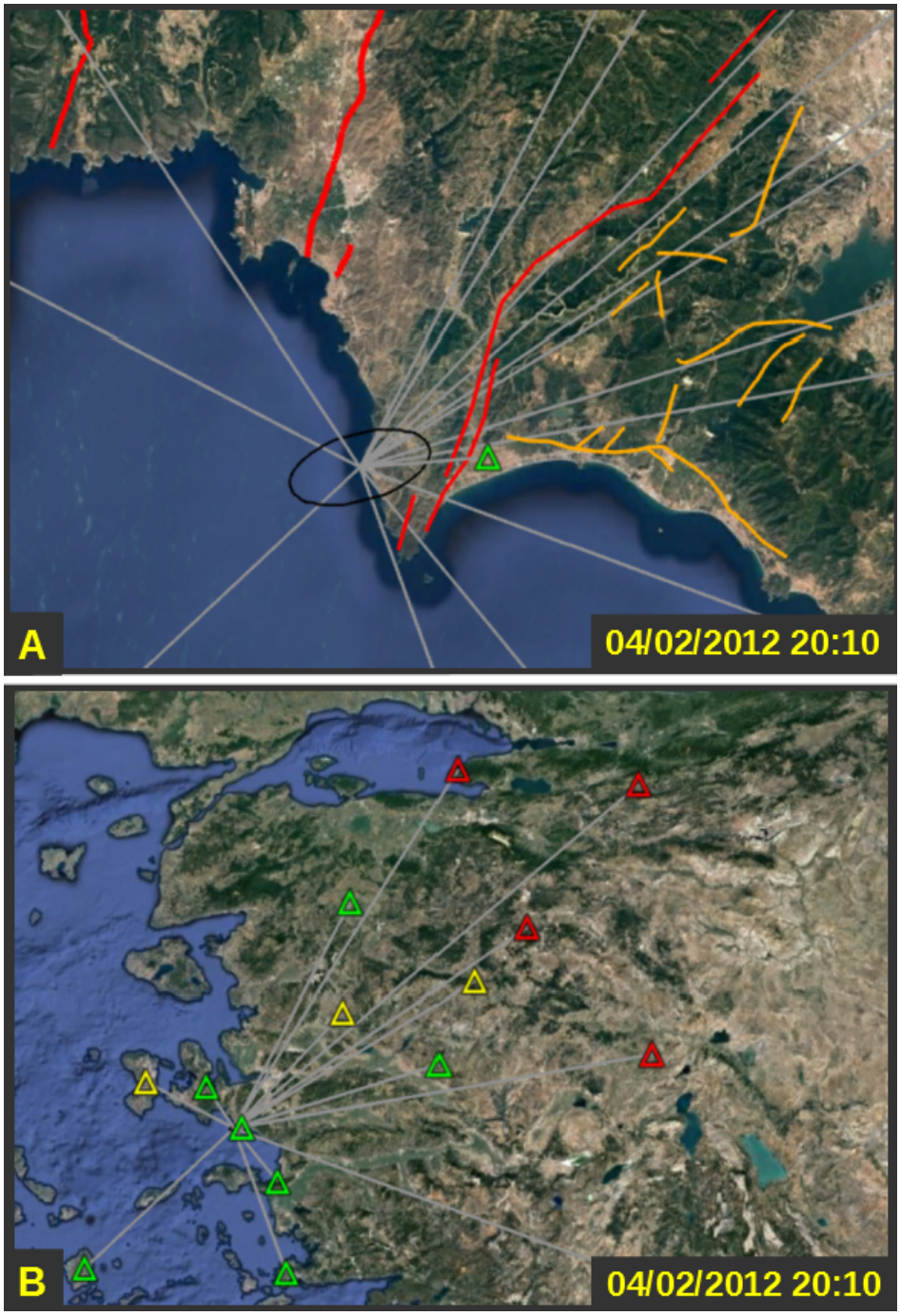

Figure B.16. 04/02/2012 20:10 M 3.8 Earthquake. A indicates location and location error ellipse of earthquake. B indicates location/station plot.

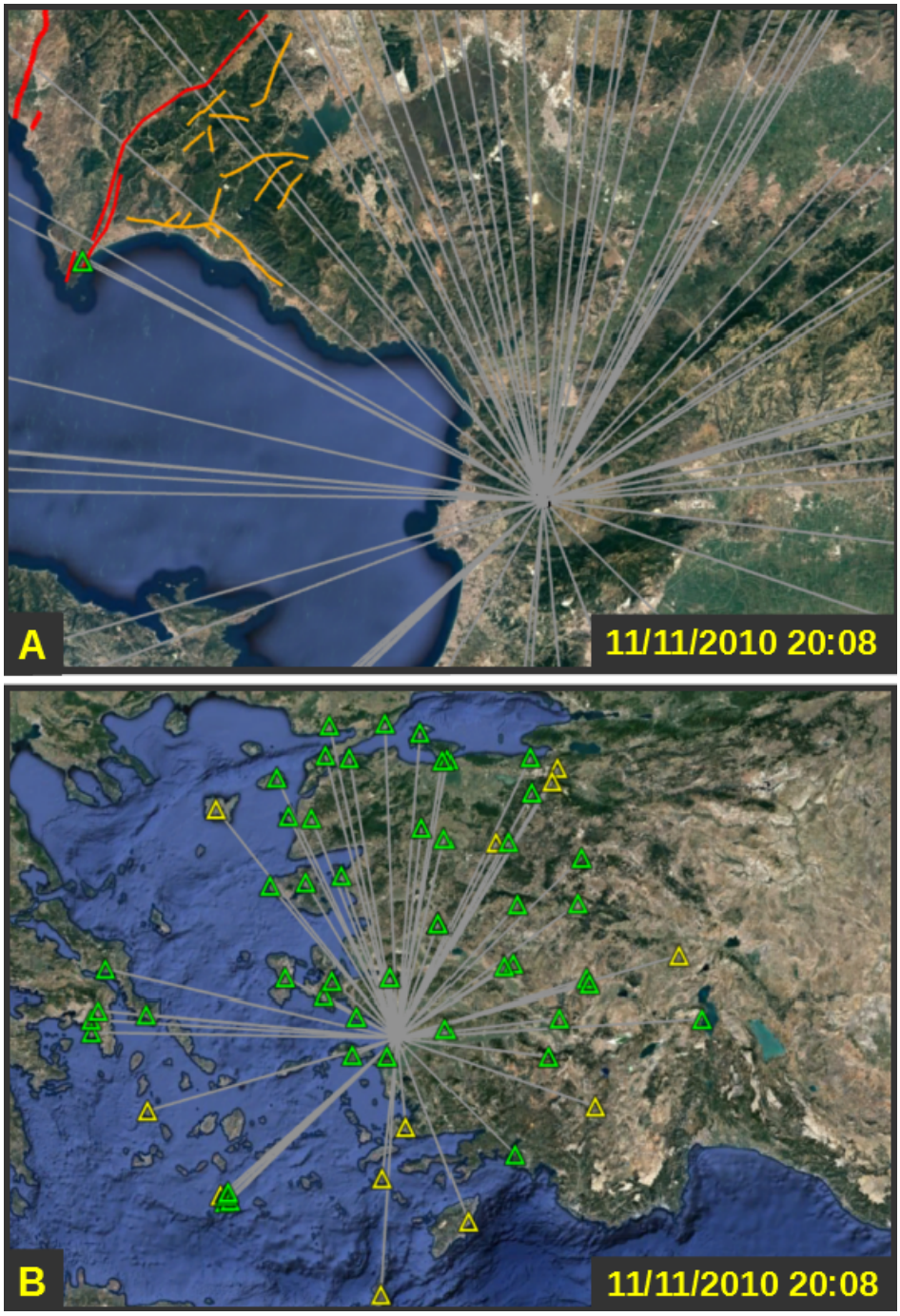

Figure B.17. 11/11/2010 20:08 M 4.7 Earthquake. A indicates location and location error ellipse of earthquake. B indicates location/station plot.

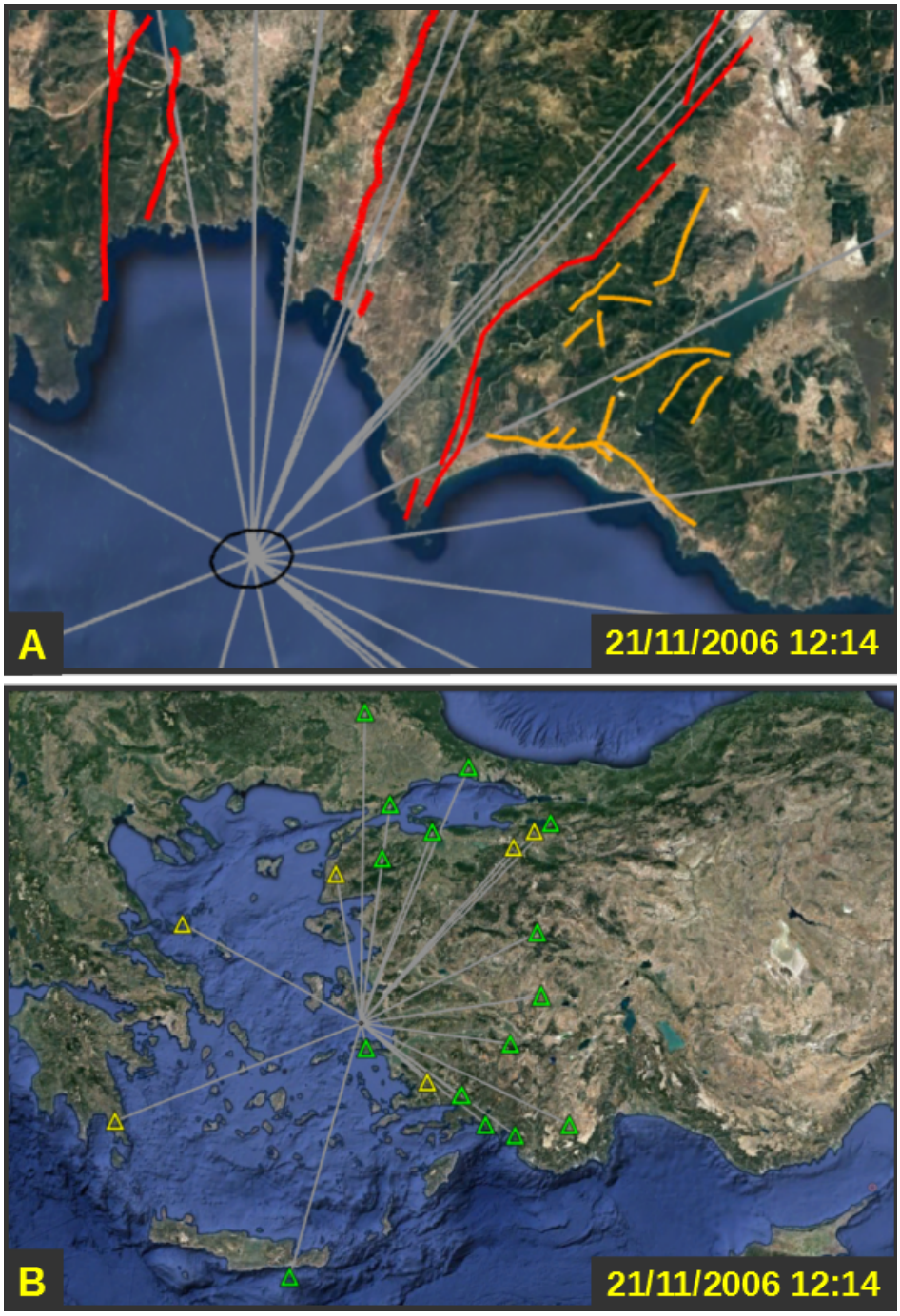

Figure B.18. 21/11/2006 12:14 M 3.5 Earthquake. A indicates location and location error ellipse of earthquake. B indicates location/station plot.

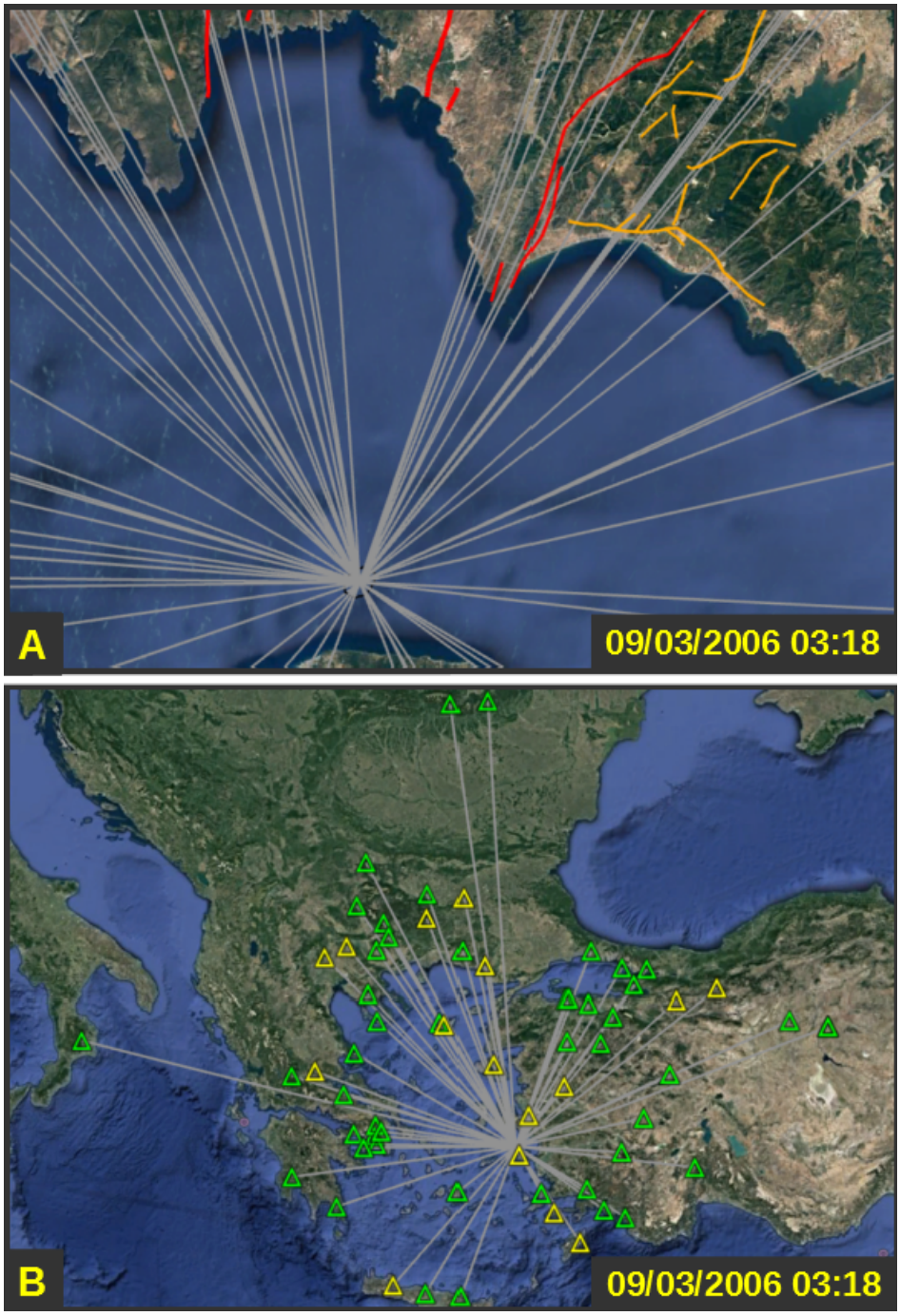

Figure B.19. 09/03/2006 03:18 M 4.3 Earthquake. A indicates location and location error ellipse of earthquake. B indicates location/station plot.

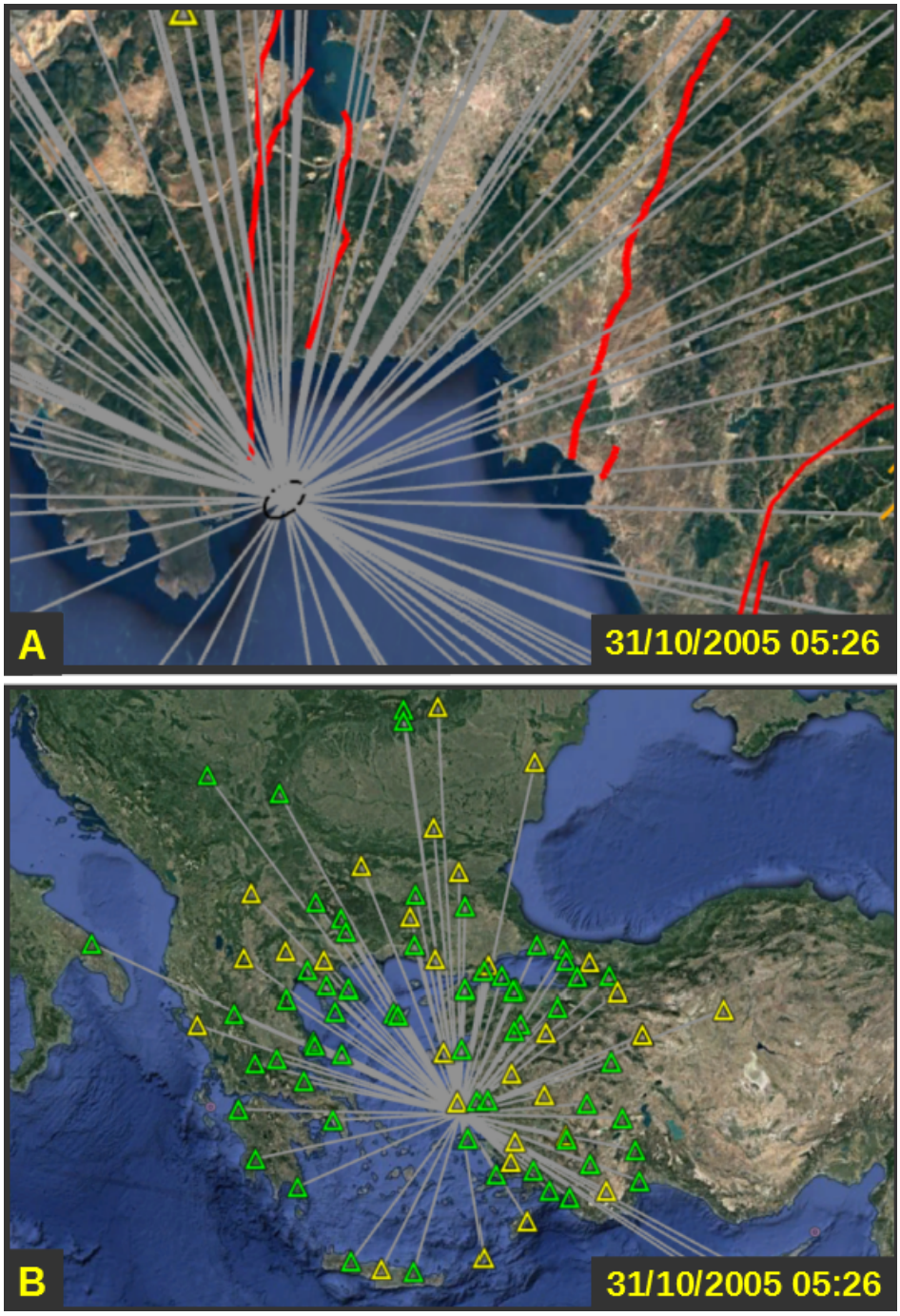

Figure B.20. 31/10/2005 05:26 M 4.8 Earthquake. A indicates location and location error ellipse of earthquake. B indicates location/station plot.

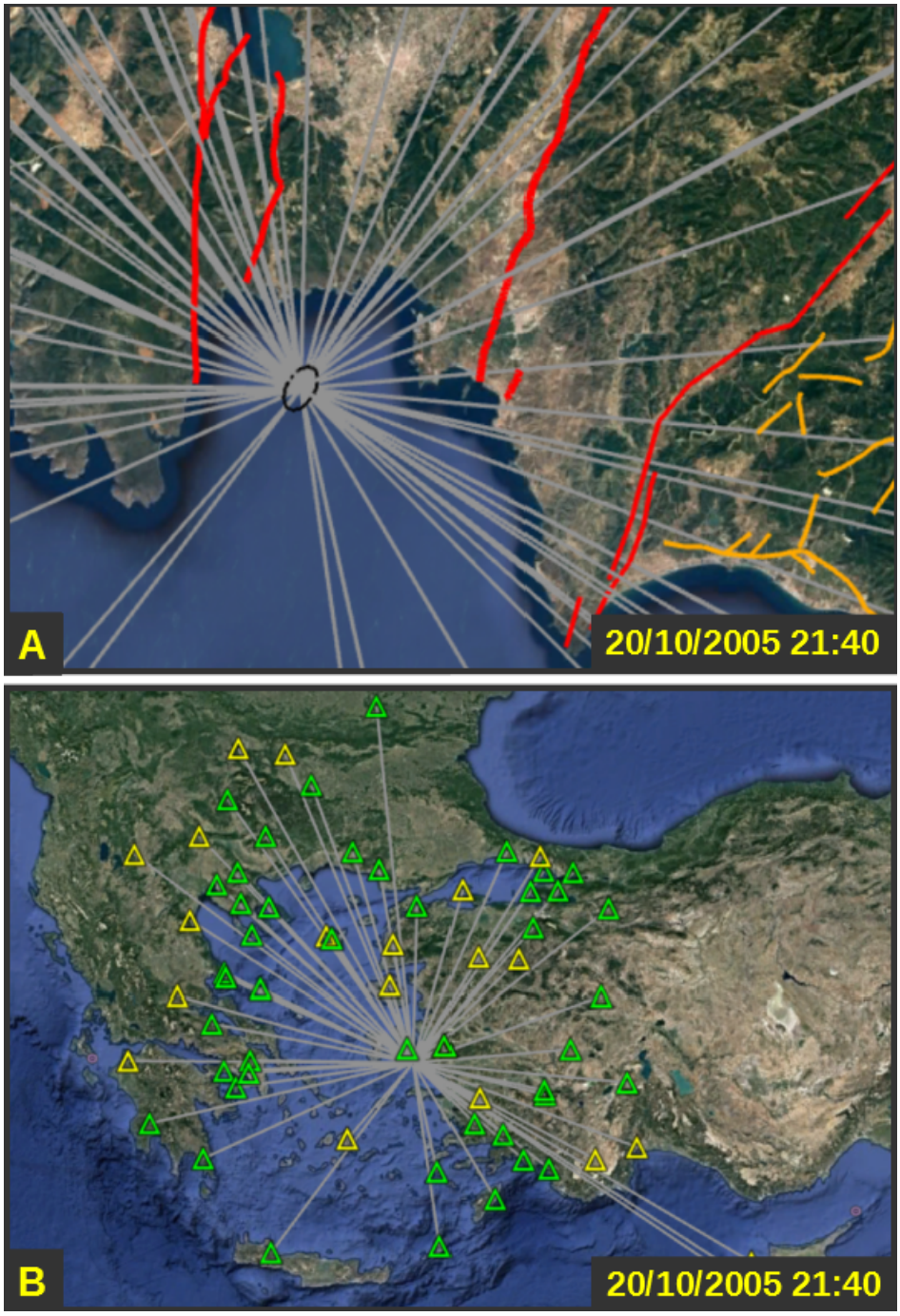

Figure B.21. 20/10/2005 21:40 M 5.9 Earthquake. A indicates location and location error ellipse of earthquake. B indicates location/station plot.

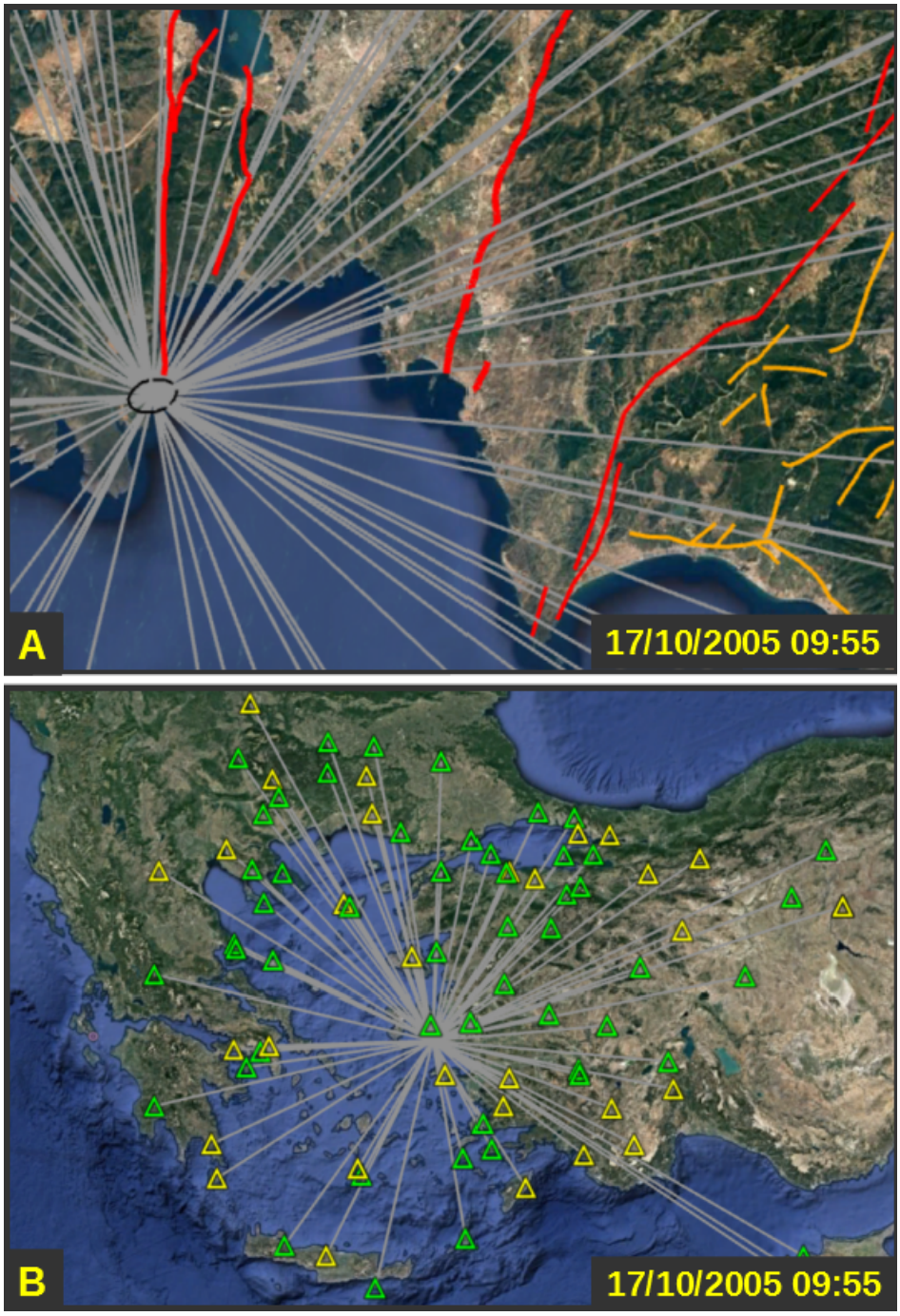

Figure B.22. 17/10/2005 09:55 M 5.3 Earthquake. A indicates location and location error ellipse of earthquake. B indicates location/station plot.

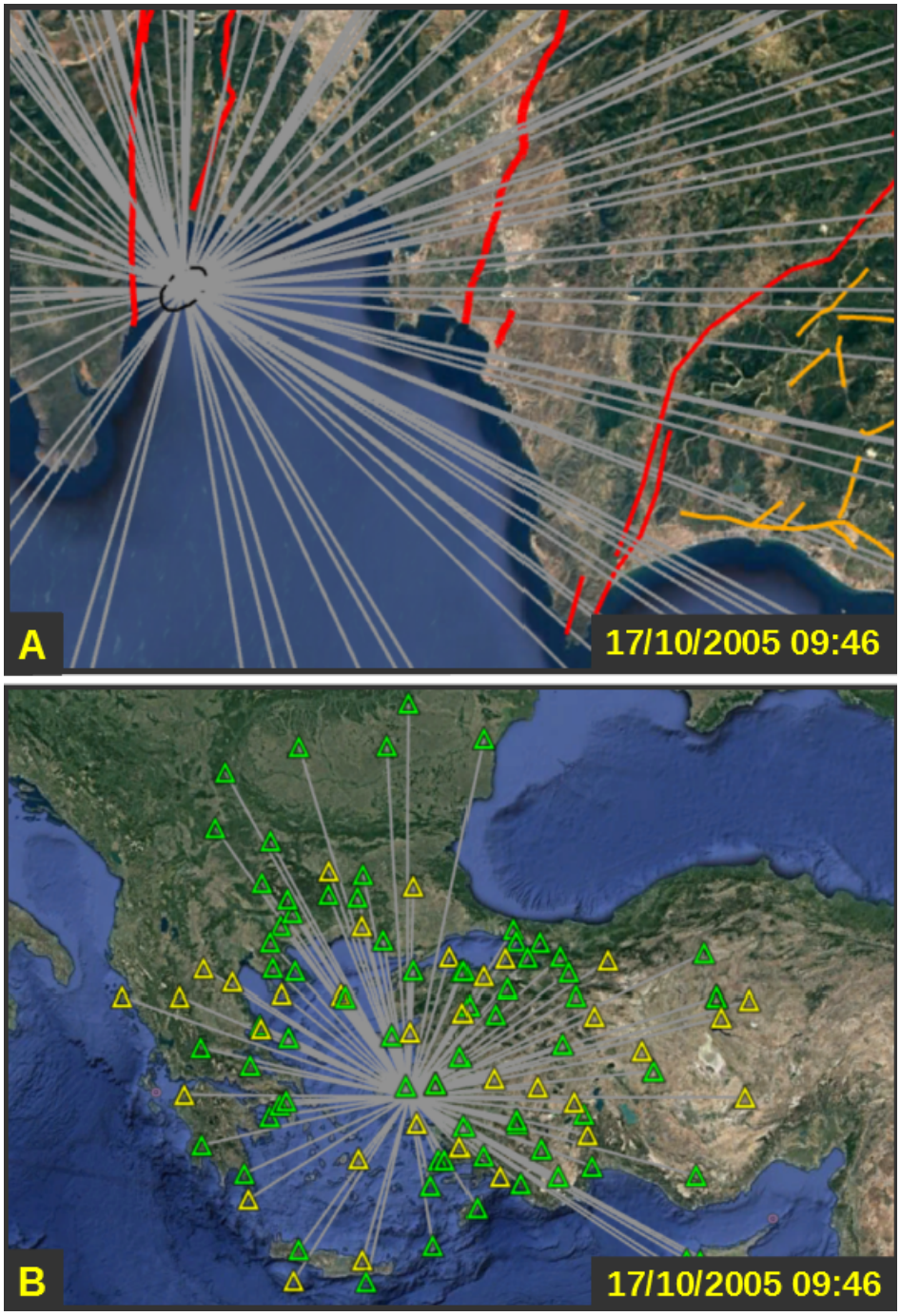

Figure B.23. 17/10/2005 09:46 M 5.8 Earthquake. A indicates location and location error ellipse of earthquake. B indicates location/station plot.

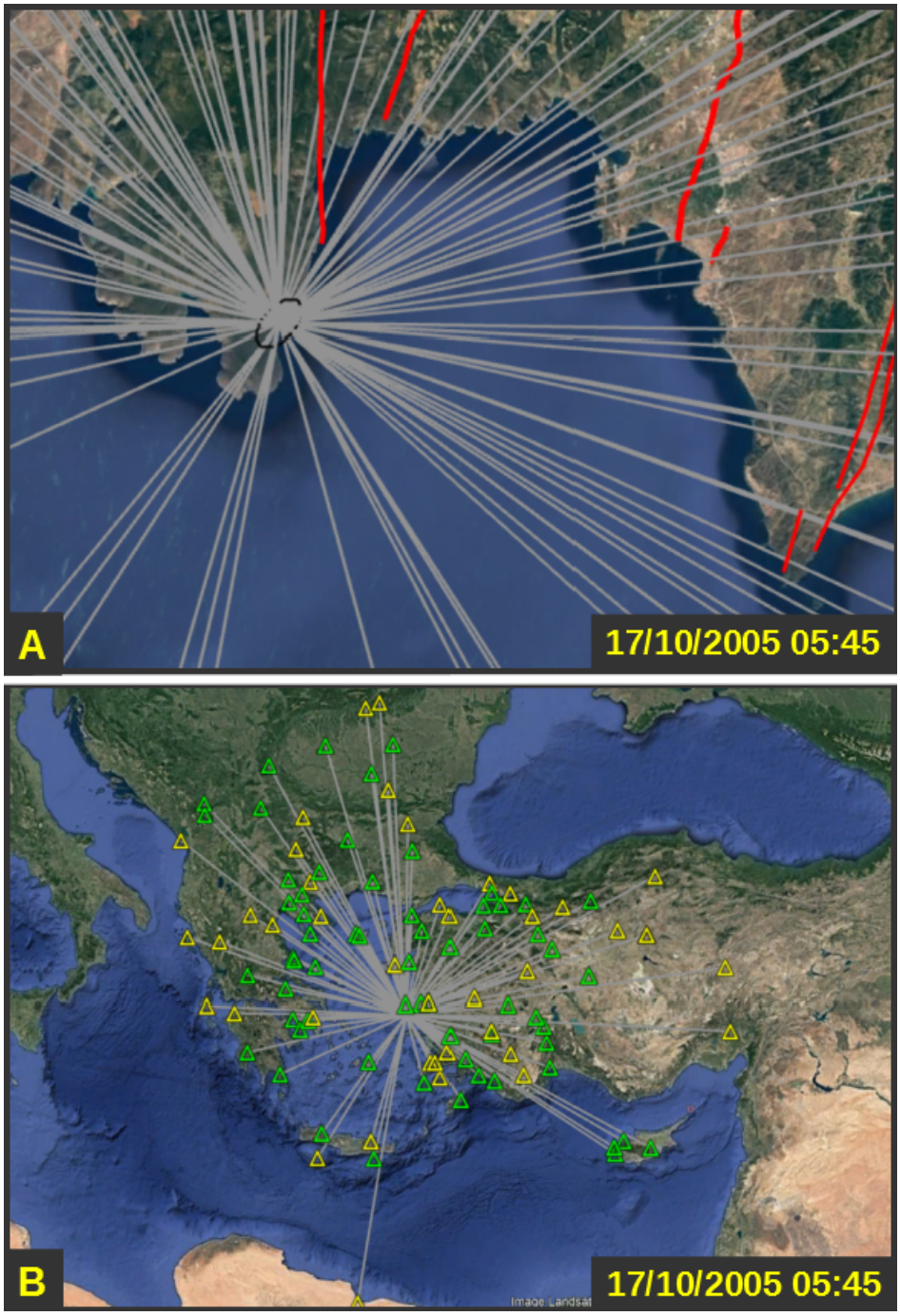

Figure B.24. 17/10/2005 05:45 M 5.7 Earthquake. A indicates location and location error ellipse of earthquake. B indicates location/station plot.

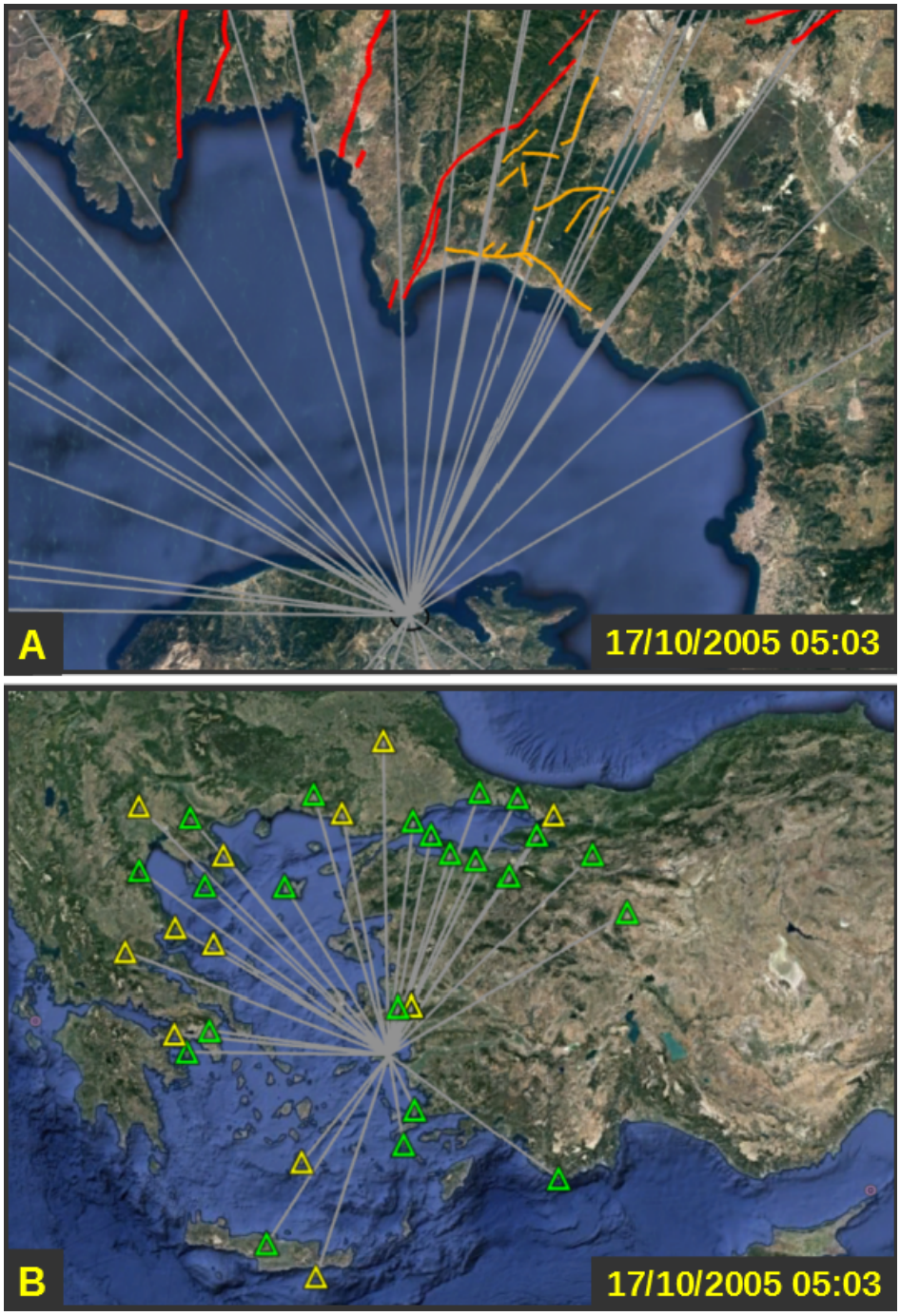

Figure B.25. 17/10/2005 05:03 M 4.3 Earthquake. A indicates location and location error ellipse of earthquake. B indicates location/station plot.

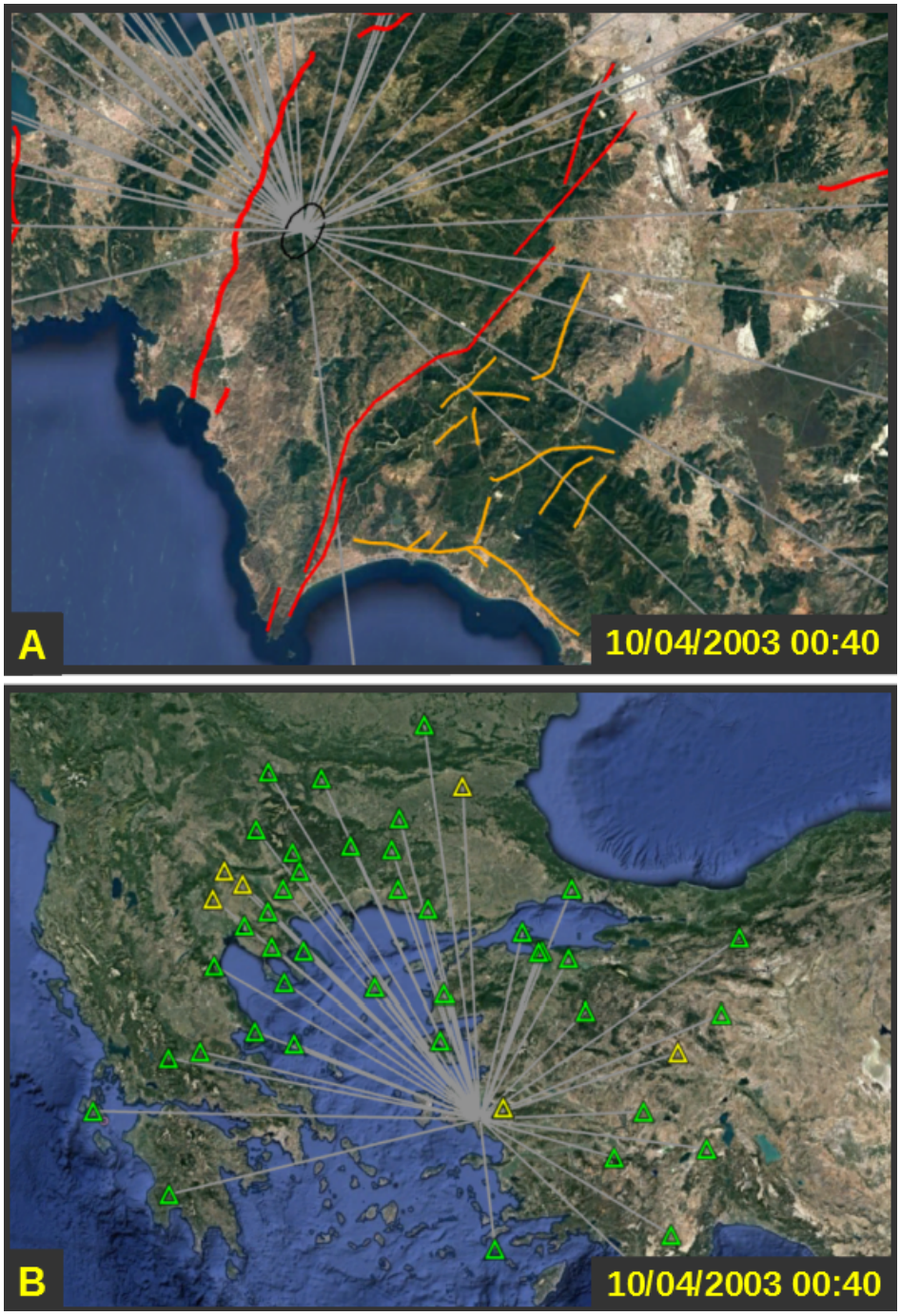

Figure B.26. 10/04/2003 00:40 M 5.8 Earthquake. A indicates location and location error ellipse of earthquake. B indicates location/station plot.

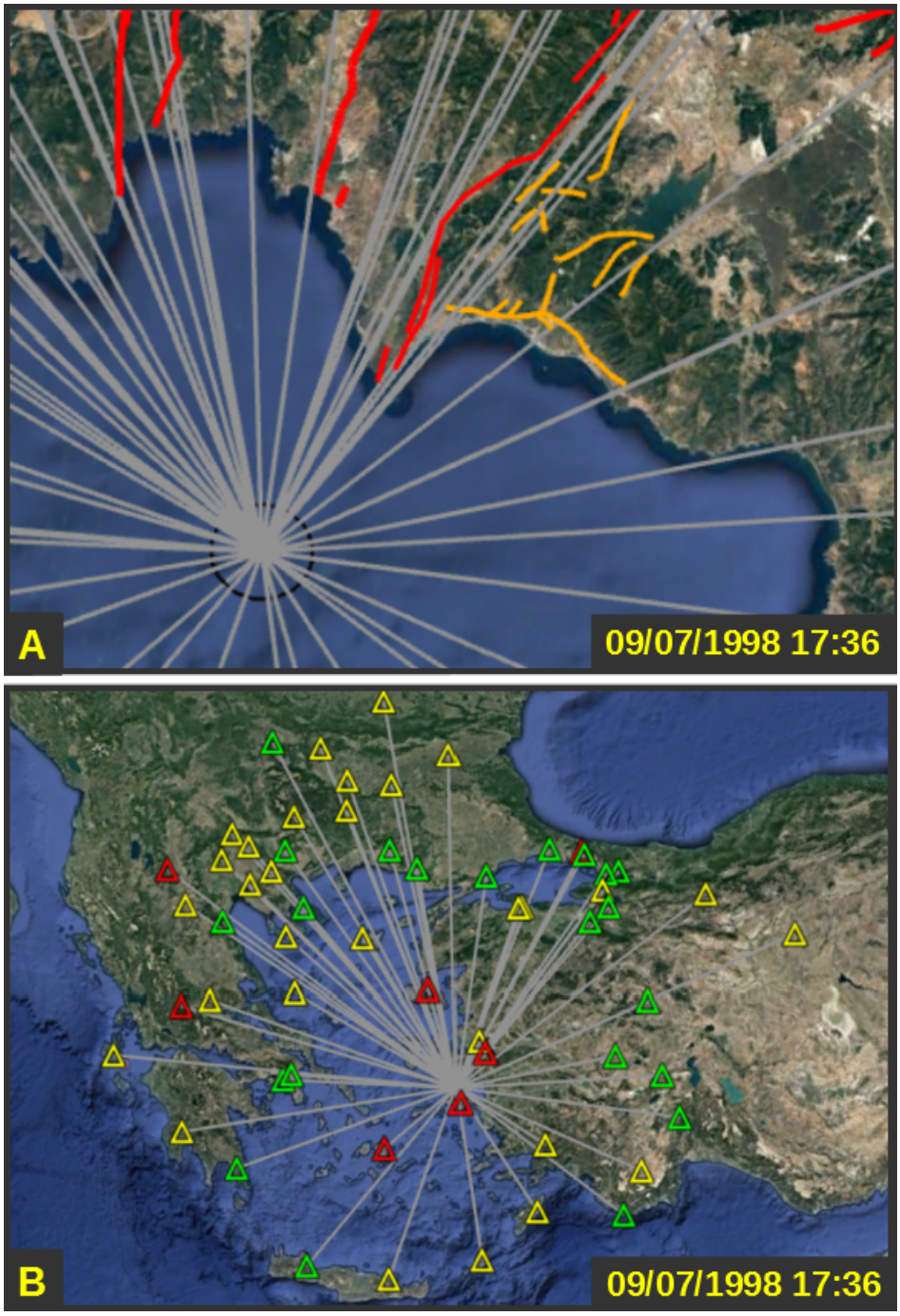

Figure B.27. 09/07/1998 17:36 M 5.3 Earthquake. A indicates location and location error ellipse of earthquake. B indicates location/station plot.

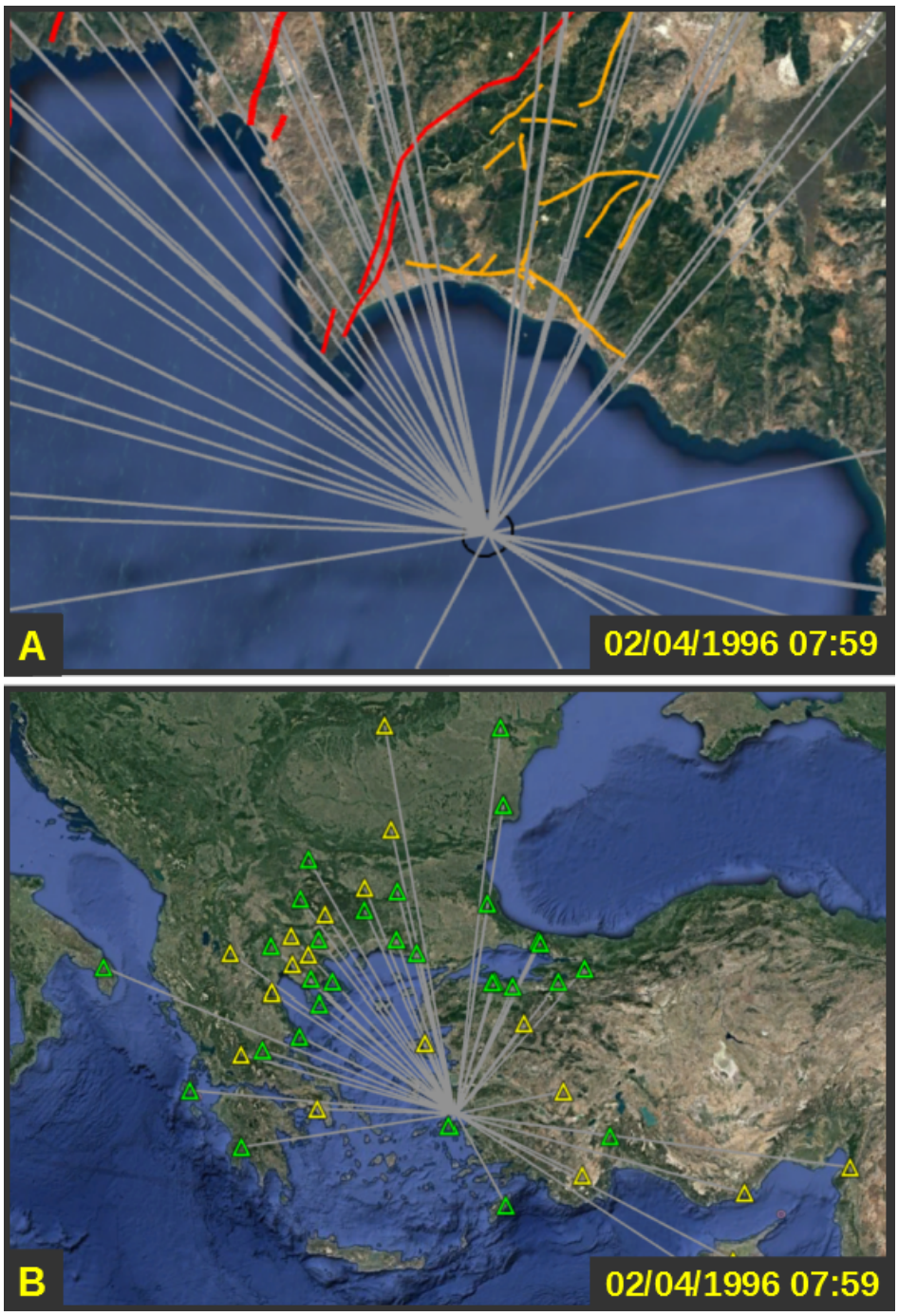

Figure B.28. 02/04/1996 07:59 M 4.9 Earthquake. A indicates location and location error ellipse of earthquake. B indicates location/station plot.

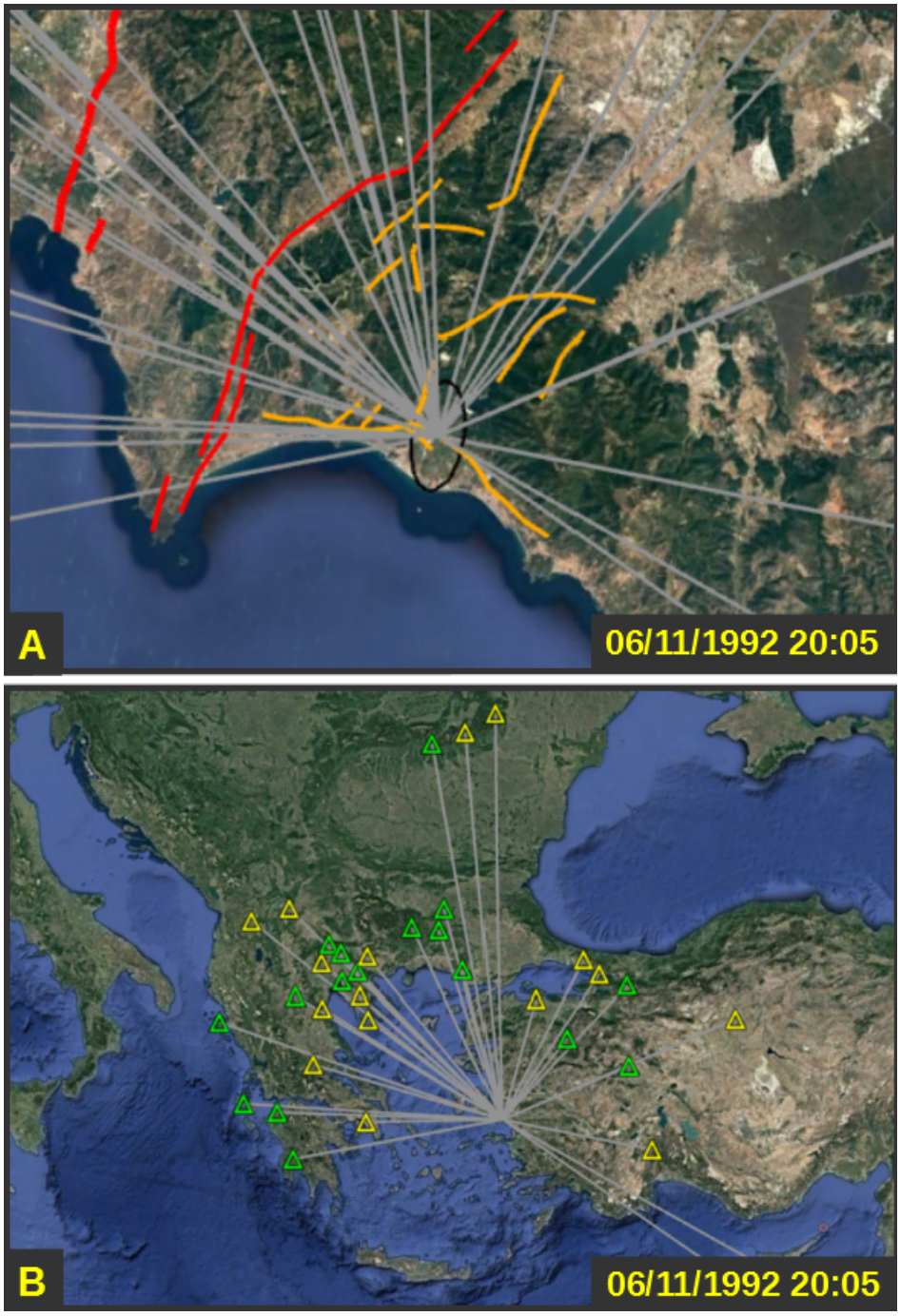

Figure B.29. 06/11/1992 20:05 M 4.7 Earthquake. A indicates location and location error ellipse of earthquake. B indicates location/station plot.

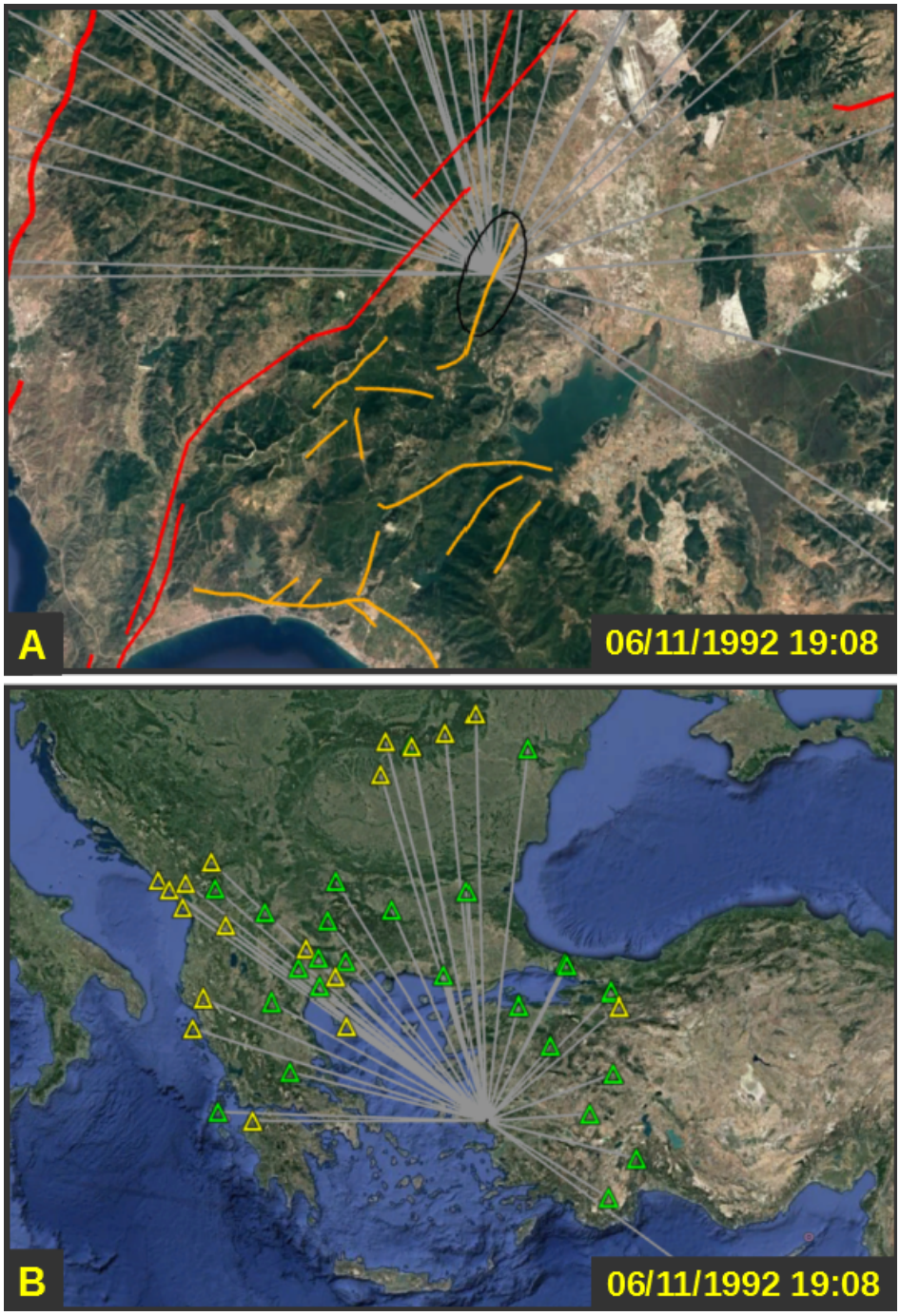

Figure B.30. 06/11/1992 19:08 M 6.0 Earthquake. A indicates location and location error ellipse of earthquake. B indicates location/station plot.

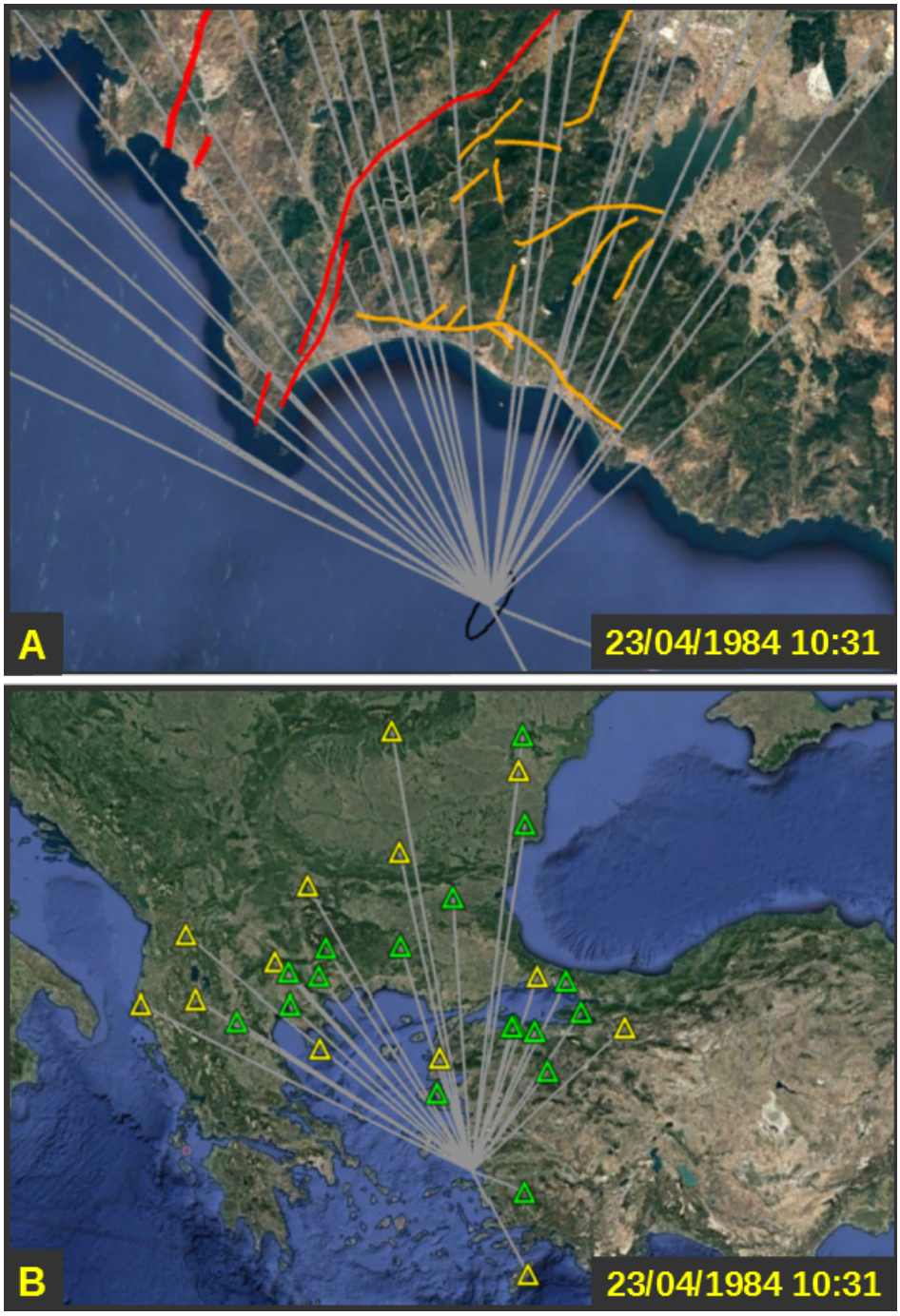

Figure B.31. 23/04/1984 10:31 M 4.6 Earthquake. A indicates location and location error ellipse of earthquake. B indicates location/station plot.

Figure B.32. 16/12/1977 07:37 M 5.3 Earthquake. A indicates location and location error ellipse of earthquake. B indicates location/station plot.

Figure B.33. 01/02/1974 00:01 M 5.3 Earthquake. A indicates location and location error ellipse of earthquake. B indicates location/station plot.

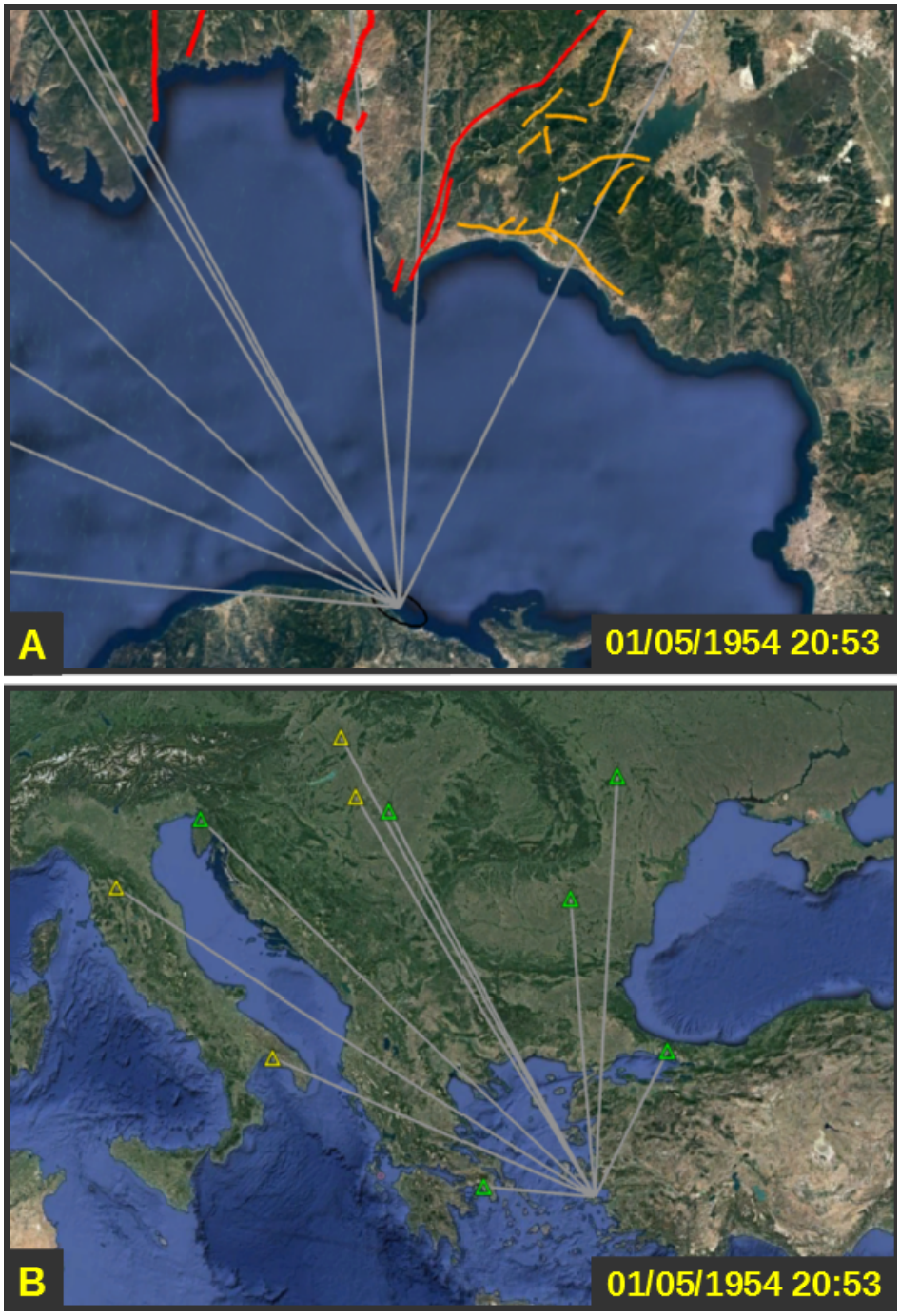

Figure B.34. 01/05/1954 20:53 M 5.4 Earthquake. A indicates location and location error ellipse of earthquake. B indicates location/station plot.

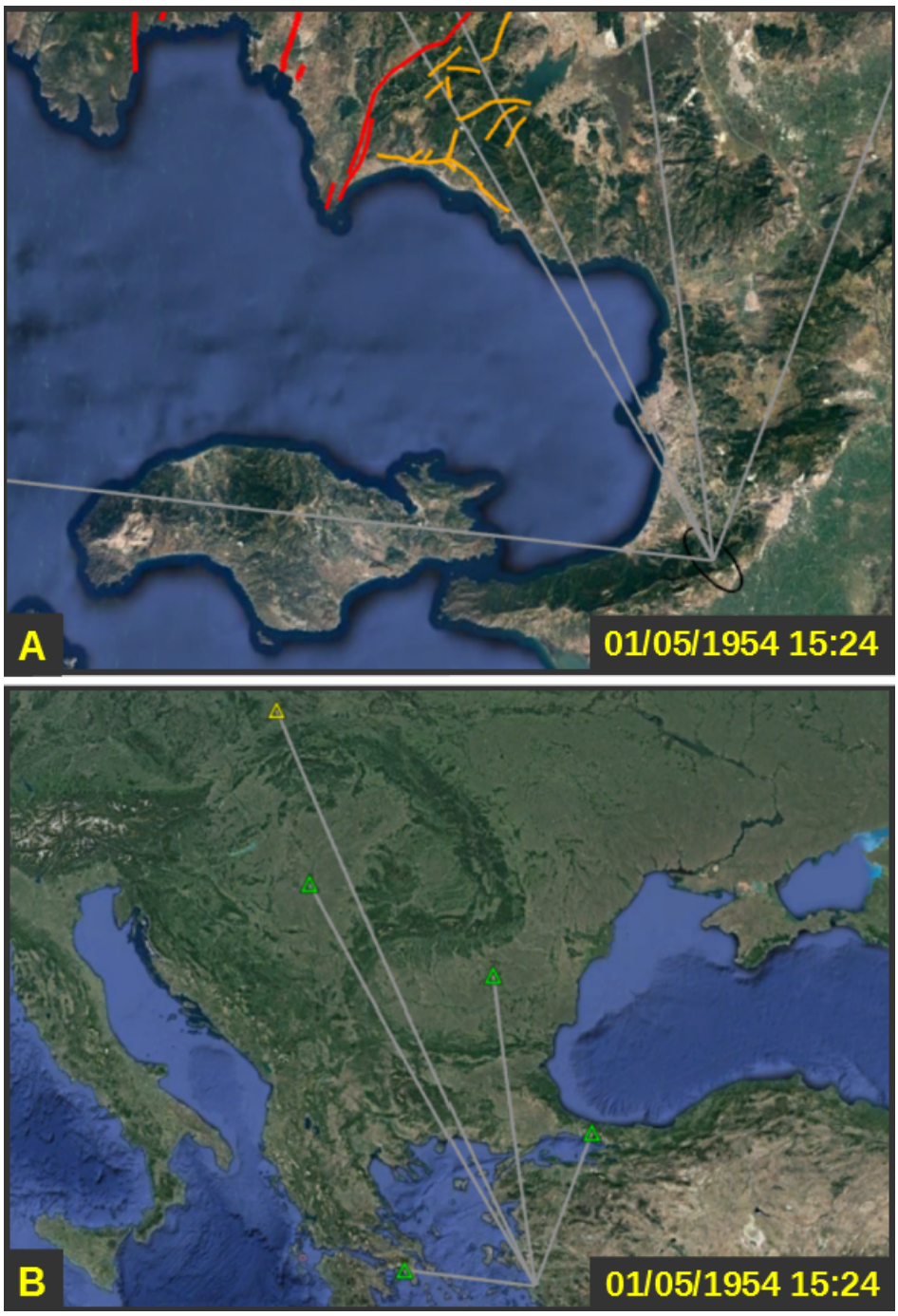

Figure B.35. 01/05/1954 15:24 M 5.3 Earthquake. A indicates location and location error ellipse of earthquake. B indicates location/station plot.

Figure B.36. 02/05/1953 18:37 M 5.1 Earthquake. A indicates location and location error ellipse of earthquake. B indicates location/station plot.

Figure B.37. 01/05/1953 20:06 M 4.9 Earthquake. A indicates location and location error ellipse of earthquake. B indicates location/station plot.

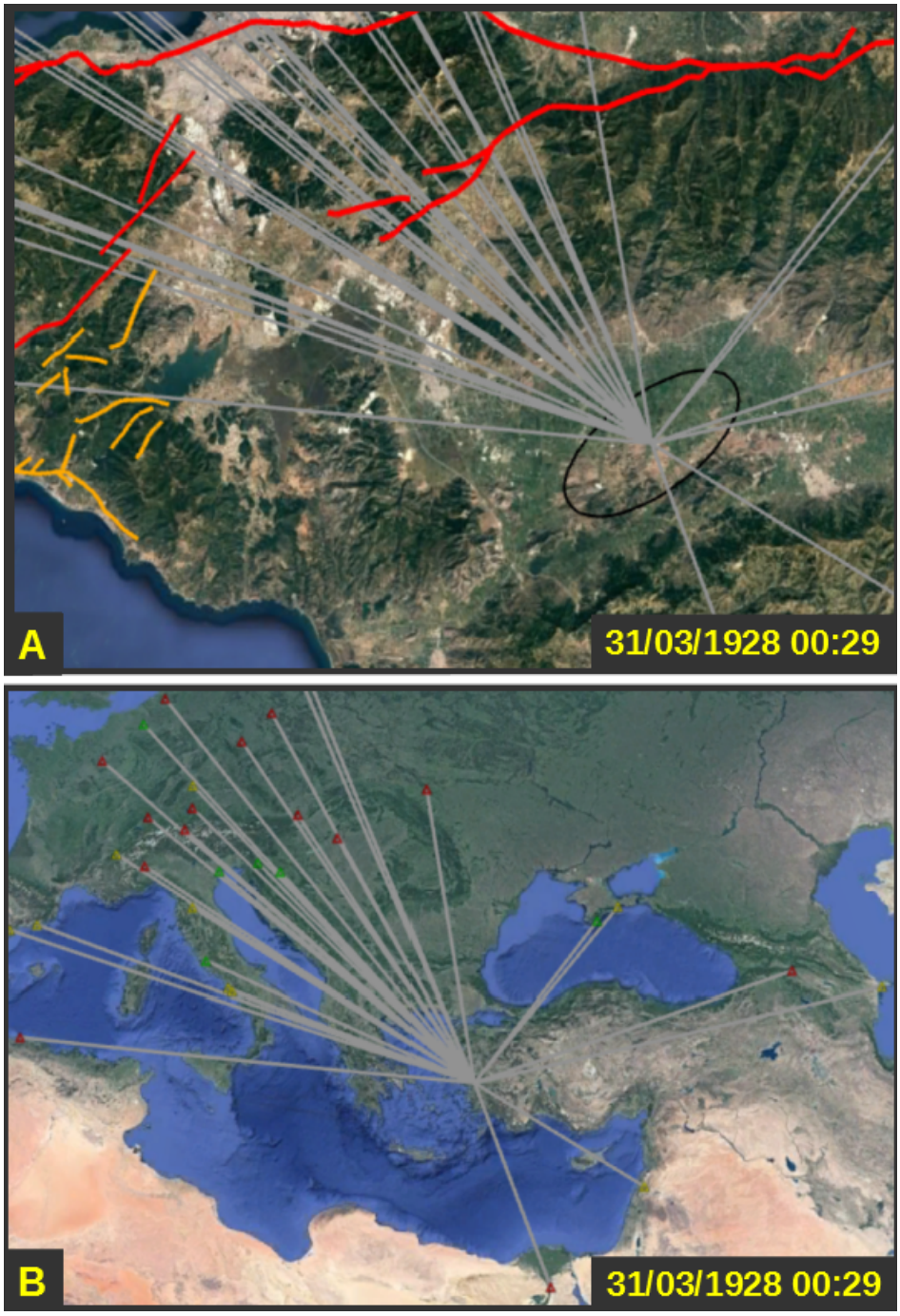

Figure B.38. 31/03/1928 00:29 M 6.2 Earthquake. A indicates location and location error ellipse of earthquake. B indicates location/station plot.

APPENDIX C: GLOBK OUTPUT OF THE CAMPAIGN BASED STATIONS

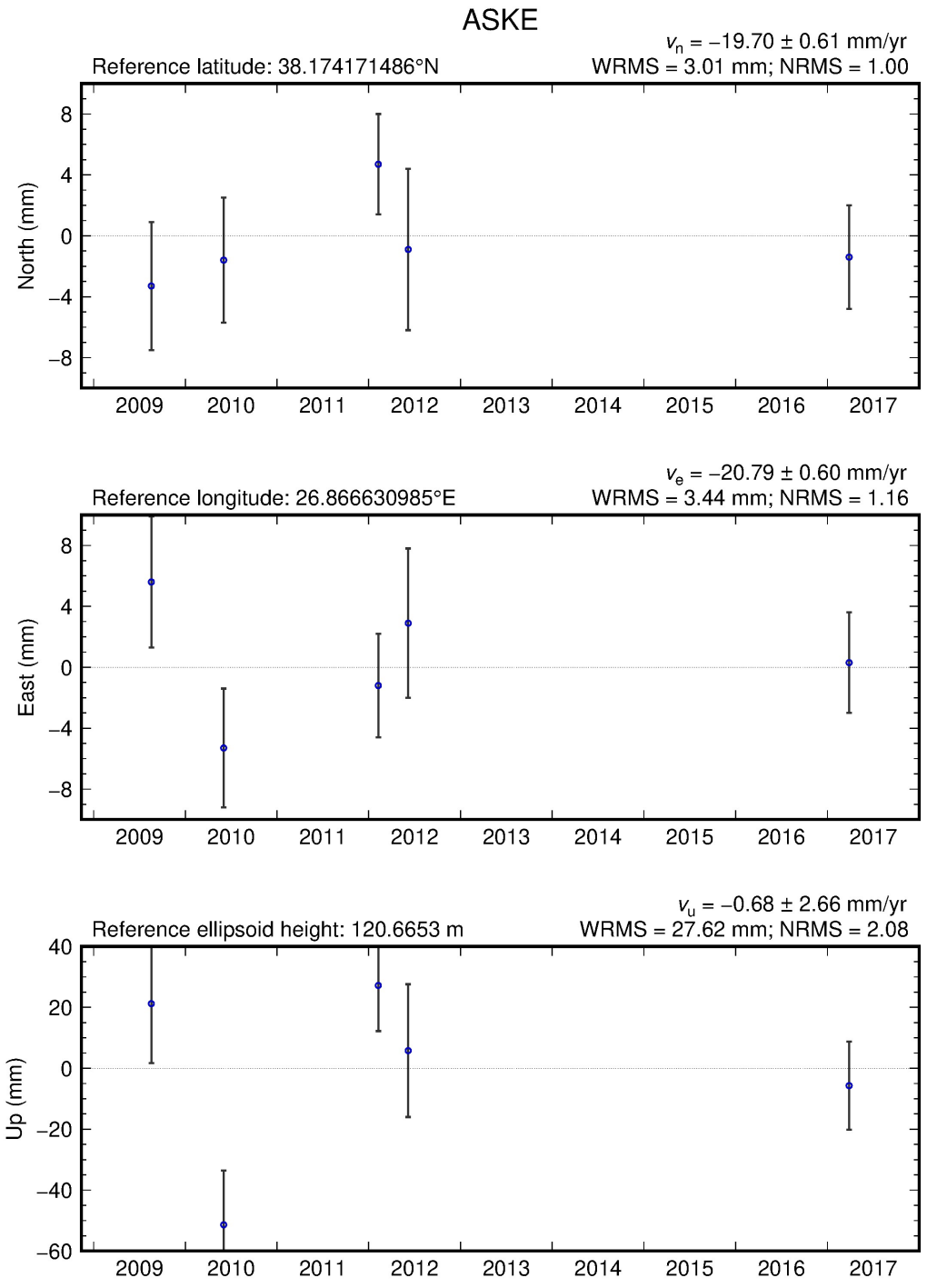

Figure C.1. North, east and up velocities and their uncertainties of ASKE Station.

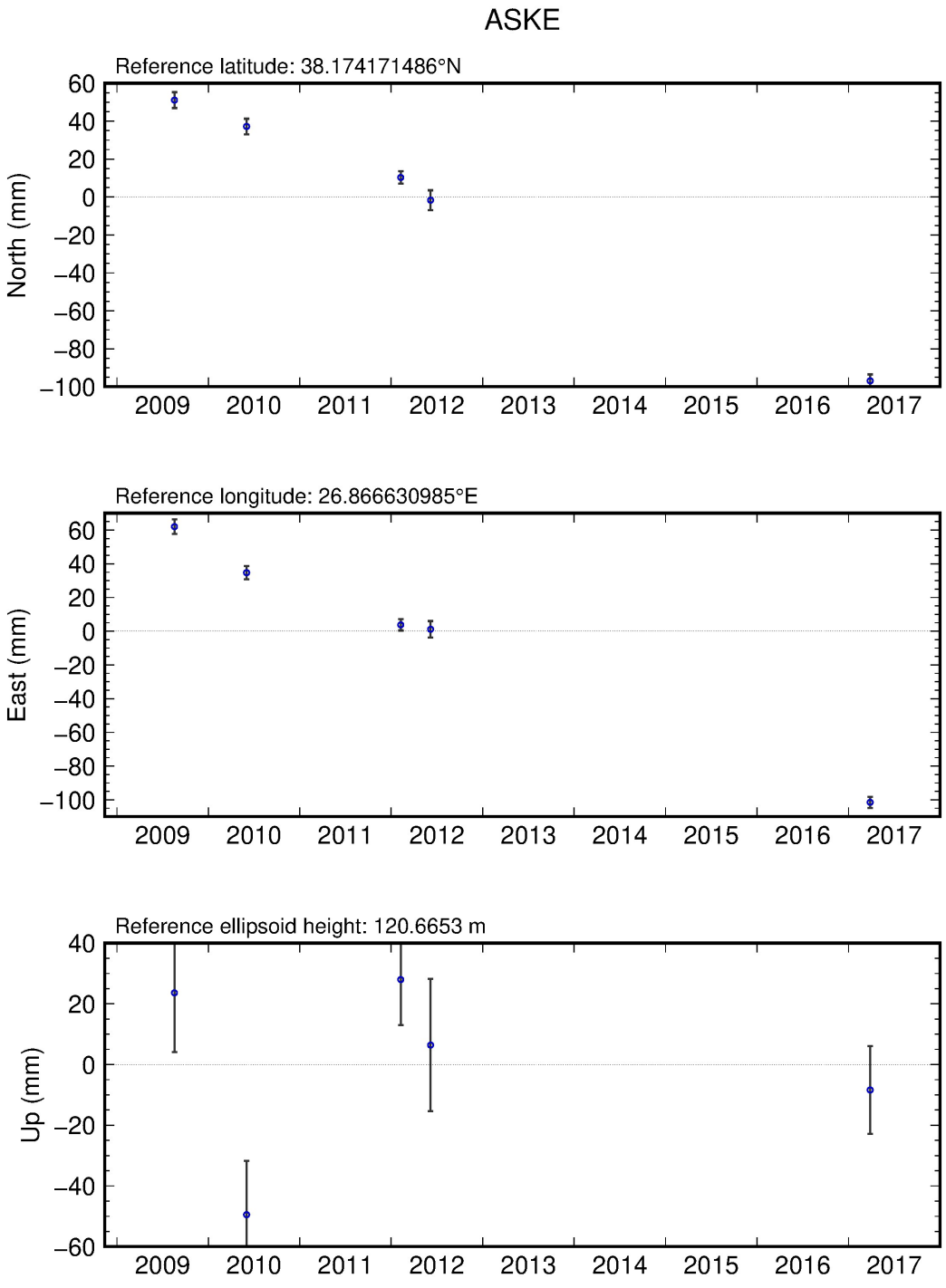

Figure C.2. GPS time series of ASKE Station.

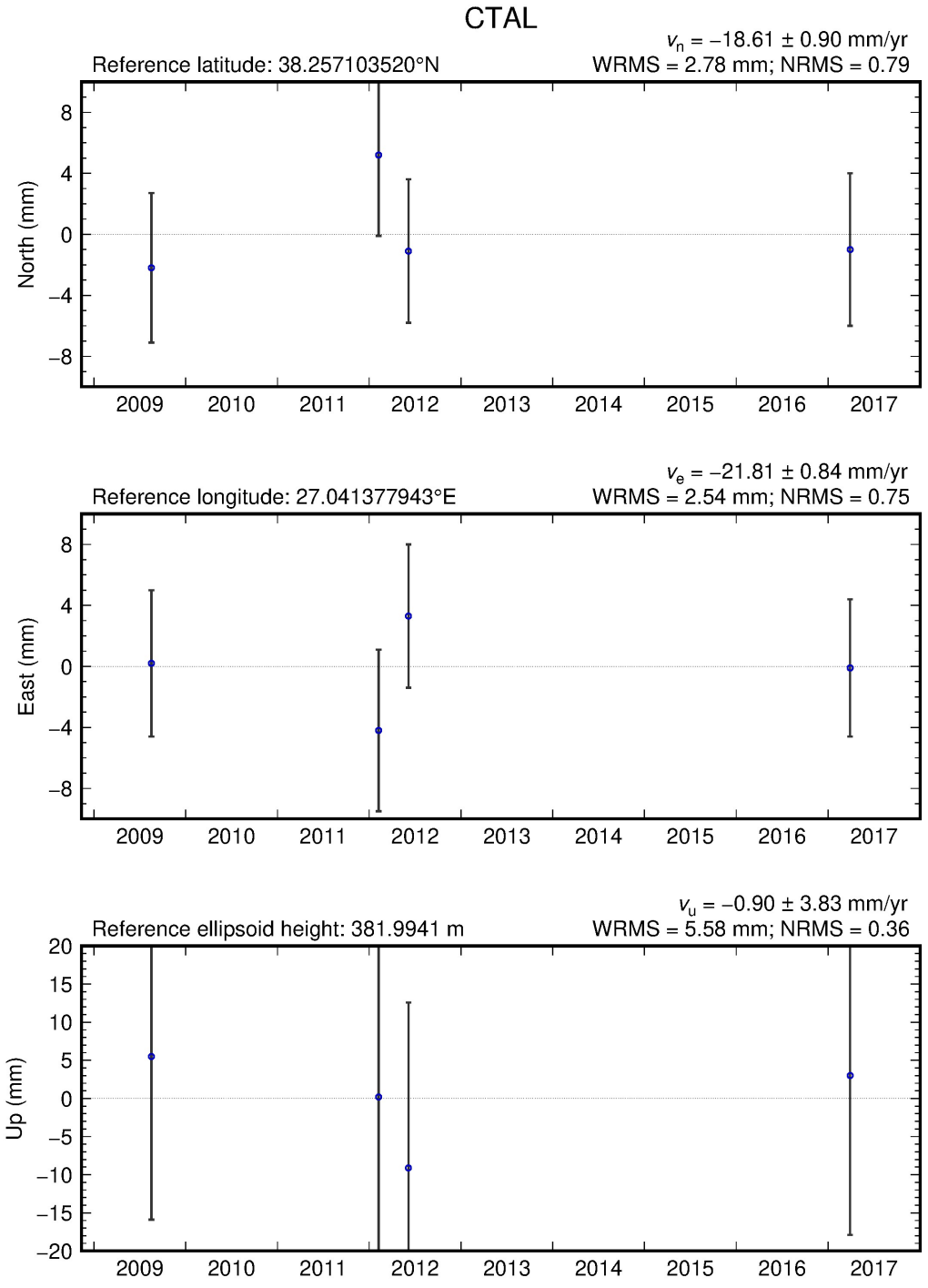

Figure C.3. North, east and up velocities and their uncertainties of CTAL Station.

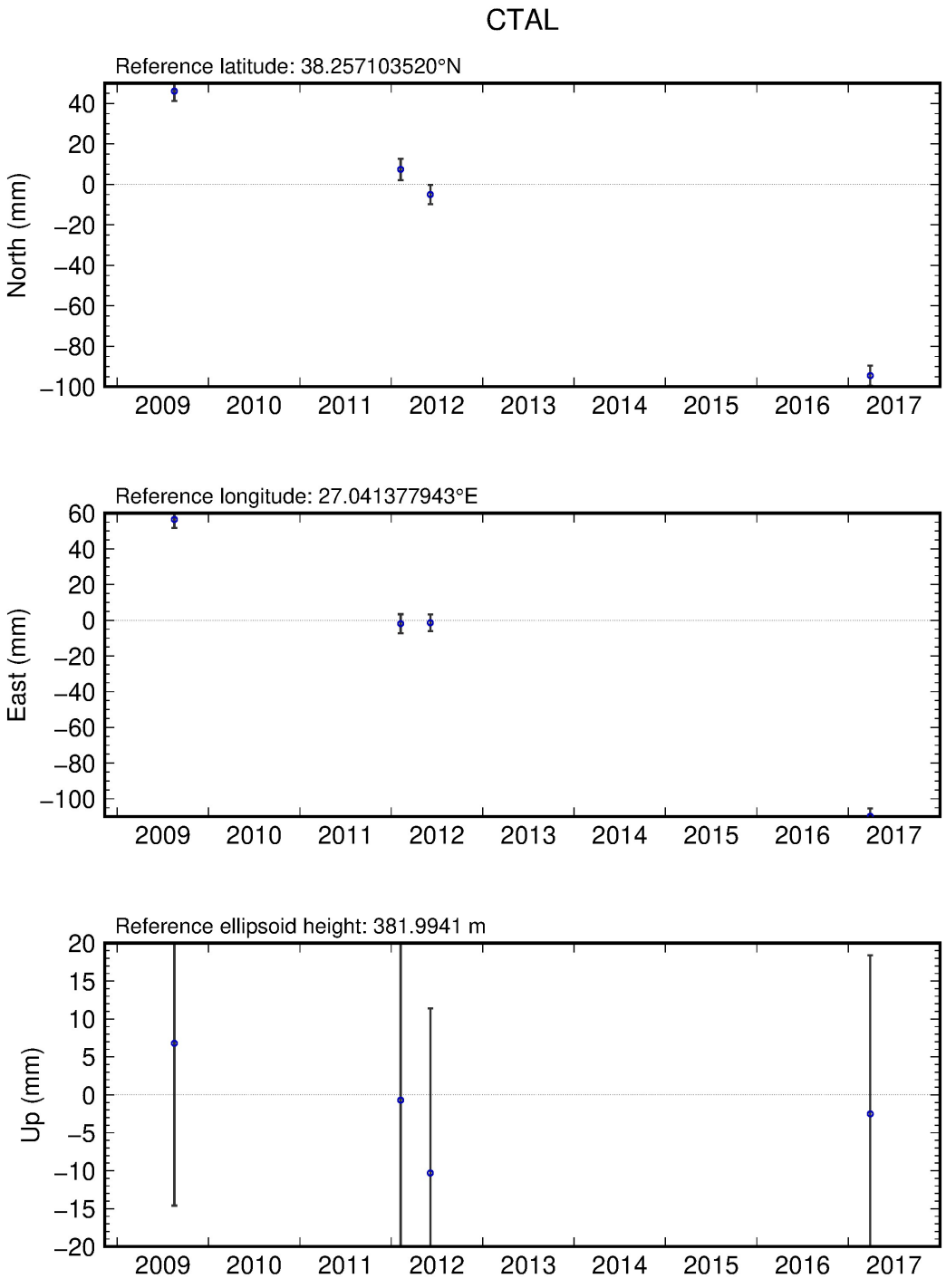

Figure C.4. GPS time series of CTAL Station.

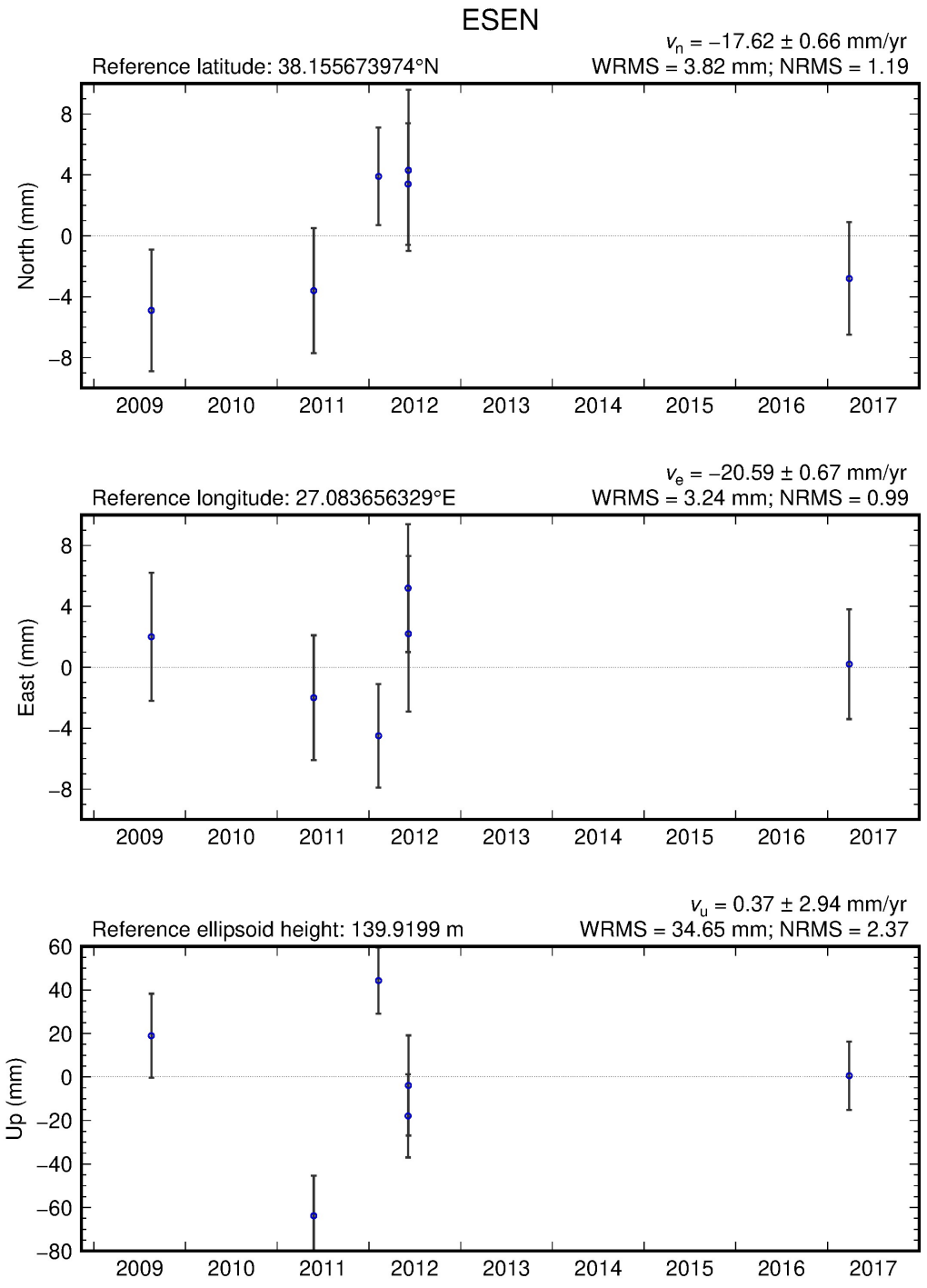

Figure C.5. North, east and up velocities and their uncertainties of ESEN Station.

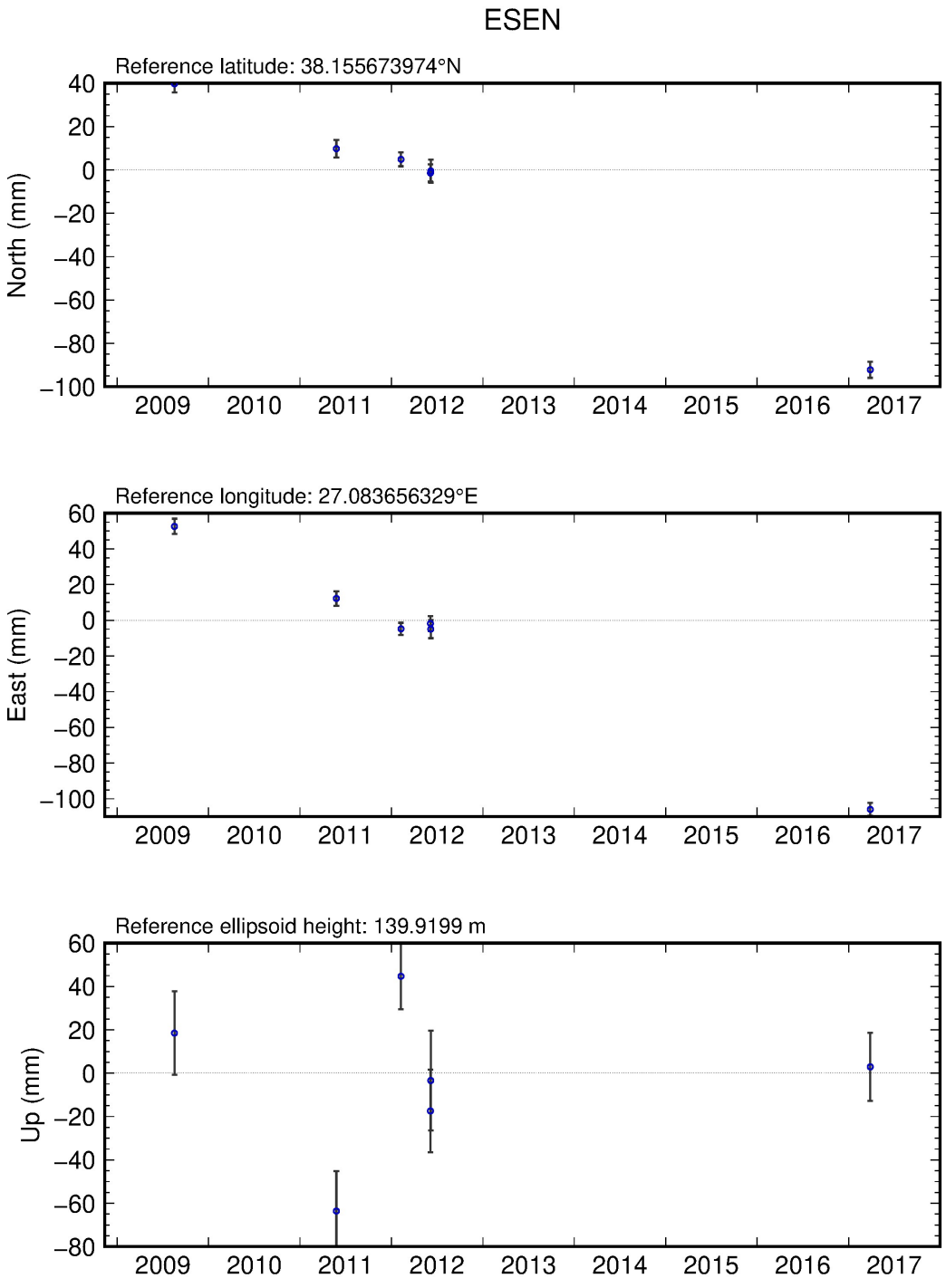

Figure C.6. GPS time series of ESEN Station.

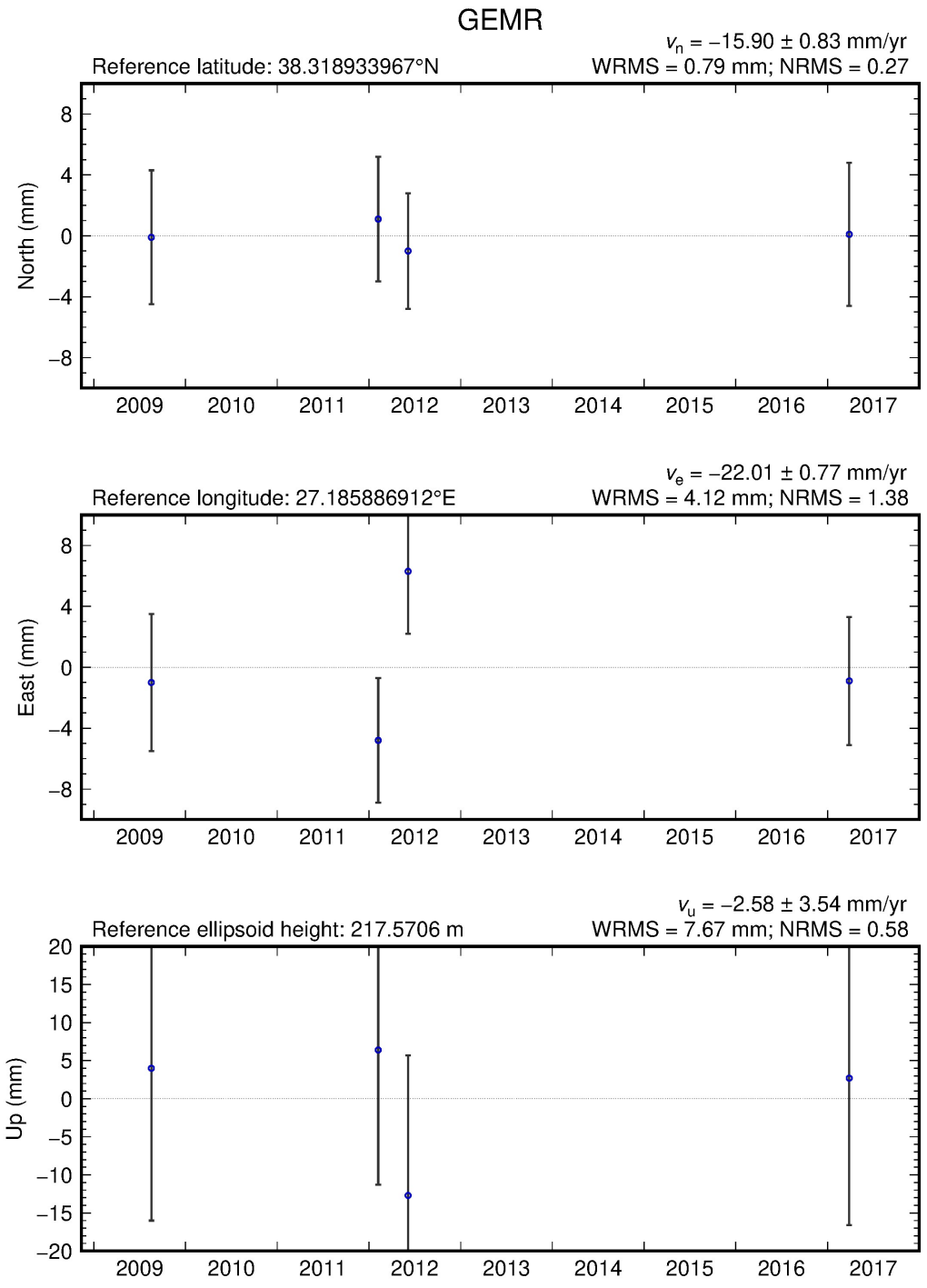

Figure C.7. North, east and up velocities and their uncertainties of GEMR Station.

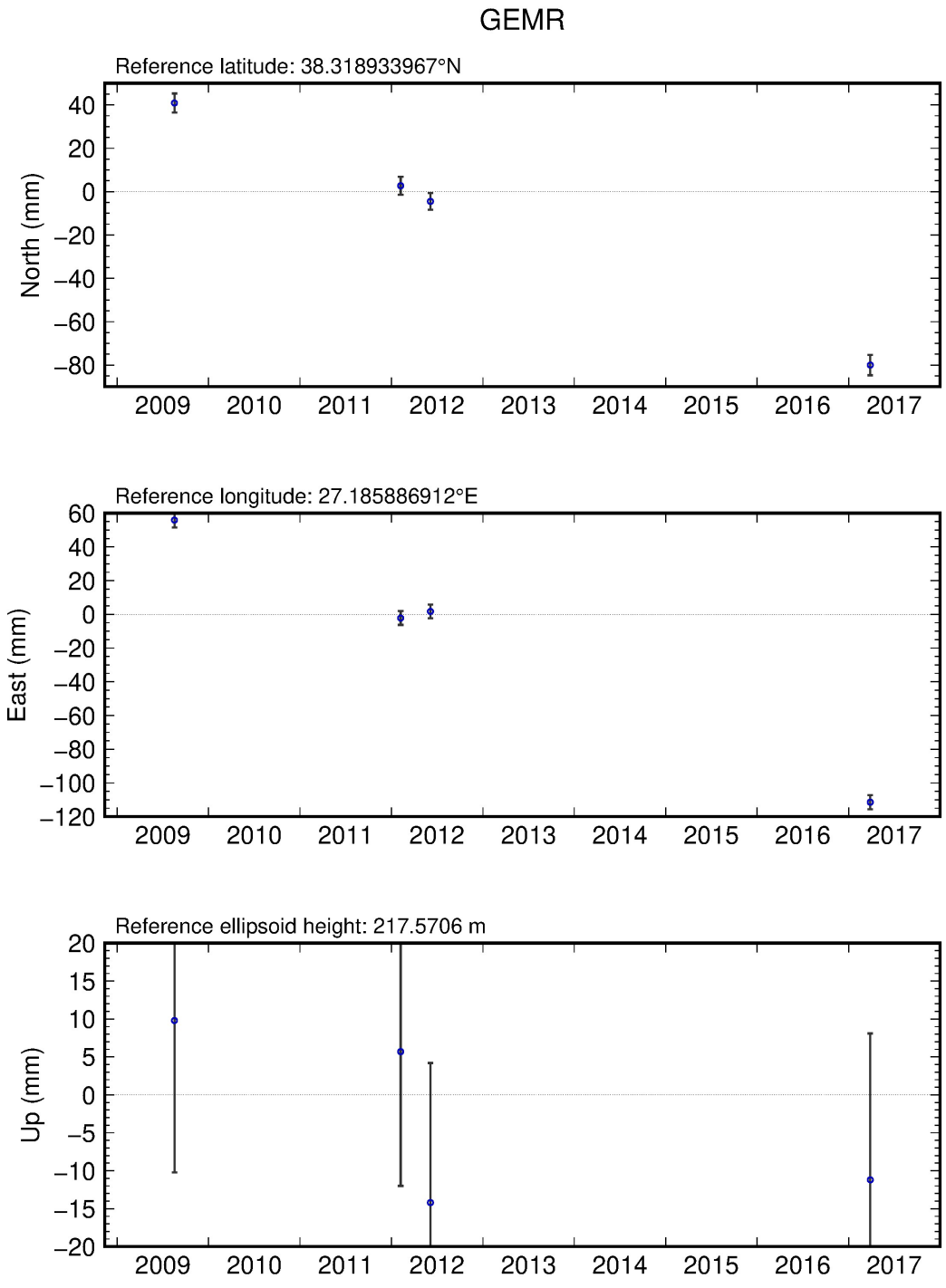

Figure C.8. GPS time series of GEMR Station.

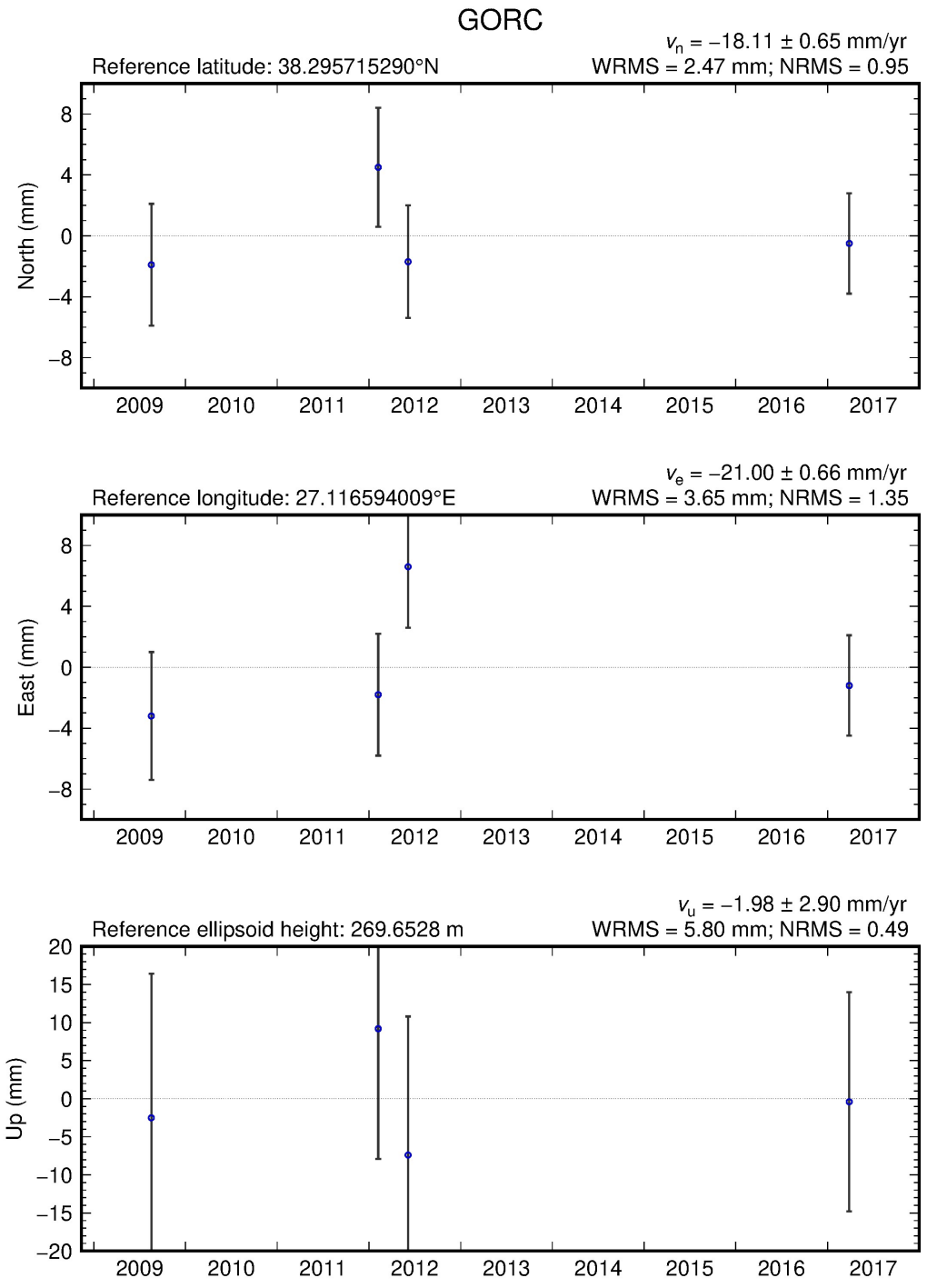

Figure C.9. North, east and up velocities and their uncertainties of GORC Station.

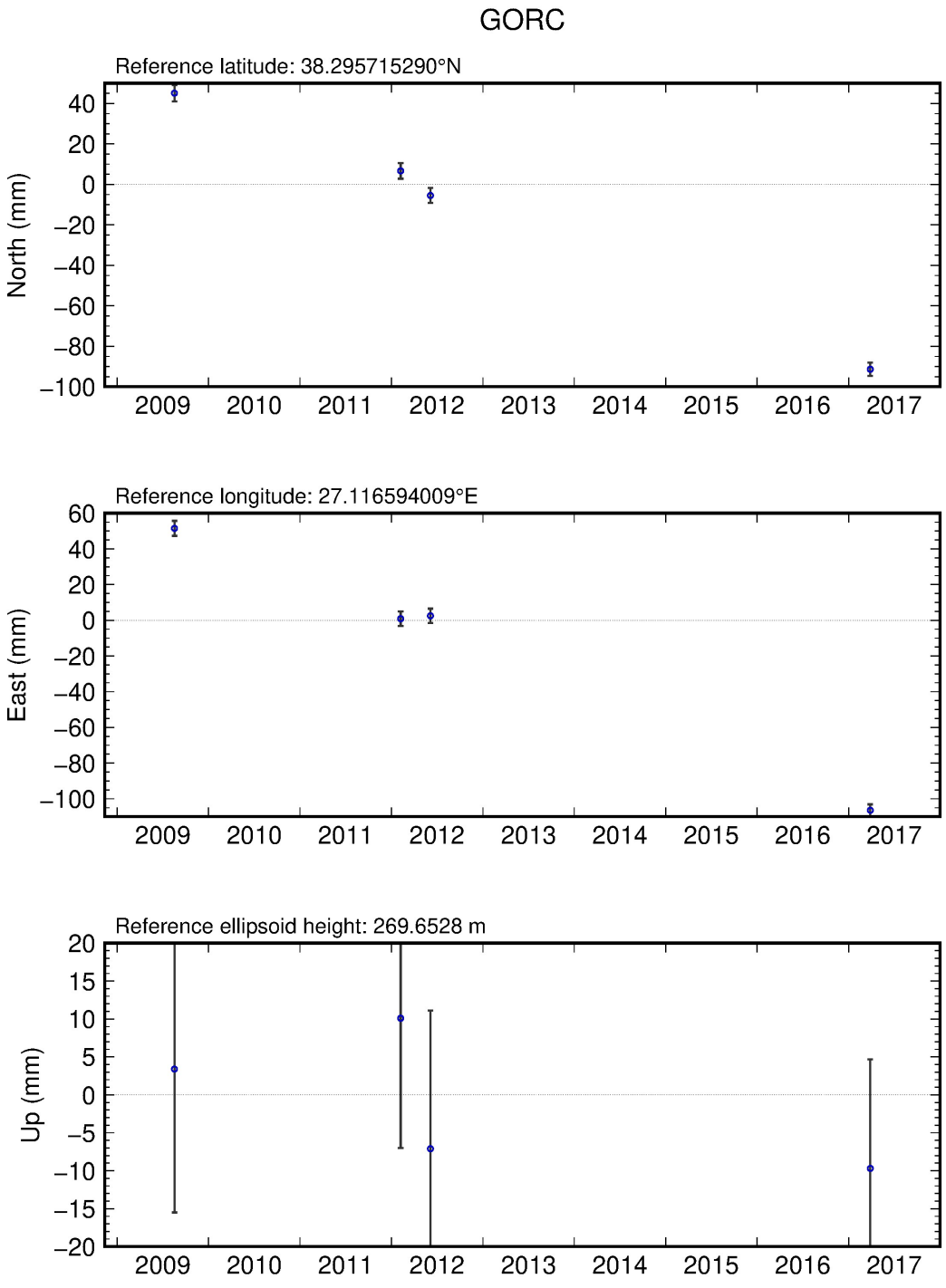

Figure C.10. GPS time series of GORC Station.

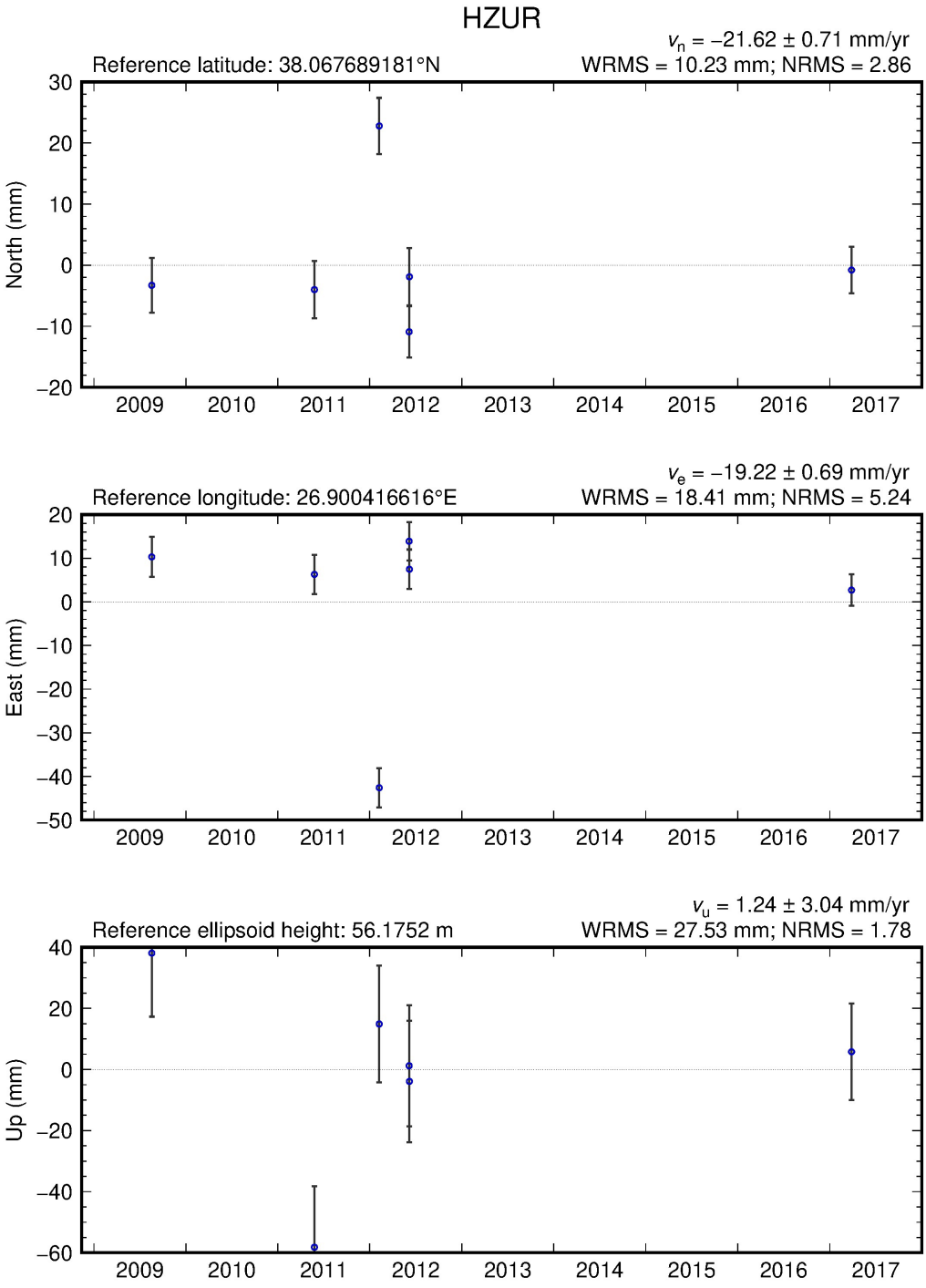

Figure C.11. North, east and up velocities and their uncertainties of HZUR Station.

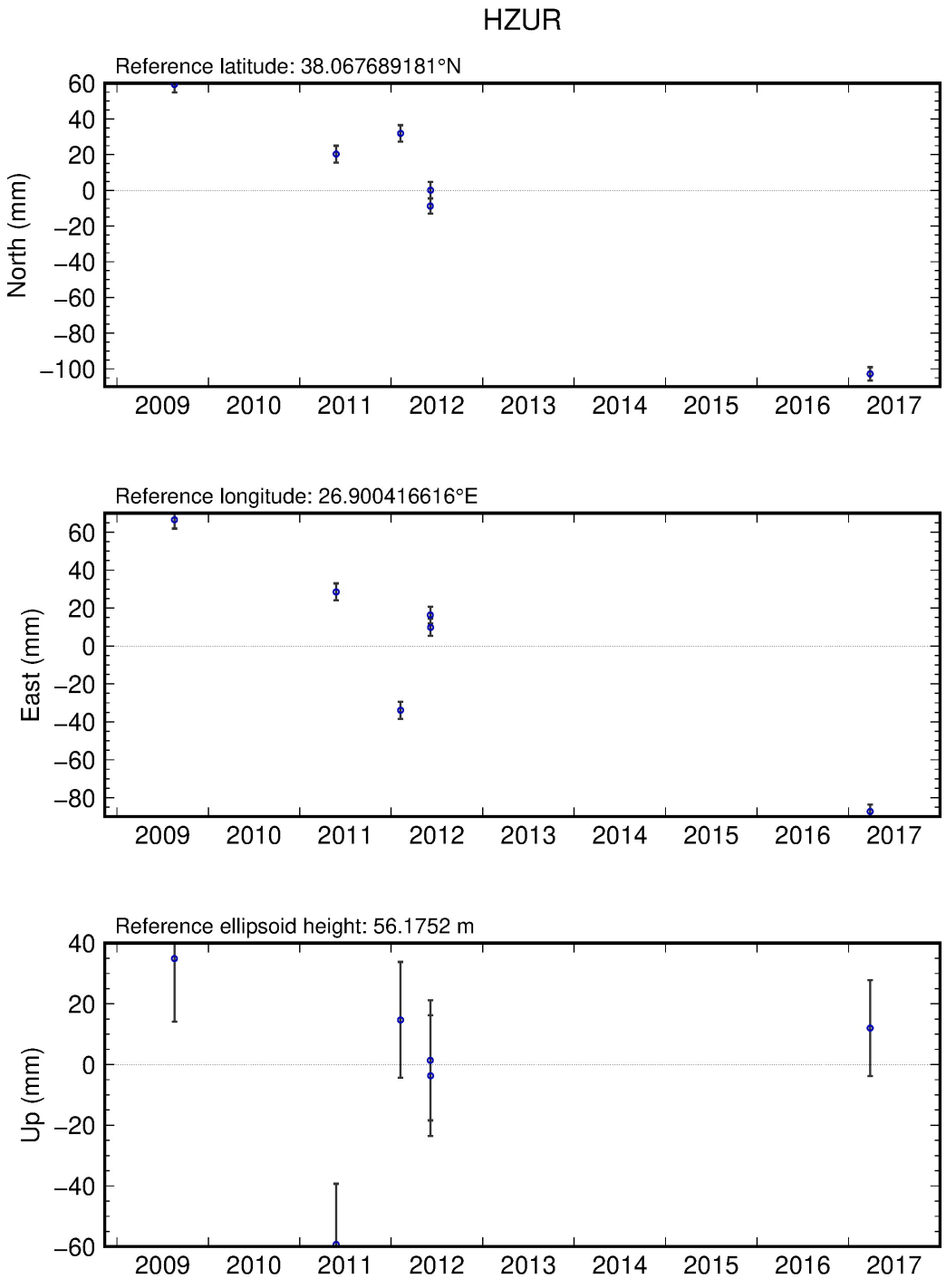

Figure C.12. GPS time series of HZUR Station.

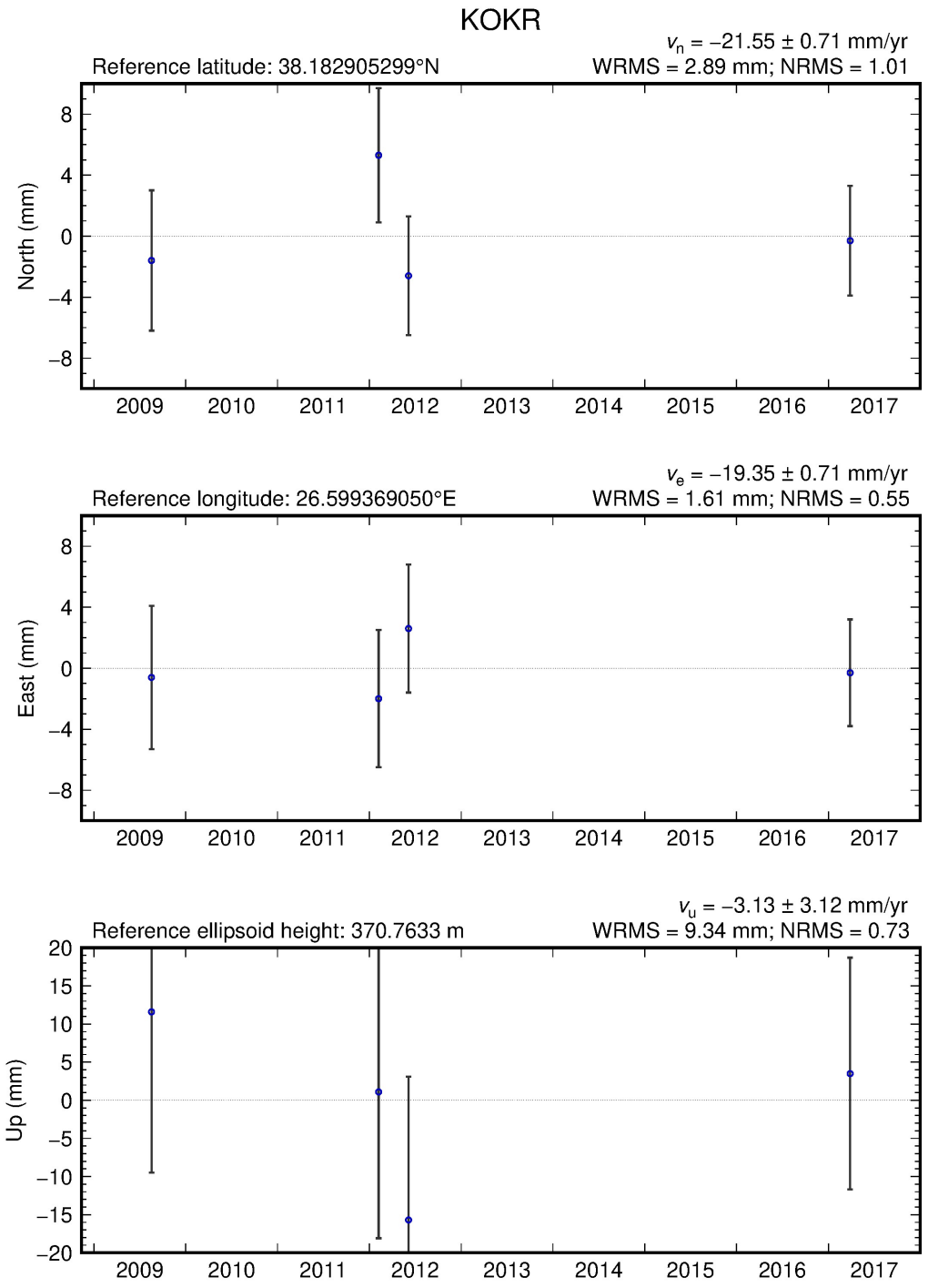

Figure C.13. North, east and up velocities and their uncertainties of KOKR Station.

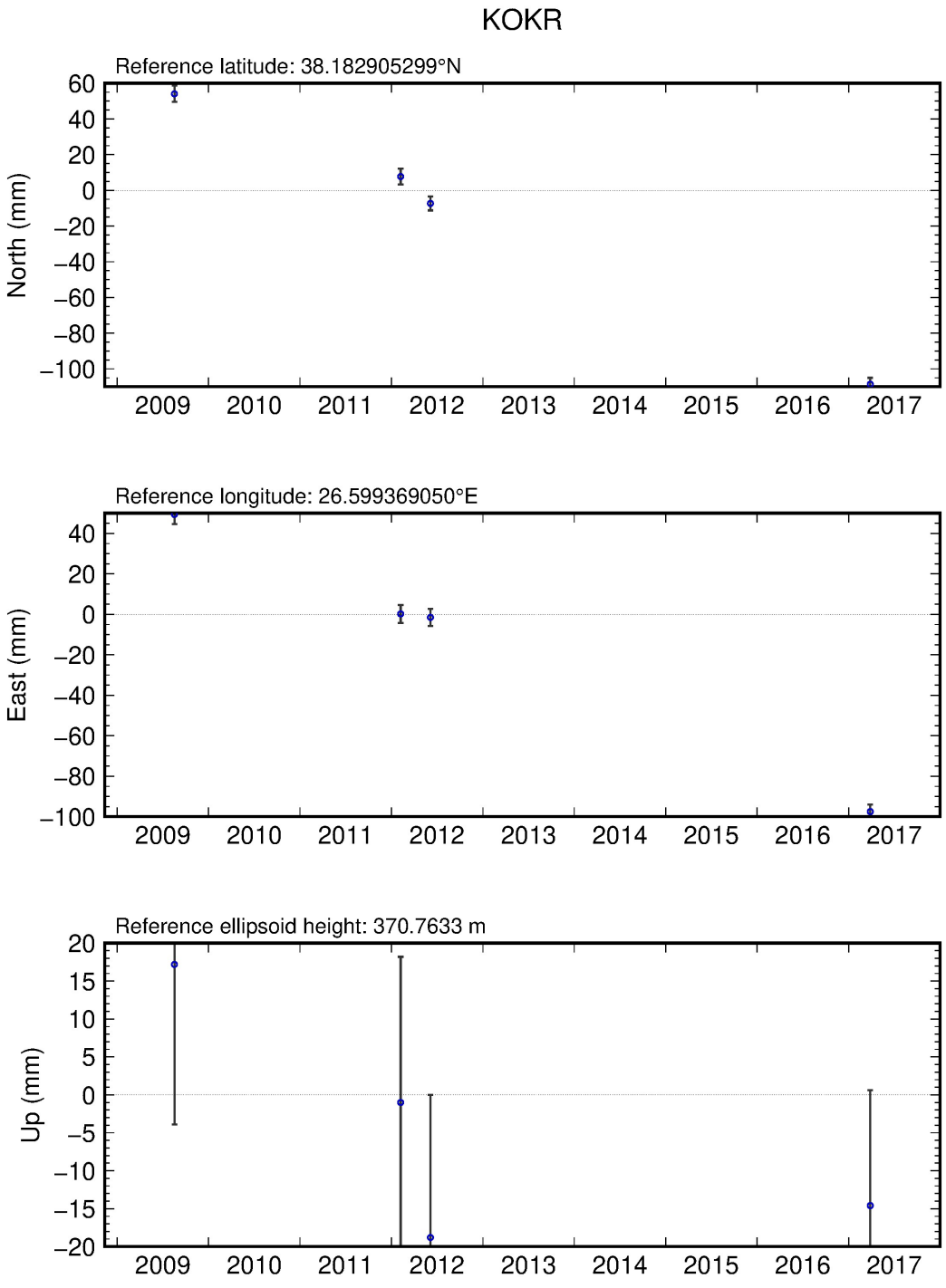

Figure C.14. GPS time series of KOKR Station.

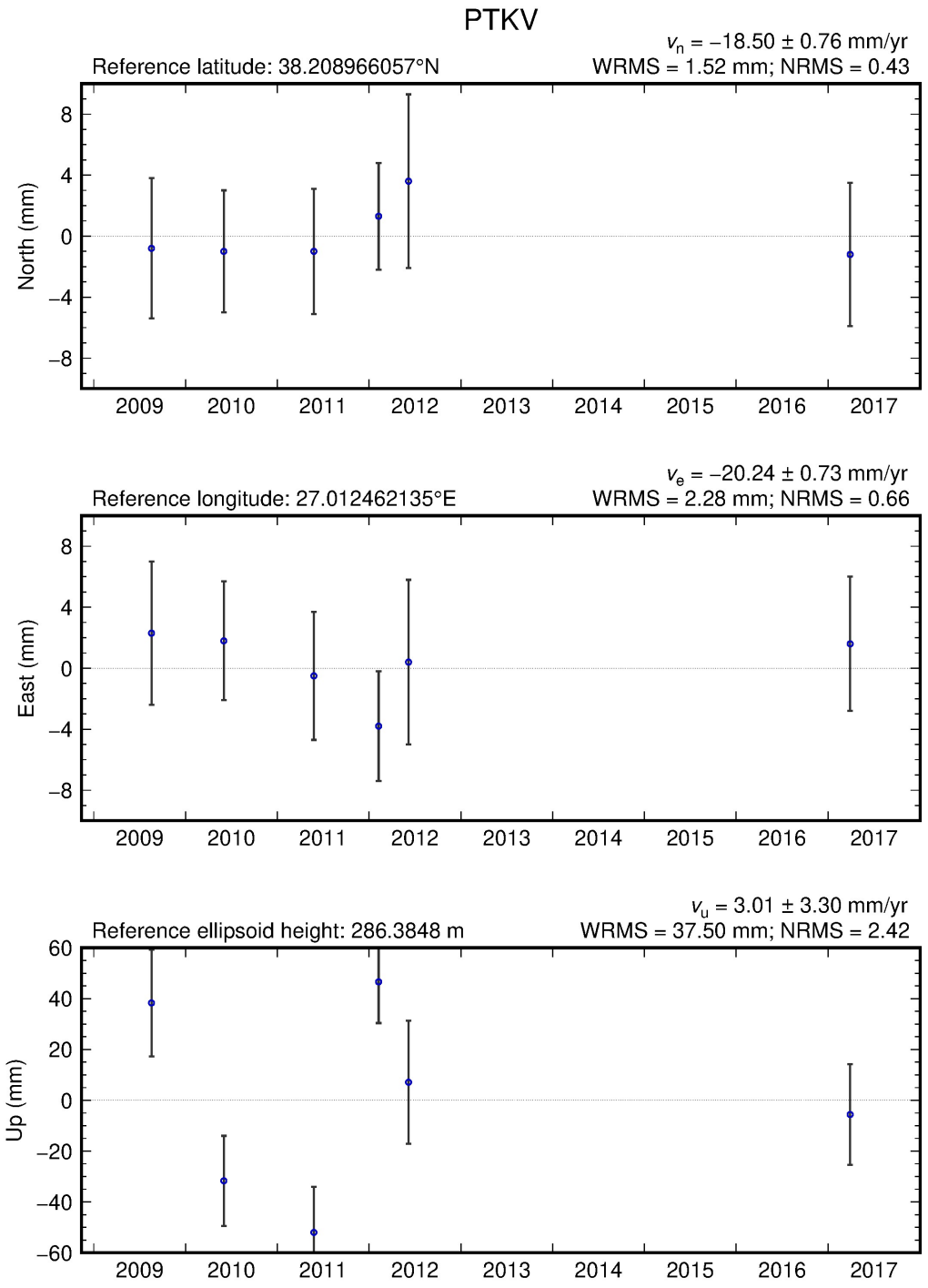

Figure C.15. North, east and up velocities and their uncertainties of PTKV Station.

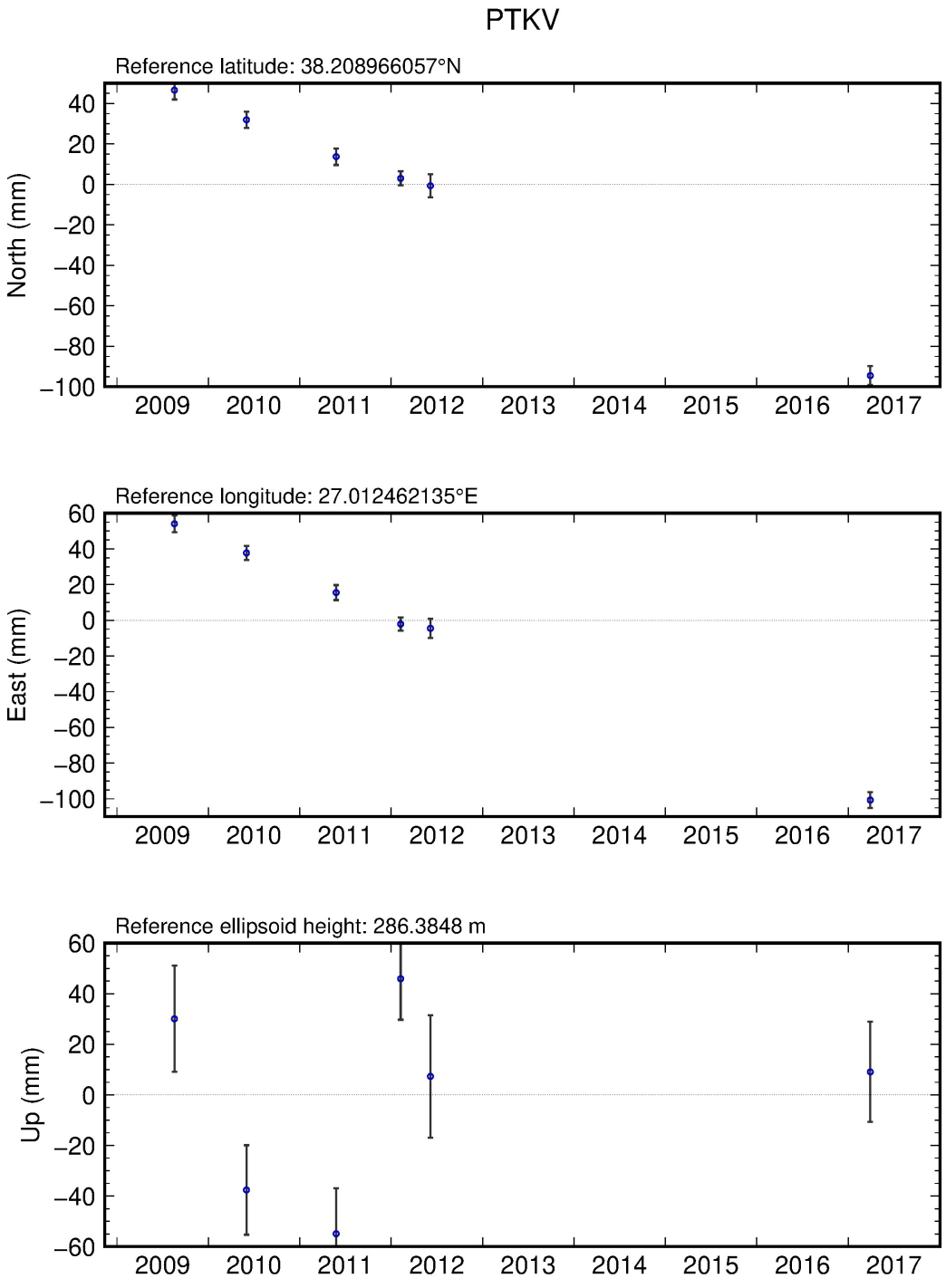

Figure C.16. GPS time series of PTKV Station.

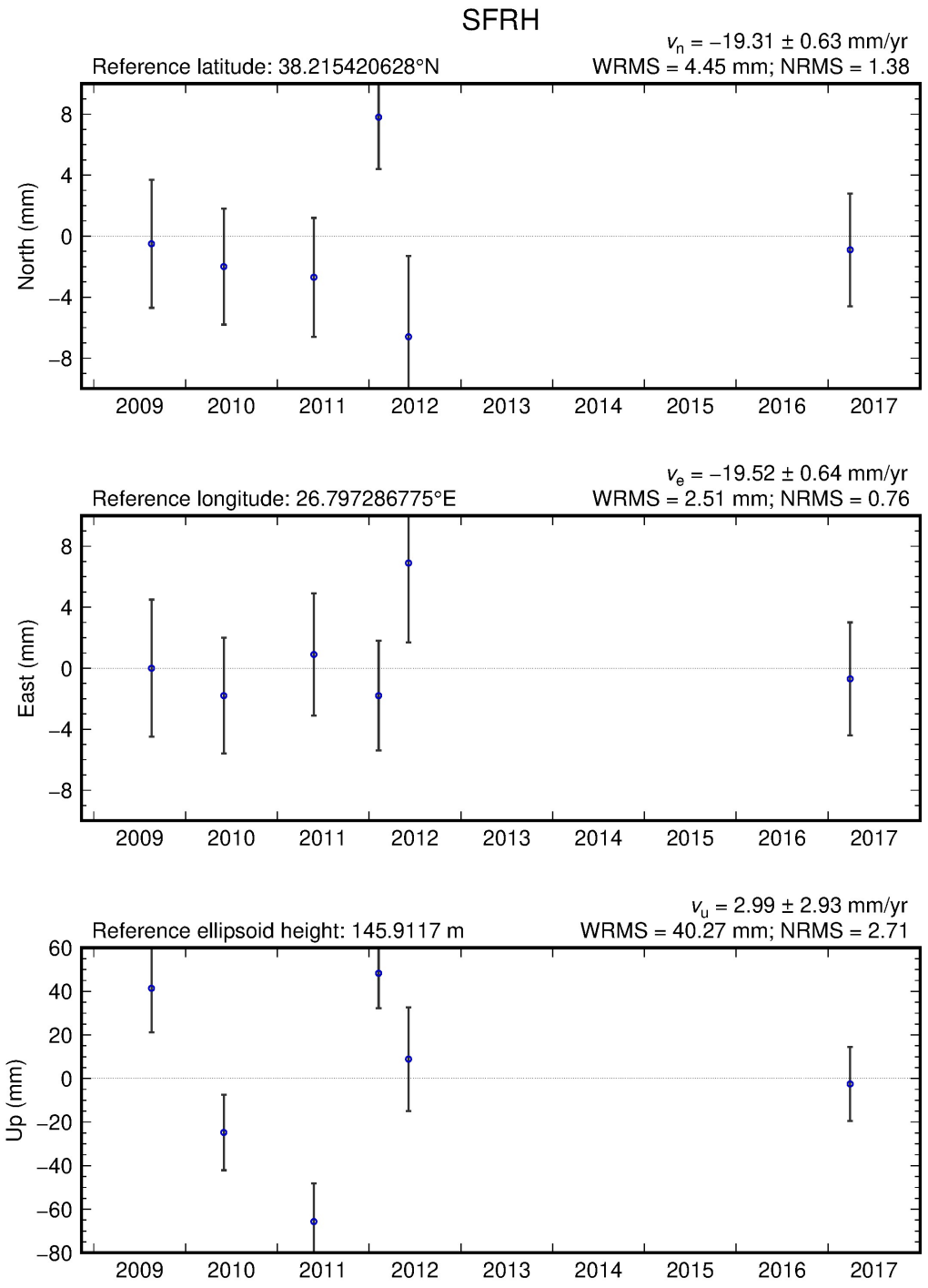

Figure C.17. North, east and up velocities and their uncertainties of SFRH Station.

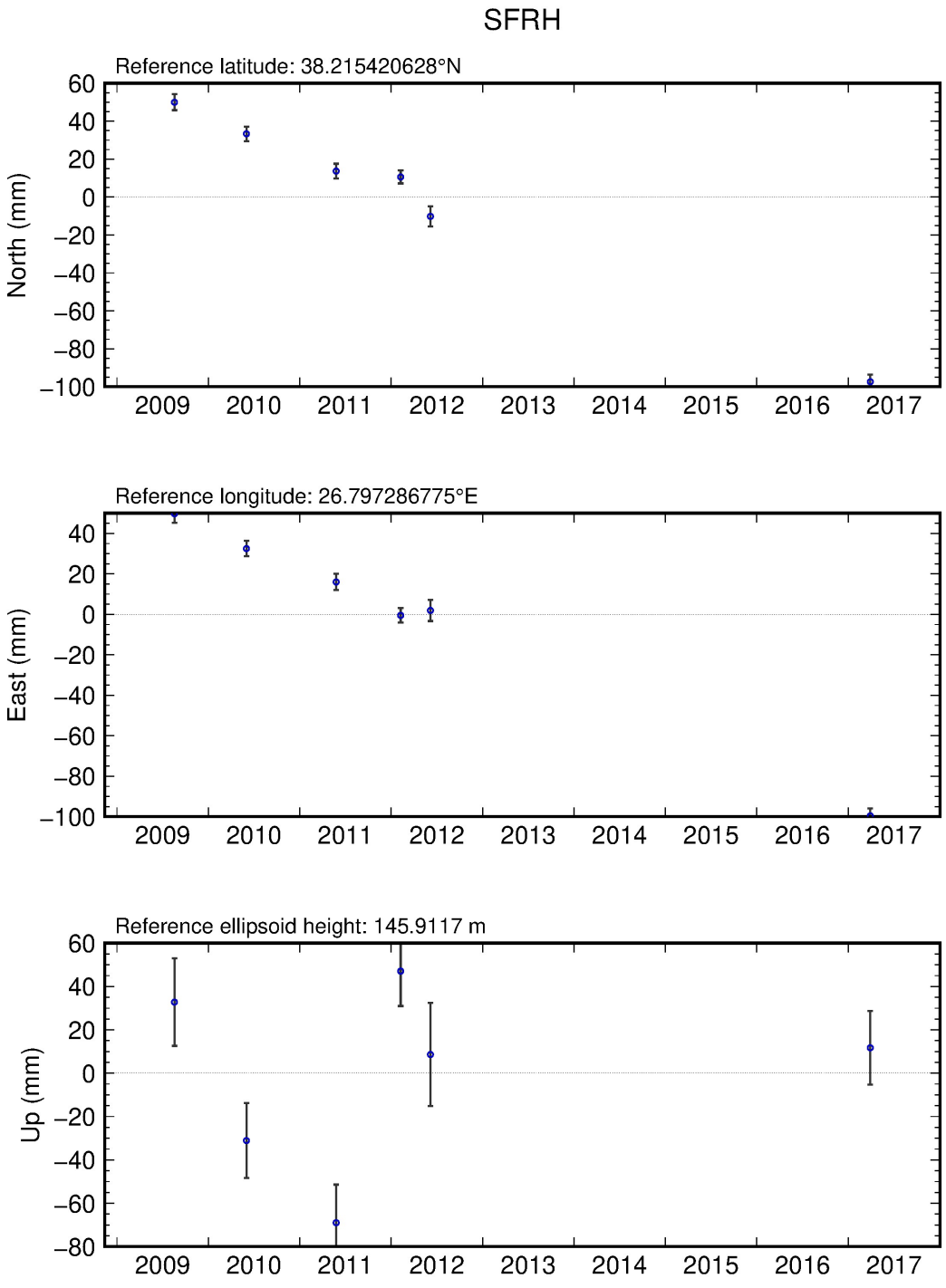

Figure C.18. GPS time series of SFRH Station.

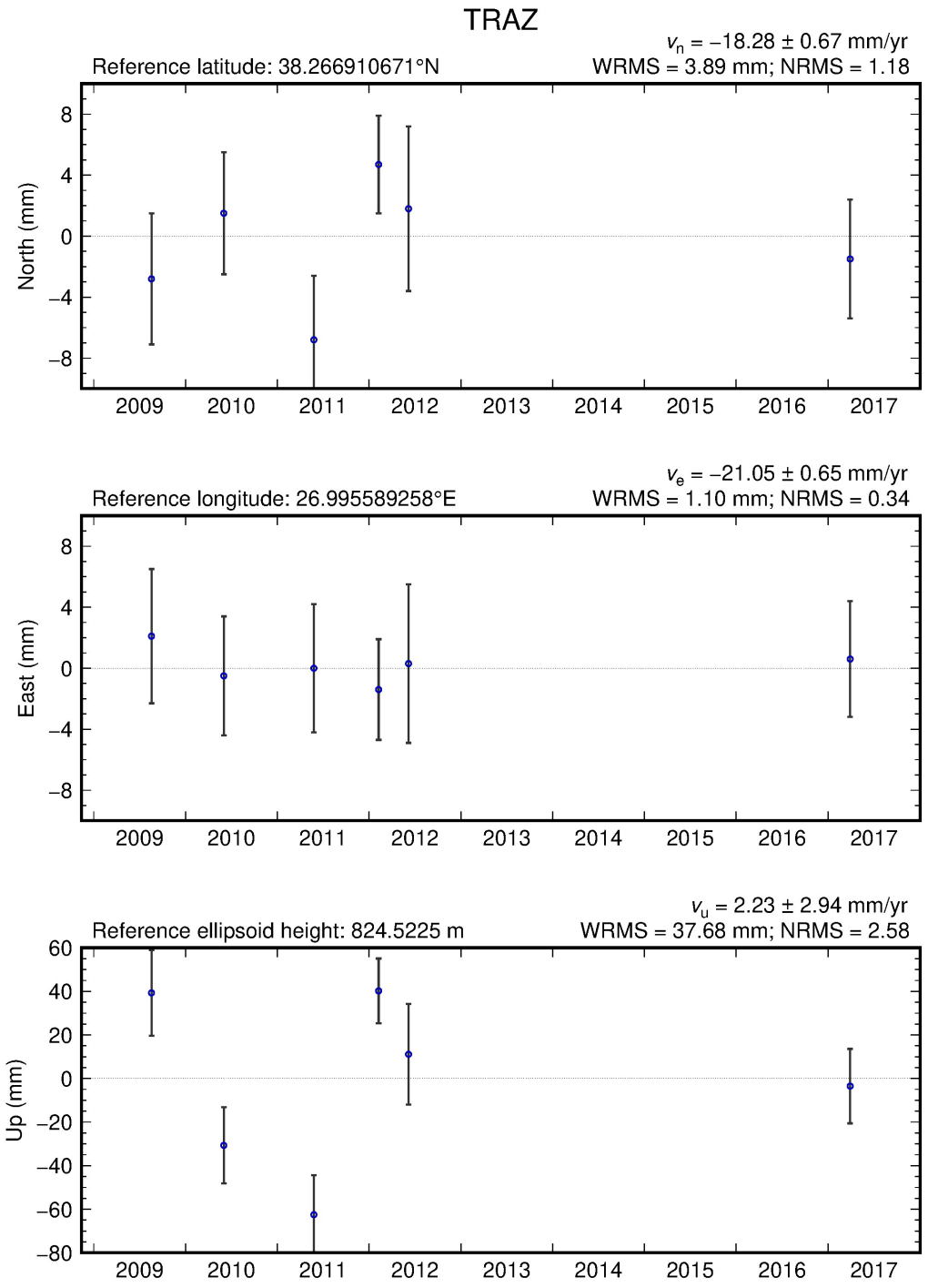

Figure C.19. North, east and up velocities and their uncertainties of TRAZ Station.

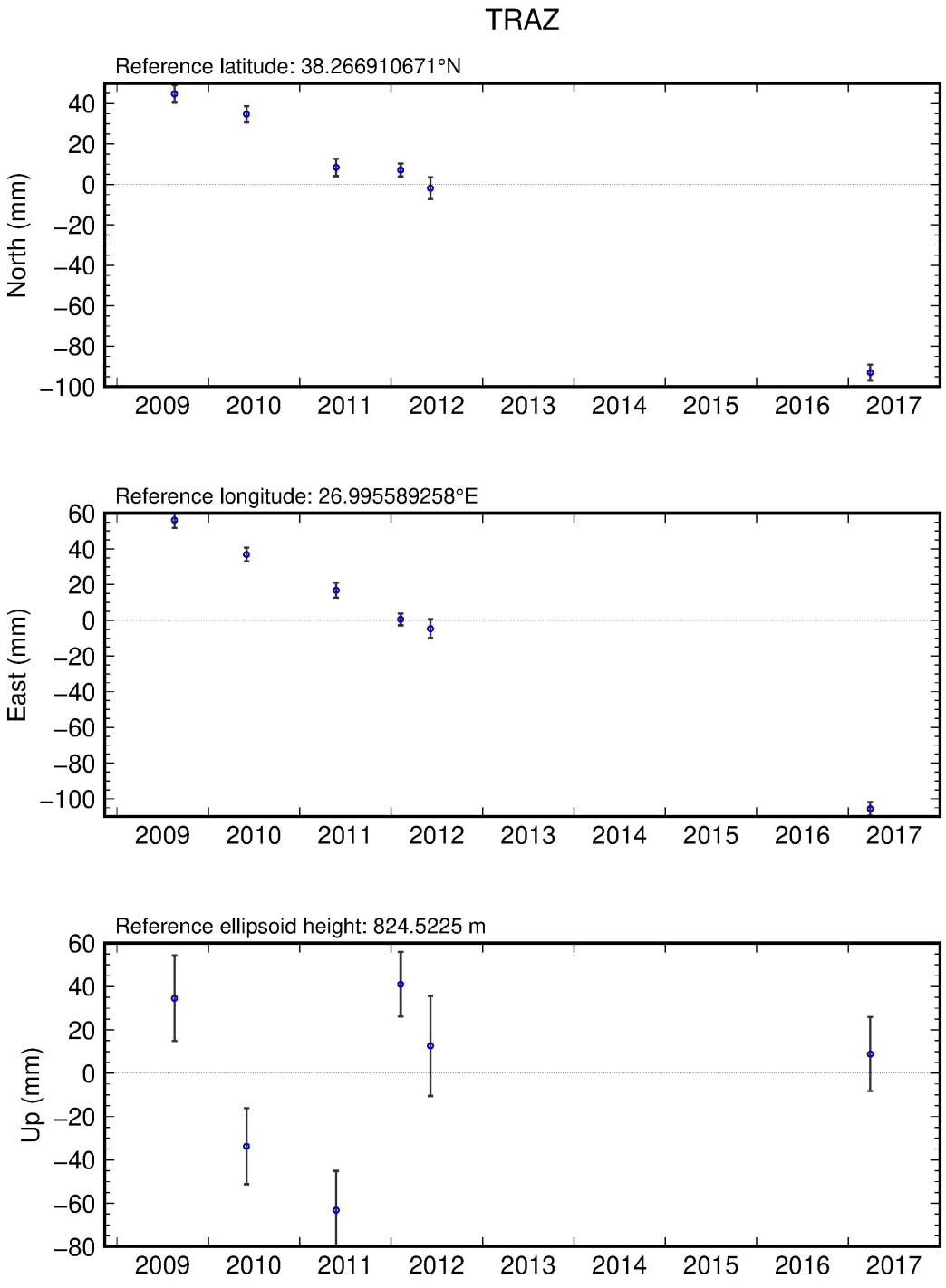

Figure C.20. GPS time series of TRAZ Station.

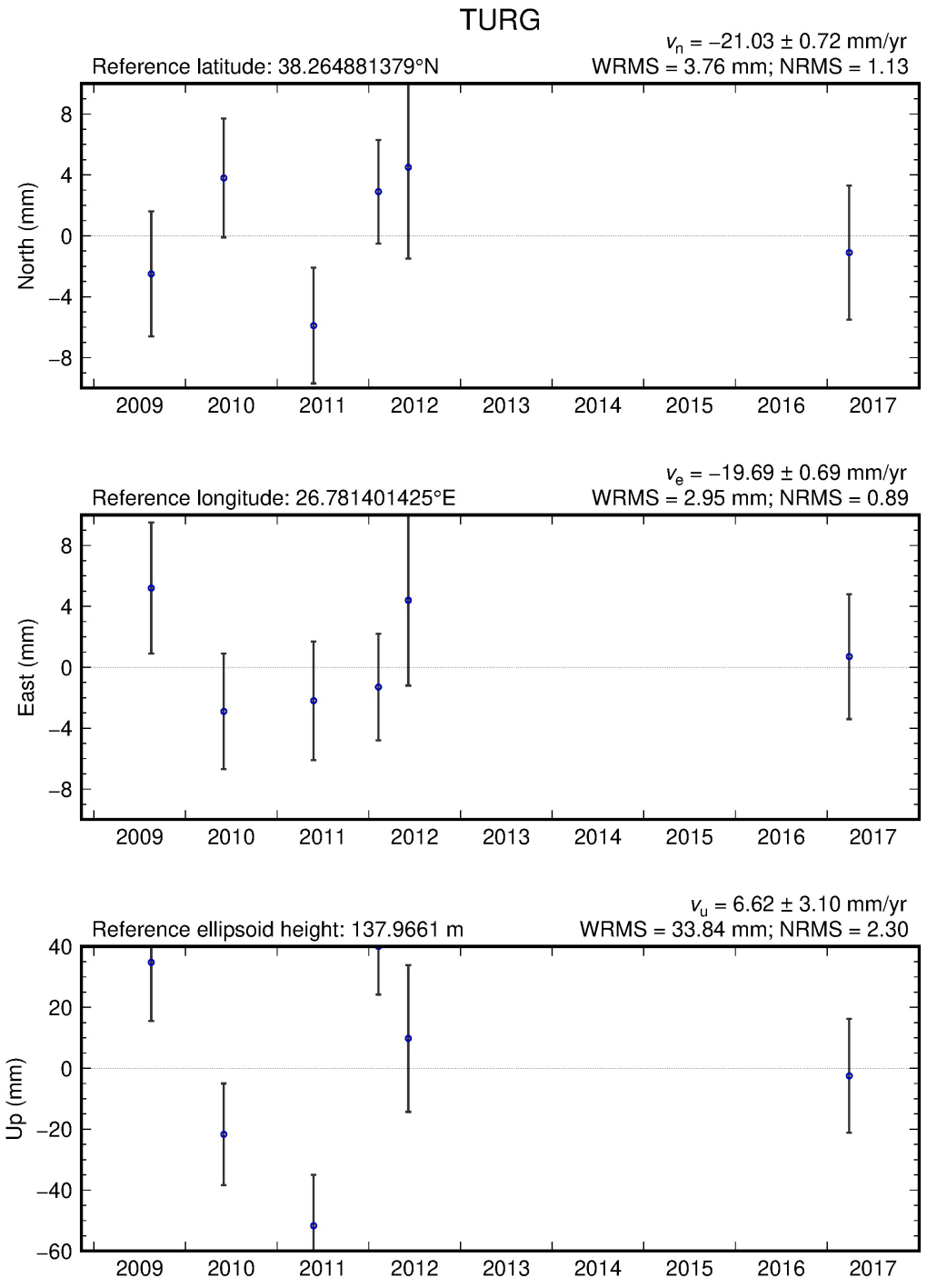

Figure C.21. North, east and up velocities and their uncertainties of TURG Station.

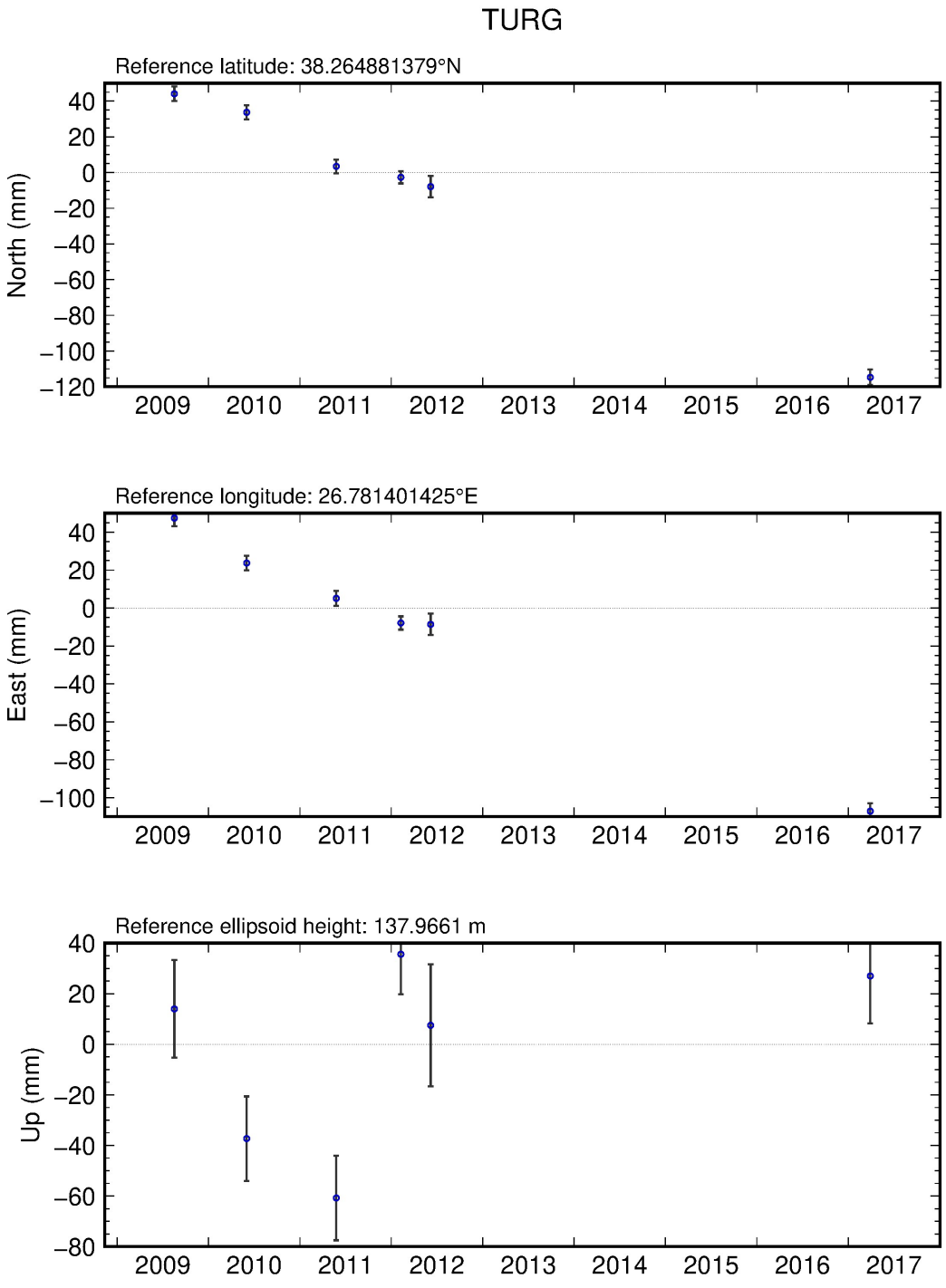

Figure C.22. GPS time series of TURG Station.

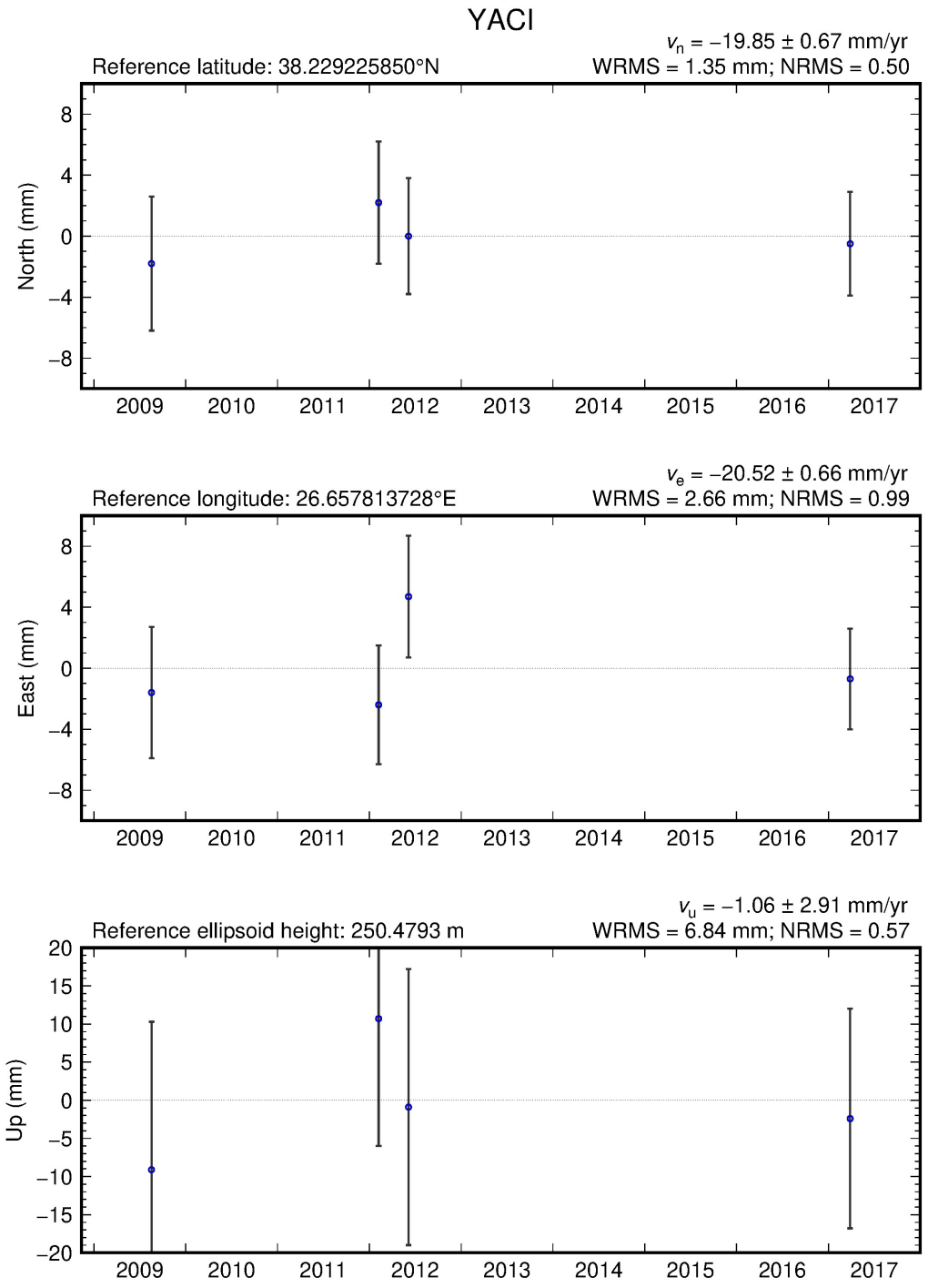

Figure C.23. North, east and up velocities and their uncertainties of YACI Station.

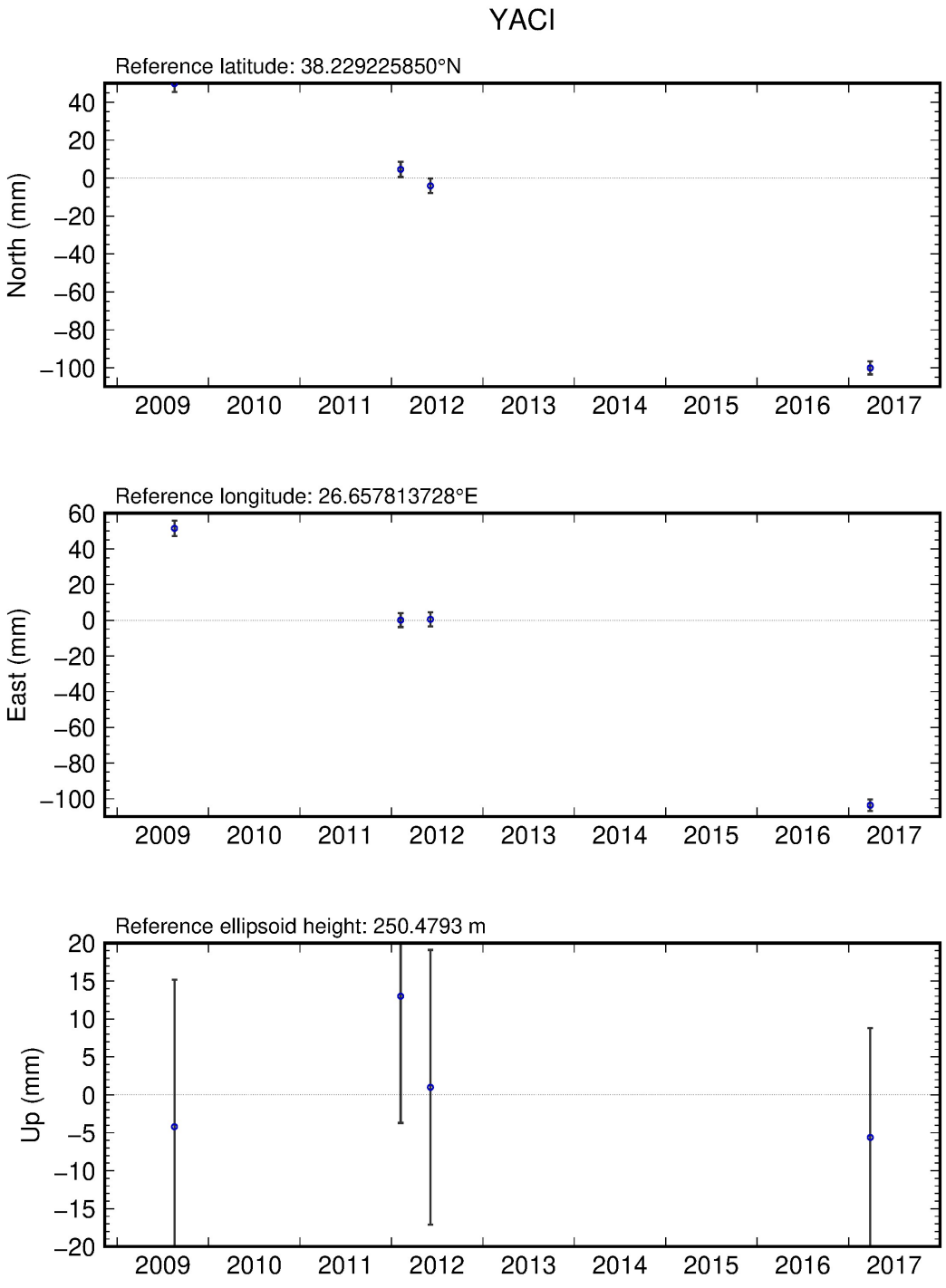

Figure C.24. GPS time series of YACI Station.

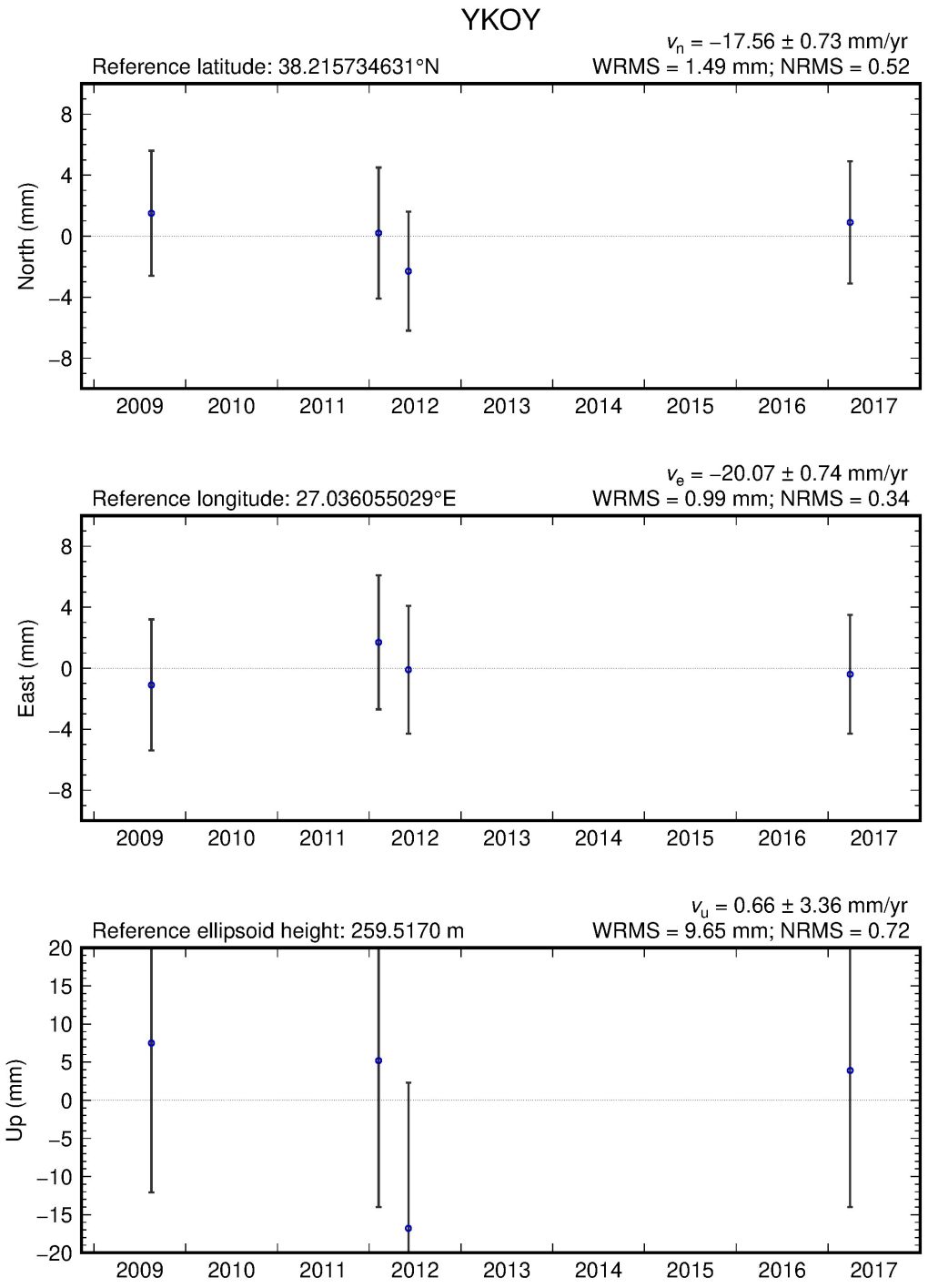

Figure C.25. North, east and up velocities and their uncertainties of YKOY Station.

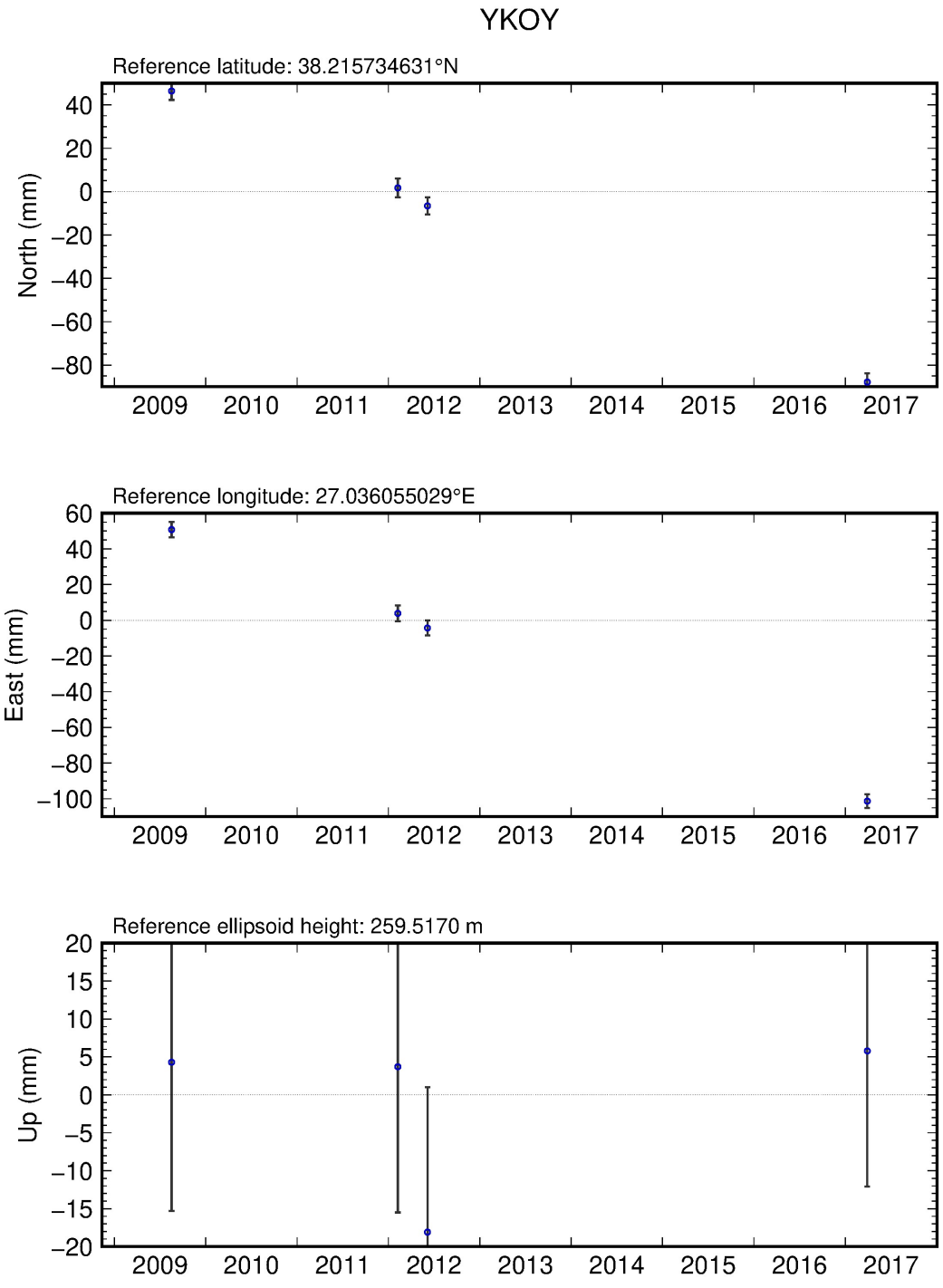

Figure C.26. GPS time series of YKOY Station.

APPENDIX D: FOCMEC OUTPUTS WITH STATION DISTRIBUTION

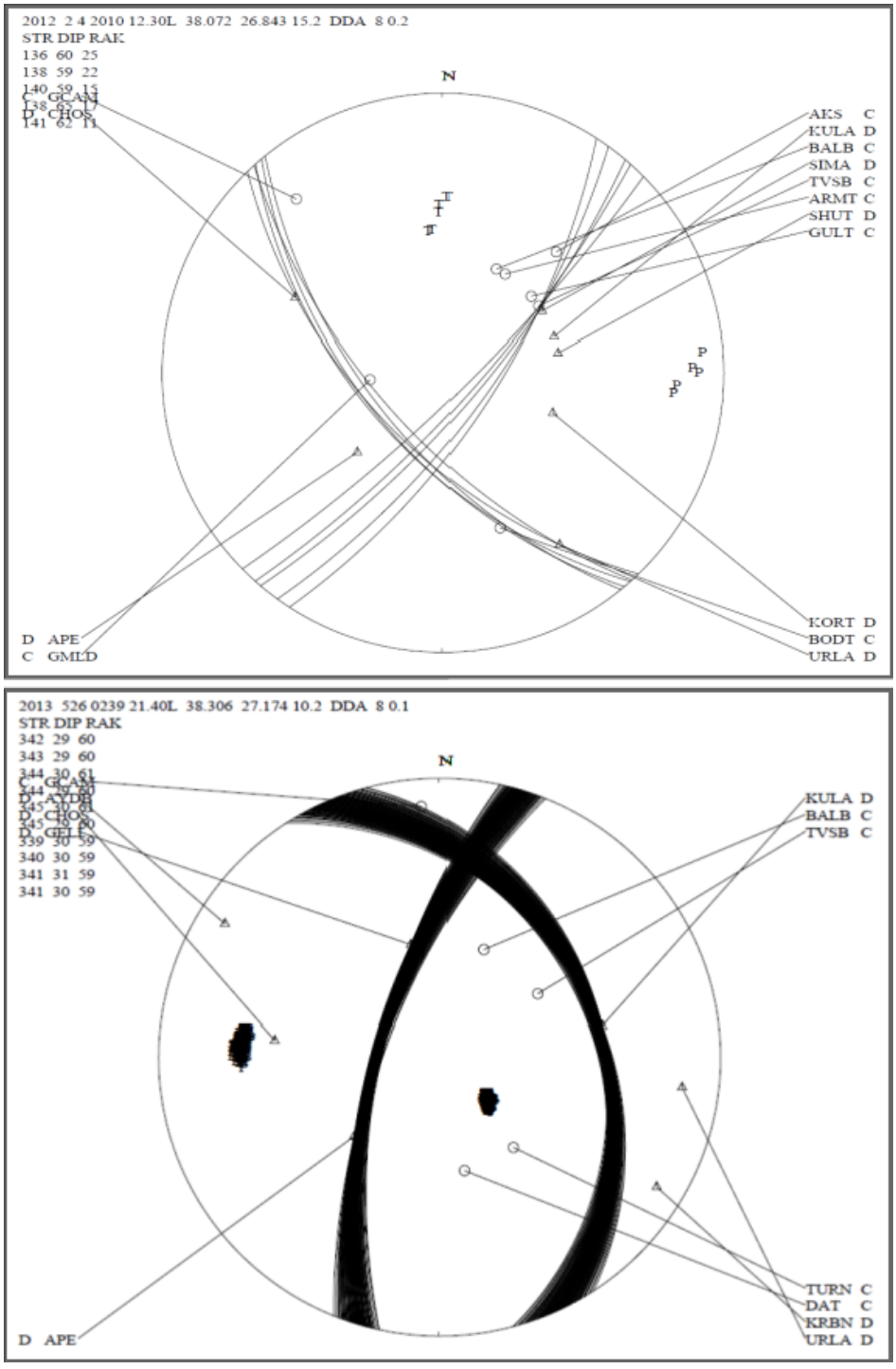

Figure D.1. Focmec outputs of the earthquakes examined in section 5.

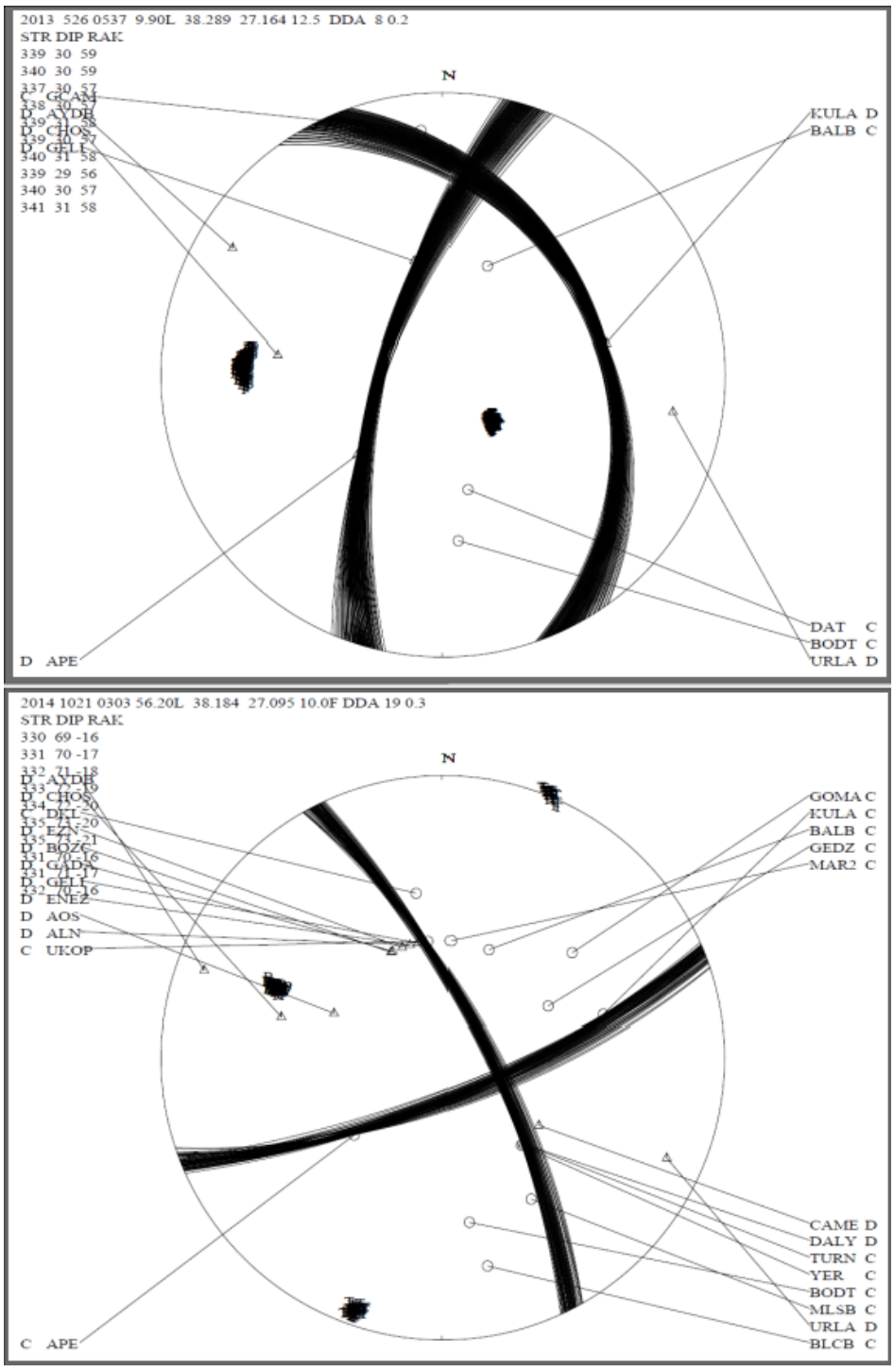

Figure D.2. Focmec outputs of the earthquakes examined in section 5.

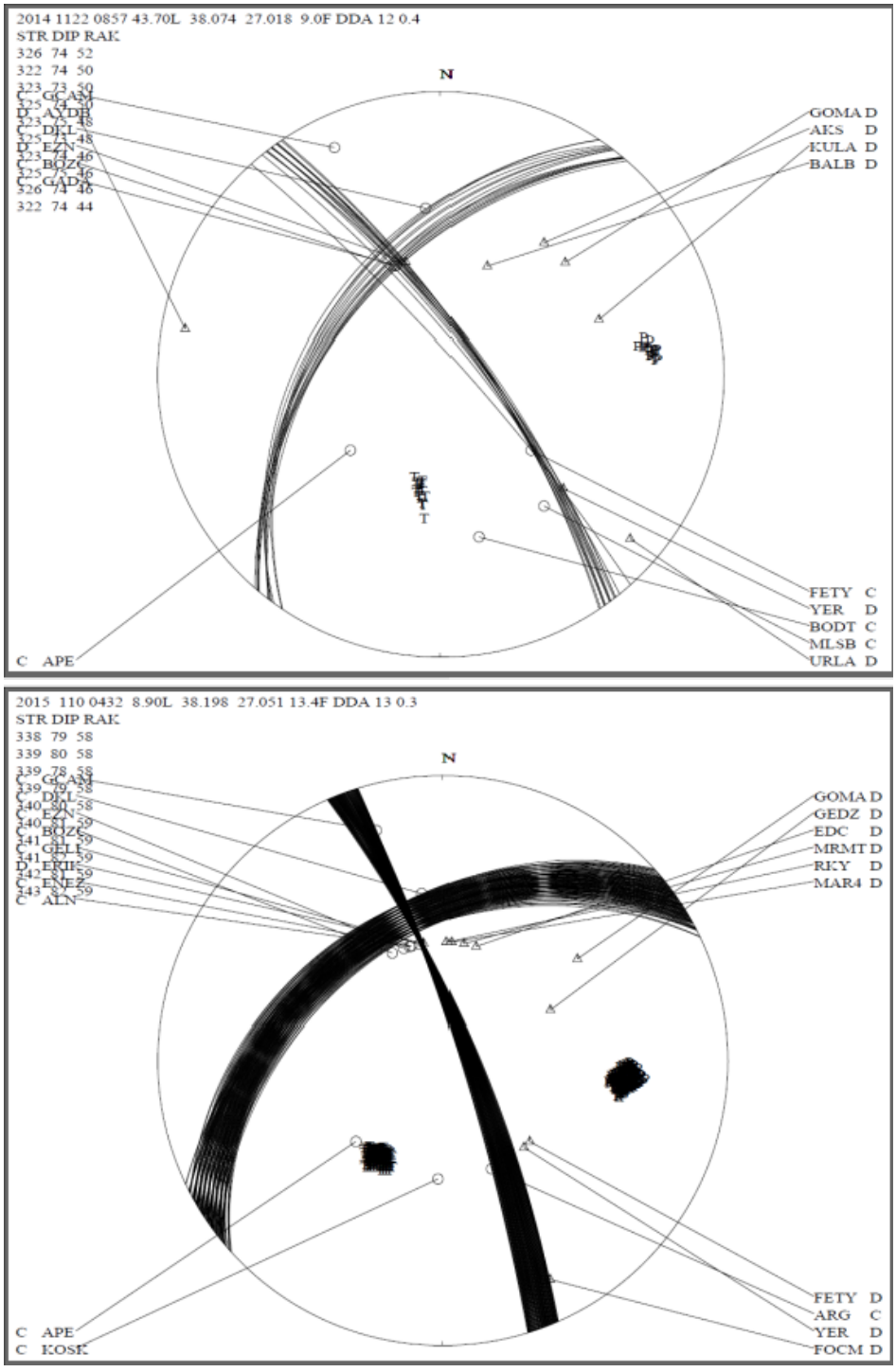

Figure D.3. Focmec outputs of the earthquakes examined in section 5.

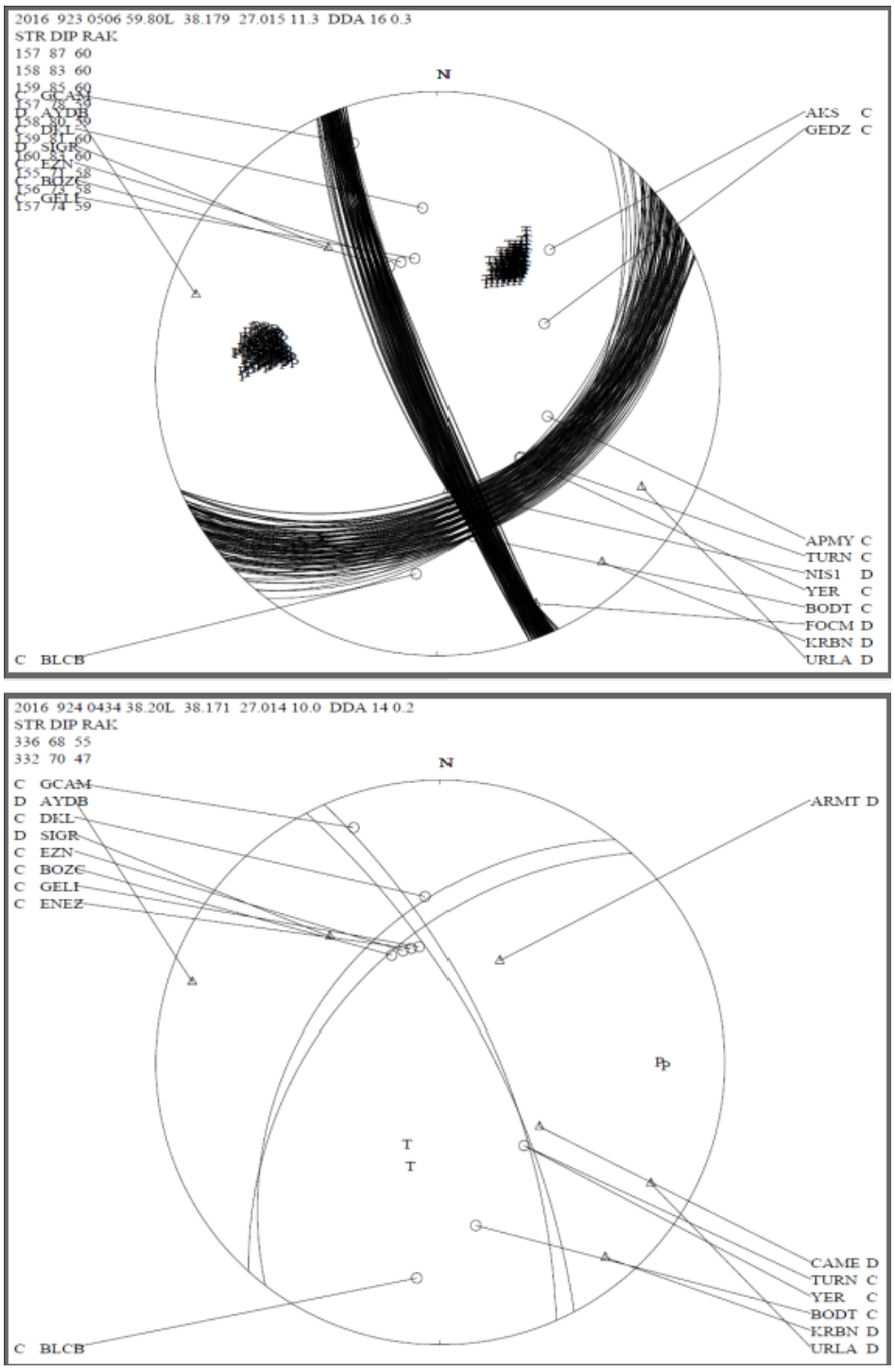

Figure D.4. Focmec outputs of the earthquakes examined in section 5.

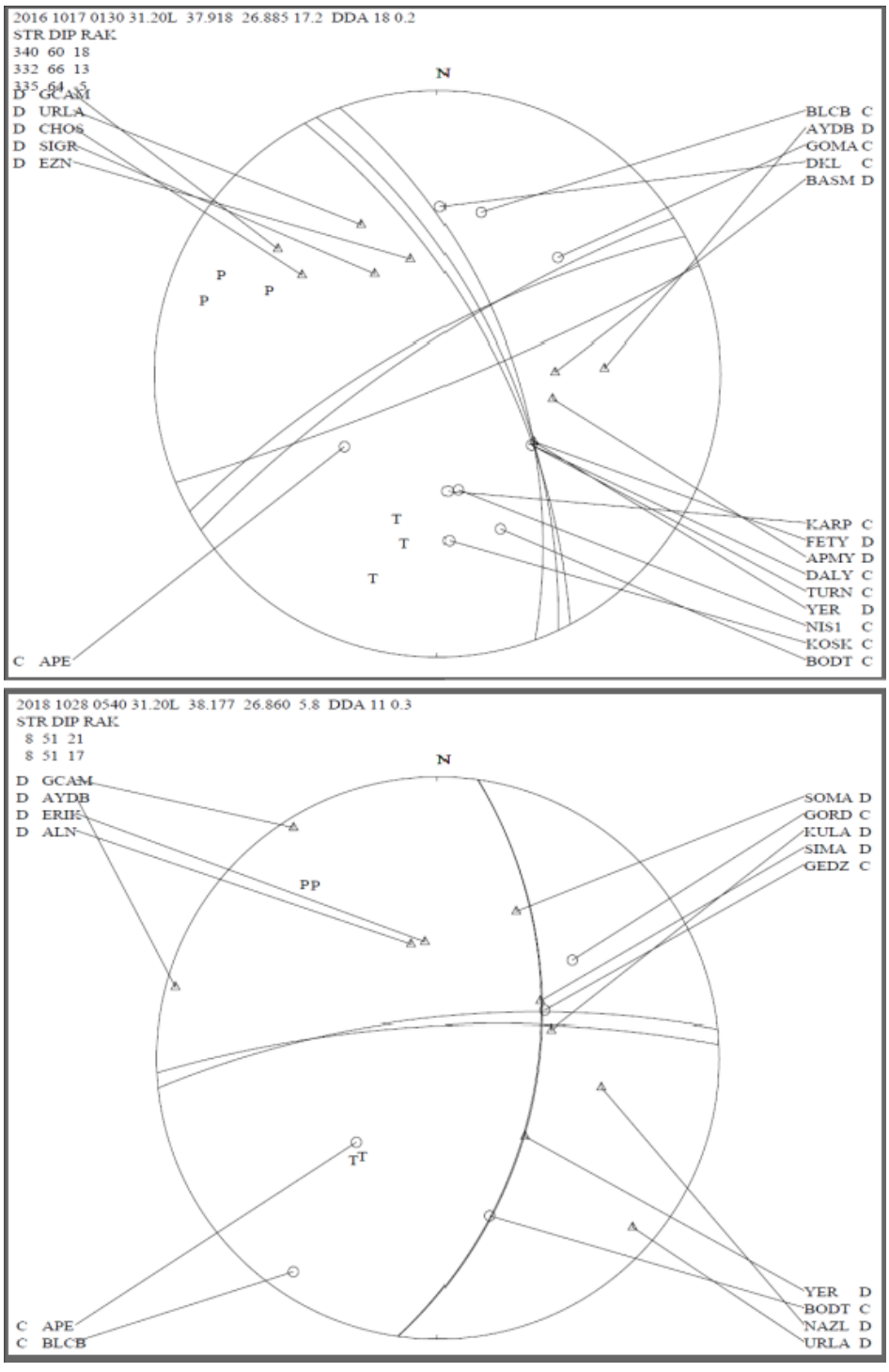

Figure D.5. Focmec outputs of the earthquakes examined in section 5.

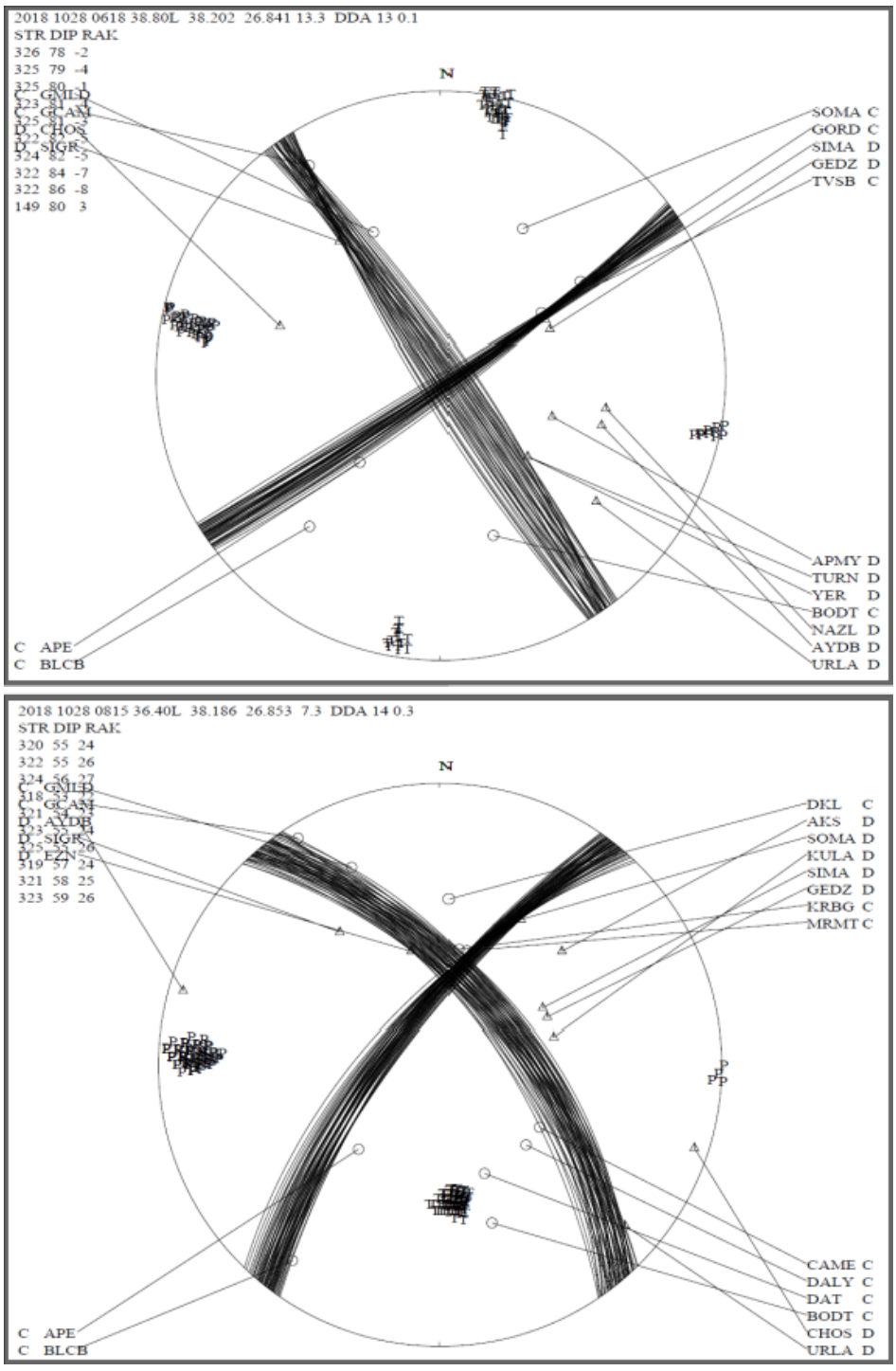

Figure D.6. Focmec outputs of the earthquakes examined in section 5.

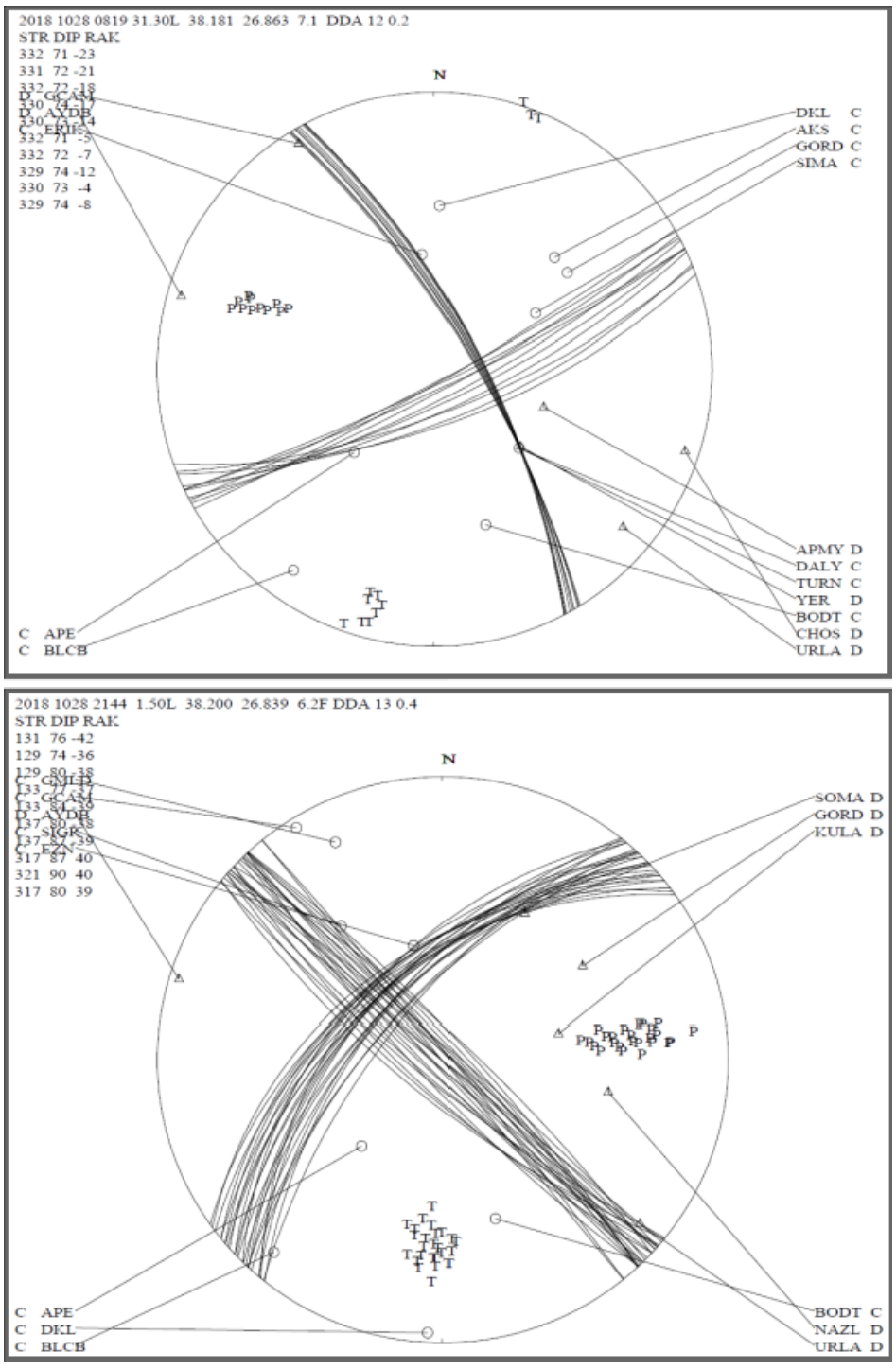

Figure D.7. Focmec outputs of the earthquakes examined in section 5.

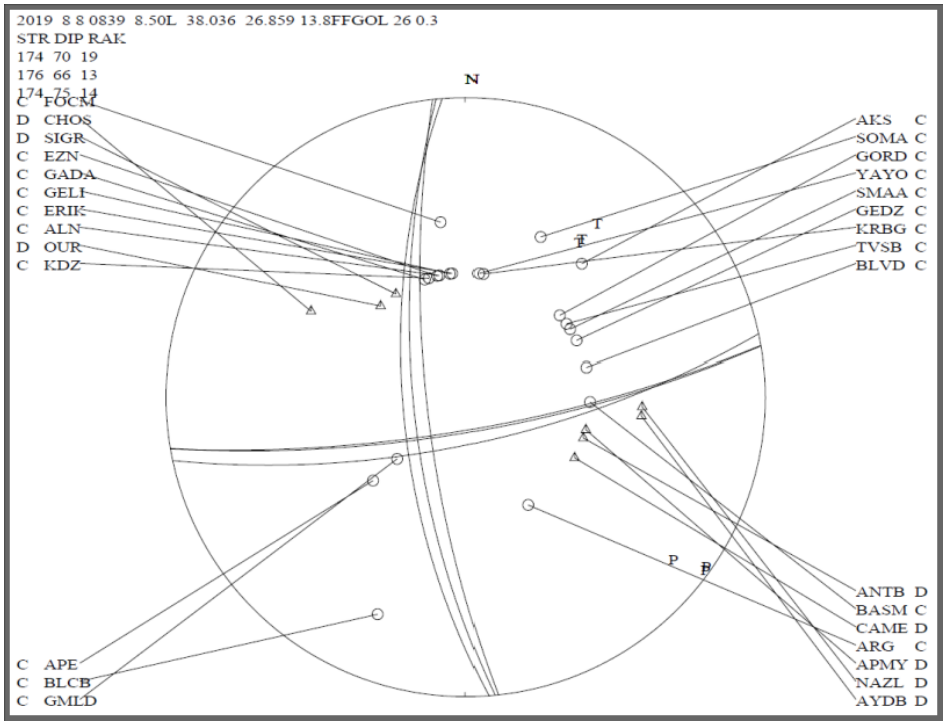

Figure D.8. Focmec outputs of the earthquakes examined in section 5.